

# Structurally Enhanced Electrodes for Redox Flow Batteries Produced via Electrospinning

by

Kyu Min Lee

A thesis

presented to the University of Waterloo

in fulfillment of the

thesis requirement for the degree of

Doctor of Philosophy

in

Chemical Engineering

Waterloo, Ontario, Canada, 2024

© Kyu Min Lee 2024

## Examining Committee Membership

The following served on the Examining Committee for this thesis. The decision of the Examining Committee is by majority vote.

Supervisor

Prof. Jeff Gostick

Department of Chemical Engineering, University  
of Waterloo

Supervisor

Prof. Edward (Ted) Roberts

Department of Chemical & Petroleum  
Engineering, University of Calgary

Internal Member

Prof. Michael Pope

Department of Chemical Engineering, University  
of Waterloo

Internal Member

Prof. Yuning Li

Department of Chemical Engineering, University  
of Waterloo

Internal-external Member

Prof. Xiaoyu Wu

Department of Mechanical Engineering,  
University of Waterloo

External Member

Prof. Roswitha Zeis

Department of Electrical, Electronic &  
Information Technologies, Friedrich-Alexander-  
Universität Erlangen-Nürnberg

## **Author's Declaration**

This thesis consists of material all of which I authored or co-authored: see Statement of Contributions included in the thesis. This is a true copy of the thesis, including any required final revisions, as accepted by my examiners.

I understand that my thesis may be made electronically available to the public.

## Statement of Contributions

Kyu Min Lee was the main author for this thesis written under the supervision of Prof. Jeff Gostick and Prof. Edward Roberts.

This thesis is based on manuscripts and chapters 3, 4, and 5 are adapted from the following publications or manuscript:

**Chapter 3** is based on the following publication:

Lee, K. M., Pahlevaninezhad, M., Smith, V., Abouali, S., Orfino, F. P., Kjeang, E., ... & Gostick, J. T. (2023). Improvement of vanadium redox flow battery performance obtained by compression and laser perforation of electrospun electrodes. *Materials Today Energy*, 35, 101333.

Contributions:

Kyu Min Lee. Conceptualization, Methodology, Investigation, Data Curation, Writing - Original Draft, Writing - Review & Editing. Sara Abouali. Software, Formal analysis, Investigation, Data Curation, Writing - Original Draft. Maedeh Pahlevaninezhad. Methodology, Formal analysis, Investigation, Data Curation, Writing - Original Draft. Francesco P. Orfino. Software, Formal analysis, Investigation. Victoria Smith. Methodology, Investigation. Erik Kjeang. Conceptualization, Resources, Supervision, Project administration. Michael Pope. Resources, Project administration, Funding acquisition. Edward Roberts. Conceptualization, Resources, Data Curation, Writing - Original Draft, Writing - Review & Editing, Supervision, Project administration, Funding acquisition. Jeff Gostick. Conceptualization, Software, Formal analysis, Investigation, Resources, Writing - Original Draft, Writing - Review & Editing, Visualization, Supervision, Project administration. Funding acquisition.

**Chapter 4** is based on the following publication:

Lee, K. M., E, Roberts., Gostick, J. T. (2023). Analysis of physical properties and operating efficiency of multi-layered fibrous electrodes for vanadium redox flow battery with multiphysics simulation. *Journal of Electrochemical Society* (In Peer-Review)

Contributions:

Kyu Min Lee. Conceptualization, Methodology, Investigation, Data Curation, Writing - Original Draft, Writing - Review & Editing. Edward Roberts. Conceptualization, Resources, Data Curation, Writing - Original Draft, Writing - Review & Editing, Supervision, Project administration, Funding acquisition. Jeff Gostick. Conceptualization, Software, Formal analysis, Investigation, Resources, Writing - Original Draft, Writing - Review & Editing, Visualization, Supervision, Project administration. Funding acquisition.

**Chapter 5** based on the following publication:

Lee, K. M., E, Roberts., Gostick, J. T. (2023). Multi-layered structure built with compressed and laser perforated electrospun fibrous electrode for vanadium redox flow battery. *Journal of Electrochemical Society* (In Preparation)

Contributions:

Kyu Min Lee. Conceptualization, Methodology, Investigation, Data Curation, Writing - Original Draft, Writing - Review & Editing. Edward Roberts. Conceptualization, Resources, Data Curation, Writing - Original Draft, Writing - Review & Editing, Supervision, Project administration, Funding acquisition. Jeff Gostick. Conceptualization, Software, Formal analysis, Investigation, Resources, Writing - Original Draft, Writing - Review & Editing, Visualization, Supervision, Project administration. Funding acquisition.

## **Abstract**

### **Structurally Enhanced Electrodes for Redox Flow Batteries Produced via Electrospinning**

Kyu Min Lee  
Doctor of Philosophy  
Department of Chemical Engineering  
University of Waterloo, Canada, 2023

The vanadium redox flow battery is one of the most promising secondary batteries for energy storage system due to its design flexibility attributed to the large adjustable capacity of the storage tanks filled with electrolyte solution. However, the vanadium redox flow battery is not yet widely deployed owing to its low power density. This thesis describes the way of constructing the fibrous electrode with novel structure to overcome the flaw. The general electrospun materials of polyacrylonitrile were synthesized with substantially lower porosity than standard materials by applying compression during the stabilization stage. This objective was to create flow battery electrodes with higher volumetric surface area. The flexibility of the electrospinning technique combined with adjustable post-processing steps such as stabilization and carbonization allowed for the creation of layers with very specific structural and transport properties. In-plane permeability was found to remain relatively constant compared to the original uncompressed fibrous structure. On the other hand, the fibers compacted and compressed down to the flat ribbon shape hurt the through-plane permeability, so artificial holes were created using a CO<sub>2</sub> laser to perforate the structure. The loss of specific surface area caused by laser perforation was quite negligible and still showed improvement. Overall, the novel flow-through electrode provided from this study successfully contributed to improving the transport properties as well as the electrochemical reaction rate, leading to the optimal power density of a vanadium redox flow battery. In

addition to that, 2-dimensional half-cell model was created with multi-physics simulation to predict the change in performance with respect to the structural properties of fibrous electrode. The performance was evaluated based on polarization behavior, required pumping power to operate the cell, and operating efficiency. Moreover, electrode was constructed to multi-layered structure in profiles of permeability, fiber size, and porosity. The vanadium ion could be distributed uniformly over the entire region of electrode, which enabled more portion of fiber surface to be utilized for reaction to improve power density while maintaining low pumping power for operation. Based on the prediction from the model, the actual experimental work was invested for multi-layered structure built with novel electrospun fibrous layers. Two different flow channel designs were considered: interdigitated and parallel. The convective flow was induced with the interdigitated flow channel design. Thus, the vanadium ions could be distributed effectively to the region of electrode, resulting in the higher power density. The electrode created in multi-layer provided higher net power density even though the increased pumping power requirement compared to the case of single layer. The body of work presented in this thesis has contributed significantly to understanding the mass transport phenomena taking place in electrodes built in novel fibrous structures. It highlights the preparation of this media through electrospinning as well as numerical and experimental methods for characterizing and understanding these processes. All the work presented here promoted the development of flow batteries through better understanding of the flow battery electrode.

## **Acknowledgements**

I would like to sincerely thank my supervisors Dr. Jeff Gostick and Dr. Ted Roberts for providing the opportunity, support, and guidance throughout my PhD studies. Their invaluable advice has guided me to grow as a researcher and to be able to reach the point where I am now. Especially, I still remember the first day I contacted Dr. Jeff Gostick at the Canadian Chemical Engineering Conference during my master's study. It was one of the best lucks in my life to meet him. I wish to express deep appreciation for his generosity and kindness. Whether I was depressed or frustrated with work, he has been an inspiration to me that I should always know how to stand whenever I am down. As a result, I could be successfully grown up as an expert in the field of porous media.

I also would like to thank my thesis evaluation committee, Dr. Michael Pope, Dr. Yuning Li, Dr. Xiaoyu Wu, and Dr. Roswitha Zeis for taking the time in reviewing this work and for their valuable comments and advice for improving this thesis.

I am also thankful to my friends and graduate students in the Department of Chemical Engineering at the University of Waterloo for making my graduate life unforgettable. Especially, I would also like to extend my gratitude to PMEAL group members, Hao Yu, Sam Ly, Nikolai Burton, Mike McKague, Serveh Abdollahi, Nooruddin Jamali, and Yong Wook Kim for their unlimited support during my period of study at the University of Waterloo. Their warm encouragement and kindness helped me to adjust to the program. Also, I would like to acknowledge all my Korean friends for their friendship and encouragement. Special thanks go to Moon Gyu Park, Jun Geun Um, Hey Woong Park, and Se Young Kim. You always helped me

to restore confidence when frustrated with my work. It was my pleasure to meet all of you.

I also owe my deepest gratitude to my beloved parents, Nam Won Lee and Hyun Sook Park, and my younger brother, Kyu Ho Lee, for their endless love, belief, encouragement, and support over whole my life. From the time of immigrating to Canada, we have endured many hardships that others cannot imagine. I will never forget your sacrifices and repay your kindness for the rest of my life. Also, it is a little late, but I would like to congratulate my brother's marriage and welcome his wife, Ohn Min, for being our family member. I love all of you so much.

Finally, I'm very grateful to my God for giving me the strength and wisdom throughout my graduate studies to complete another chapter of my life.

## **Dedication**

Dedicated to My Family

# Table of Contents

<b>Examining Committee Membership</b> .....	<b>ii</b>
<b>Author’s Declaration</b> .....	<b>iv</b>
<b>Statement of Contributions</b> .....	<b>v</b>
<b>Abstract</b> .....	<b>vii</b>
<b>Acknowledgements</b> .....	<b>ix</b>
<b>Dedication</b> .....	<b>xi</b>
<b>List of Figures</b> .....	<b>xvi</b>
<b>List of Tables</b> .....	<b>xx</b>
<b>List of Abbreviations</b> .....	<b>xxi</b>
<b>1. Introduction and Research Objectives</b> .....	<b>1</b>
1.1. Introduction .....	1
1.2. Research Objectives and outline.....	4
<b>2. Literature Review</b> .....	<b>7</b>
2.1. Mechanism of Redox Flow Battery .....	7
2.2. Redox Couples .....	8
2.3. Material and Role of Electrode .....	12
2.4. Porous Electrode .....	14
2.4.1. <i>Electrospinning</i> .....	15
2.4.2. <i>Stabilization and Carbonization</i> .....	17
2.5. Properties of porous electrode .....	19
2.6. Electrode characterization methods .....	22
2.6.1. <i>Permeability</i> .....	22
2.6.2. <i>Porosity</i> .....	24
2.6.3. <i>Specific Surface area</i> .....	26

2.7.	Polarization behavior .....	27
2.8.	Flow channel .....	29
2.8.1.	<i>Types of Flow Channel Design</i> .....	29
2.9.	Past Works.....	31
2.10.	Research Target .....	33
<b>3.</b>	<b>Improvement of Vanadium Redox Flow Battery Performance Obtained by Compression and Laser Perforation of Electrospun Electrodes .....</b>	<b>38</b>
3.1.	Introduction .....	38
3.2.	Experimental Methods.....	40
3.2.1.	<i>Electrospinning</i> .....	40
3.2.2.	<i>Stabilization and Carbonization</i> .....	41
3.2.3.	<i>In-Plane and Through-Plane Permeability</i> .....	42
3.2.4.	<i>Porosity</i> .....	43
3.2.5.	<i>Specific Surface Area</i> .....	43
3.2.6.	<i>Laser Perforation</i> .....	44
3.2.7.	<i>Tomography</i> .....	44
3.2.8.	<i>Flow Cell Validation</i> .....	47
3.3.	Results and Discussion.....	49
3.3.1.	<i>Impact of Compression During Stabilization</i> .....	49
3.3.2.	<i>Impact of Laser Perforation</i> .....	60
3.3.3.	<i>Cell Performance Assessment by Polarization Curves</i> .....	62
3.4.	Conclusion.....	64
<b>4.</b>	<b>Multiphysics Simulation of Multi-layered Fibrous Electrodes for Vanadium Redox Flow Battery .....</b>	<b>66</b>
4.1.	Introduction .....	66
4.2.	Modeling Approach.....	68
4.2.1.	<i>Geometry</i> .....	68
4.2.2.	<i>Ion Transportation</i> .....	70
4.2.3.	<i>Electrochemical Reaction</i> .....	72

4.2.4.	<i>Dissociation of Sulfuric Acid</i> .....	74
4.2.5.	<i>State of Charge (SOC)</i> .....	74
4.2.6.	<i>Model Parameters</i> .....	74
4.2.7.	<i>Model Validation</i> .....	76
4.3.	Results and Discussion .....	78
4.3.1.	<i>Baseline Case: Electrospun Electrodes with Same Properties in All Layers</i> .....	78
4.3.2.	<i>Varying Properties Between Layers</i> .....	81
4.3.3.	<i>Pumping Cost Analysis</i> .....	84
4.3.4.	<i>Optimization</i> .....	89
4.4.	Conclusion.....	91
4.5.	Acknowledgements.....	93
<b>5.</b>	<b>Multi-layered Structure Built with Compressed and Laser Perforated Electrospun Fibrous Electrode for Vanadium Redox Flow Battery</b> .....	<b>94</b>
5.1.	Introduction .....	94
5.2.	Experimental Method .....	96
5.2.1.	<i>Electrolytes</i> .....	96
5.2.2.	<i>Cyclic Voltammetry</i> .....	97
5.2.3.	<i>Flow cell validation</i> .....	97
5.2.4.	<i>Pumping power</i> .....	98
5.3.	Results and Discussion .....	99
5.3.1.	<i>Characterization of samples</i> .....	99
5.3.2.	<i>Cyclic Voltammetry</i> .....	100
5.3.3.	<i>Application of interdigitated flow design</i> .....	102
5.3.4.	<i>Application of parallel channel design</i> .....	113
5.4.	Conclusion.....	120
<b>6.</b>	<b>Conclusions and Future Work</b> .....	<b>122</b>
6.1.	Summary and Conclusion .....	122
6.2.	Suggestions for Future Works .....	124

6.2.1.	<i>Analysis in the size and concentration of artificial holes</i>	124
6.2.2.	<i>Development of time-dependent model in COMSOL Multiphysics</i>	125
6.2.3.	<i>Development of meso-pores on fiber surface</i>	125
6.2.4.	<i>Analysis in component of liquid electrolyte</i>	126
<b>References</b>		<b>127</b>
<b>Appendices</b>		<b>139</b>

## List of Figures

Figure 1-1 – Investment in the field of renewable energy worldwide.....	2
Figure 1-2 – Share of renewable energy sources in electricity generation.....	2
Figure 2-1– Schematic representation of vanadium redox flow battery [7].....	8
Figure 2-2–a) Schematic of mass transport of active species through a porous electrode. b) Schematic illustration of redox reaction mechanism on surface of cathode, c) on surface of anode [7] .....	13
Figure 2-3 - Structure of fibrous electrode in vanadium redox flow battery [48].....	14
Figure 2-4 – Design of electrospinner .....	16
Figure 2-5 – SEM images of electrospun fibres with different wt% of PAN in the mixture. The scale bar on each image is 10 $\mu m$ .....	17
Figure 2-6 - Change in the structure of polyacrylonitrile during stabilization and carbonization [62] .....	18
Figure 2-7 – Electrospun polyacrylonitrile (PAN) material before and after carbonization [24] .....	19
Figure 2-8 – Pore-scale mechanisms resulting in macroscopic dispersion coefficients .....	22
Figure 2-9 – Experimental set-up for a) in-plane, and b) through-plane permeability measurements .....	24
Figure 2-10 – Porosity measurement set-up.....	25
Figure 2-11 – Dynamic vapor sorption (DVS) resolution device .....	27
Figure 2-12 – Polarization behavior from general redox flow cell [69].....	28
Figure 2-13 – Designs of flow channel in the Vanadium Redox Flow Battery [75].....	30
Figure 2-14 – Change of net power density in terms of inlet concentration of reactant and flow rate of electrolyte with a) flow-through mode (without flow field) and b) interdigitated flow field .....	35
Figure 3-1– SEM images of pristine (a and c) and compressed (b and d) carbonized samples at low and high magnification .....	50
Figure 3-2 – a) Porosities of samples with different pre- and post-processing conditions applied, and b) volumetric renderings of the segmented images with the uncompressed sample on the left, and compressed sample on the right. Axis values indicate voxels, which were 16 $nm$ in length. ....	53
Figure 3-3 – a) Pore size distributions for compressed and uncompressed samples, and b) Fiber size distributions for pristine and compressed samples.....	54
Figure 3-4 - In-plane permeabilities at different degree of compression.....	58

Figure 3-5 – Voltage gradients obtained with direct numerical simulations of electron conduction in the solid phase. Top row: Uncompressed, bottom row: Compressed. Color represents the voltage gradient ranging from 1 (red) to 0 (blue).....60

Figure 3-6 – SEM images of laser perforated sintered sample ( $178 \mu m$ ) with the distance of a)  $1000 \mu m$  and b)  $2000 \mu m$  between holes, laser perforated hole with the magnification of c) x1600 and d) x2700 .....62

Figure 3-7 - Polarization and power density curves at 50% state of charge .....64

Figure 4-1 – Domain of cathode containing a) single, and b) multi-layer with boundary conditions applied on Multiphysics simulation .....69

Figure 4-2 – Polarization and power density curves at different flow rate of electrolyte across the SGL39AA domain .....78

Figure 4-3 - Polarization curves for the baseline case. Panel (a) shows the performance as a function of fluid flow rate for a constant inlet concentration of  $1000 \text{ mol}/m^3$ . Panel (b) shows the case for different inlet concentrations at a constant flow rate of  $10 \text{ mL}/min$ . The black lines represent the SGL39AA material at the highest and lowest value of the varied parameter to indicate the performance range. ....79

Figure 4-4 - Polarization behavior plotted against electrochemical conversion factor. Panel (a) shows the performance as a function of fluid flow rate for a constant inlet concentration of  $1000 \text{ mol}/m^3$ . Panel (b) shows the case for different inlet concentrations at a constant flow rate of  $10 \text{ mL}/min$ . The black lines represent the SGL39AA material at the highest and lowest value of the varied parameter to indicate the performance range. ....80

Figure 4-5 – Complete set of polarization curves for all 5 electrode materials studied here as a function of electrolyte flowrate for a constant inlet concentration of  $1000 \text{ mol}/m^3$ . Panels (a-e) show the standard polarization curve while panels (f-j) show the electrochemical conversion defined by Eq.4-29. ....82

Figure 4-6 - Polarization curves for all electrodes studied here as a function of inlet concentration at a constant flow rate of  $10 \text{ mL}/min$ . Panels (a-e) shows the standard polarization curves while panels (f-j) show the electrochemical conversion defined by Eq.4-29.....83

Figure 4-7 – Maximum electrochemical conversion factor as a function of limiting current density. Points for each electrode structure are connected by a colored line according to the legend. The marker colors indicate a) flow rate of electrolyte and b) inlet concentration of  $VO_2 +$  .....84

Figure 4-8 – Pumping efficiency vs current density for all the multilayered structures. Panels (a-d) show the

efficiency as a function of flow rate for a constant inlet concentration of  $1000 \text{ mol/m}^3$ . Panels (e-h) show the pumping efficient as a function of inlet concentration for a constant inlet flow rate of  $10 \text{ mL/min}$ , .....87

Figure 4-9 – Peak values of pumping efficiency vs the net power density for each condition for all structures. Each line corresponds to a given material, indicated in the legend. Panel (a) shows the peak pumping efficiency as a function of flow rate for a constant inlet concentration of  $1000 \text{ mol/m}^3$  with the color of each marking corresponding to the flow rate. Panel (b) shows the peak pumping efficient as a function of inlet concentration for a constant flow rate of  $10 \text{ mL/min}$  with the color of each marker corresponding to concentration.....88

Figure 4-10 – a) Polarization curve, b) the data with the current density expressed as electrochemical conversion factor, c) maximum electrochemical conversion factor as a function of peak current density, and d) peak values of net efficiency values vs the net power density obtained at that condition for multi-layered electrodes built with optimal conditions. All cases were using a flow rate of  $10 \text{ mL/min}$  and an inlet concentration of  $1000 \text{ mol/m}^3$ . .....91

Figure 5-1 - SEM images of a) pristine and b) sintered electrospun fibrous sample at the magnification of X20000, c) laser perforated hole with the magnification of x1600.....100

Figure 5-2 – Cyclic voltammogram of SGL25AA, pristine, and compressed electrospun fibrous electrodes in terms of areal current density in  $0.05\text{M } \text{VOSO}_4 + 3.0\text{M } \text{H}_2\text{SO}_4$  electrolyte at a scan rate of  $10\text{mV/s}$  ..102

Figure 5-3 - Polarization and gross power density curves at 100% state of charge with interdigitated flow channel.....104

Figure 5-4 – Maximum gross power density approached via interdigitated flow channel with different layer types of fibrous electrodeS: SGL25AA.P: Pristine electrospun sample,C: Compressed electrospun sample,L: Compressed and laser perforated electrospun sample,X/Y: Double layer consist of X sample beside flow field and Y sample beside membrane.....105

Figure 5-5 – Distribution of  $\text{VO}_2^+$  ion in a) sample #1 and b) dual-layered fibrous electrodes built with layer 3 beside a rib and layer 2 beside a membrane in sample #3 on Table 4-2. C) is the case of dual layer which two layers are reversed .....107

Figure 5-6 – Inlet pressure and pumping power density required with each layer type of fibrous electrode to provide electrolyte flow rates when assembled with interdigitated flow channel.....109

Figure 5-7 – Net power density approached via interdigitated flow channel with different layer types of fibrous electrodes. S: SGL25AA, P: Pristine electrospun sample, C: Compressed electrospun sample, L: Compressed and laser perforated electrospun sample, X/Y: Double layer consist of X sample beside flow field and Y sample beside membrane .....112

Figure 5-8 – Net operating efficiency of redox flow cell with different layer types of fibrous electrode when assembled with interdigitated flow channel .....113

Figure 5-9- a) Polarization and b) gross power density curves at 100% state of charge with parallel flow channel. X\_Y\_(thin or thick): X sample beside flow field and Y sample beside membrane with the overall thickness of (thin: 170  $\mu\text{m}$ , thick: 340  $\mu\text{m}$ ) .....115

Figure 5-10 - Maximum gross power density approached via parallel flow channel with different layer types of fibrous electrode at the overall thicknesses of a) 340  $\mu\text{m}$  and b) 170  $\mu\text{m}$ .....116

Figure 5-11 – Inlet pressure and pumping power density required with each layer type of fibrous electrode at the overall thicknesses of a) 340  $\mu\text{m}$  and b) 170  $\mu\text{m}$  to provide electrolyte flow rates when assembled with parallel flow channel .....117

Figure 5-12 - Net power density approached via parallel flow channel with different layer types of fibrous electrodes at the overall thicknesses of a) 340  $\mu\text{m}$  and b) 170  $\mu\text{m}$ .....118

Figure 5-13 - Net operating efficiency of redox flow cell with different layer types of fibrous electrode at the overall thicknesses of a) 340  $\mu\text{m}$  and b) 170  $\mu\text{m}$  when assembled with parallel flow channel .....119

## List of Tables

Table 2-1 – Redox couples attempted for flow cell .....	9
Table 3-1 - Specific surface area of electrospun fibrous samples .....	55
Table 3-2 - Transport and physical properties of pristine and sintered samples .....	56
Table 4-1 - Fixed model parameters .....	75
Table 4-2 - Transport related parameters used in each study.....	75
Table 4-3 - Parameters determined by parameter sweep .....	89
Table 5-1 - Specific surface area of electrospun fibrous samples .....	101
Table 5-2 – List of fibrous samples used at each layer type .....	104

## List of Abbreviations

BET	Brunauer-Emmett-Teller
DMF	Dimethylformamide
DOE	Department of energy
DVS	Dynamic vapor sorption
ES	Electrospinning
ESS	Energy storage system
EU	European union
GDL	Gas diffusion layer
IRENA	international renewable energy agency
NASA	National Aeronautics and Space Administration
PAN	Polyacrylonitrile
PEMFC	Proton exchange membrane fuel cell
PTFE	Polytetrafluoroethylene
SEM	Scanning electron microscopy
SOC	State of charge

# **1. Introduction and Research Objectives**

## **1.1. Introduction**

The global energy consumption has been increased rapidly due to the accelerated industrialization, inordinate technical developments, and economic growth. The increase in global energy demand accelerates the greenhouse gas emission, which induces global warming and climate changes. Renewable energies have been employed as alternative sources to mitigate those growing global environmental issues since no polluting emissions are produced [1,2,3]. According to the international renewable energy agency (IRENA), the use of renewable energy source should be increased by 57% globally until 2030 to keep the rise of average global temperature below 2°C [4]. As can be confirmed from Figure 1-1, various countries in worldwide are investing in the field of renewable energy to approach the goal. Especially, China is investing acidulously more than every other country in the world. European union (EU) is the next largest investors followed by United States of America (USA) [5].

According to Figure 1-2, hydropower occupies 44.44% of renewable energies but requires high cost for dam construction to store them, resulting in low economic efficiency. Also, natural environments are destroyed by flooding as well as the geological damage [6]. For this reason, solar photovoltaic and wind energies are considered alternatively as main renewable energy sources. However, they are inherently unstable due to the high dependence to earth's climate. For instance, the solar panels are inefficient to be used in cloudy weather while the wind turbines cannot be operated in calm weather.

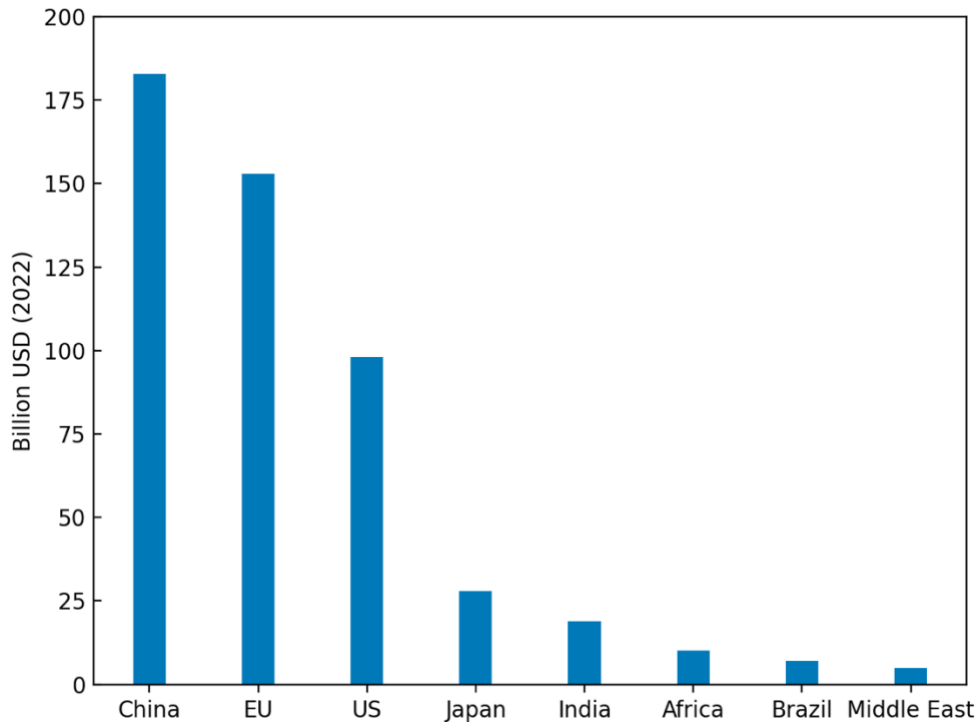


**Figure 1-1 - Investment in the field of renewable energy worldwide**

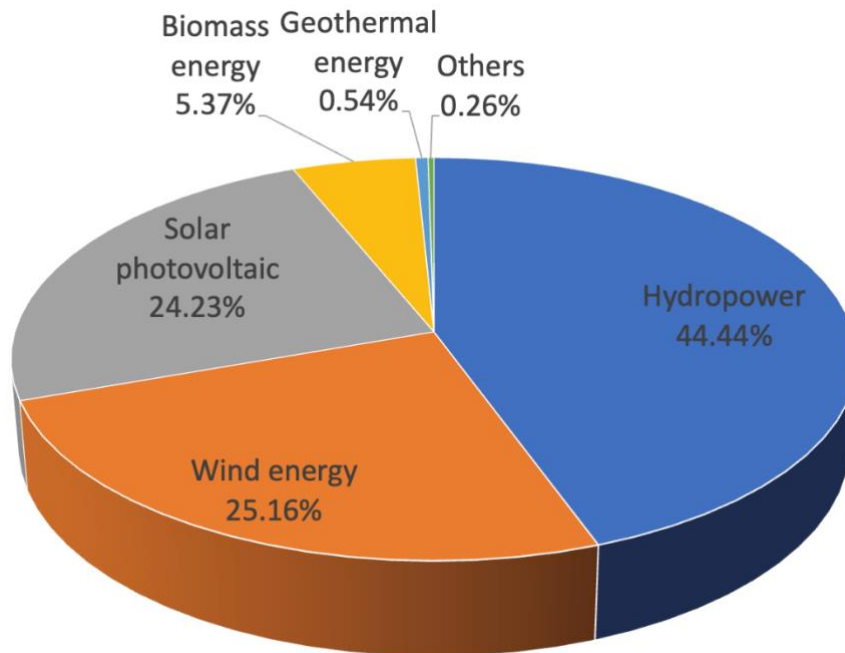


**Figure 1-2 - Share of renewable energy sources in electricity generation**

Energy storage system (ESS) is the technique to maintain stable power as well as to

match the generation with load requirement [7,8]. The renewable energies are stored beforehand in the system so that they can be utilized flexibly without being interrupted by climate [9]. In practice, the demand for energy storage system has been grown up rapidly, and would be tripled until 2030, which is attributed to economy's shift towards greener energy [10]. The energy storage systems are classified into various types according to the form of energy stored: Thermal, mechanical, chemical, electro-chemical, and hybrid energy. Among them, electrochemical energy storage is the most widely used system, because of its flexible energy and power configuration, low environmental impact, easy large-scale utilization, short construction period, and fast response [11]. Batteries are the devices used in the system to convert chemical energy to electrical one and are categorized into two groups depending on the rechargeability: Primary and secondary. The primary battery is the single-use battery with chemicals which cannot be recharged once consumed. On the other hand, secondary battery is highly preferred type in the industries due to its rechargeability and is classified depending on the material of electrodes and electrolyte [12]. In fact, various types of secondary batteries have been considered for the energy storage system, such as lead acid battery, lithium ion battery, sodium sulfate battery, and redox flow battery. Among them, the redox flow battery is one of the most promising secondary batteries due to its high capacity, the design flexibility, and long life cycle [13,14,15,16]. The first redox flow battery was invented by the Lewis Research Centre, National Aeronautics and Space Administration (NASA) with Fe/Cr redox couples in 1973 [17]. However, the battery had restrictions for commercialization because of the short life cycle as well as the low energy and power densities. In order to address those flaws, various redox couples have been tested exhaustively for alternative use, such as V/V, Zn/Br, Zn/Ce, V/Br, and V/Fe [18,19,20,21,22,23]. In particular, the vanadium redox flow battery is considered as a promising next-generation battery because of its safety and high

efficiency. The anolyte and catholyte contain compatible active species, vanadium ions, and thus the undesirable side-reactions are significantly diminished compared to other redox couples. In addition, research on porous electrodes has been conducted to enhance the electrochemical reaction between ions and electrode surface so that the higher power density and more efficient operation can be realized. Carbonized fibrous electrodes have been favored due to their high specific surface area, leading to the intensified current density [24]. However, the low permeability restricts the electrolyte transport in electrodes thereby requiring high pumping power for operation. In this thesis, the structure of the electrode in a vanadium redox flow battery is modified and analyzed exhaustively to enhance the electrolyte transport in electrodes so that higher overall efficiency can be attained.

## **1.2. Research Objectives and outline**

This thesis aims to provide ways of building novel structures of electrospun fibrous electrodes that enhance the power density of vanadium redox flow cell. As part of the effort, pristine electrospun samples were modified via compression and laser perforation, then subjected to a wide range of characterization and performance tests. For further analysis, a continuum-based modeling was implemented to observe the optimal multi-layered electrode structure in terms of physical properties of porous materials. Finally, the multi-layered electrode built with electrospun samples were evaluated experimentally.

This thesis consists of 6 chapters:

Chapter 1 contains the introduction on the background of vanadium redox flow battery and the research objectives.

Chapter 2 includes a literature review on the principle of vanadium redox flow battery. Especially, the experimental ways of observing physical properties of porous fibrous electrode were explained in detail. Also, past works investigating improving the efficiency of electrodes were discussed. Based on that, some qualitative metrics for describing the improvement in power density of redox flow cell was introduced.

Chapter 3 explains the way of modifying pristine electrospun electrode sample to achieve the novel fibrous structure. The properties of each sample were analyzed in both tomography images and experimental methods. The trend of change in power density of a redox flow cell as a function of physical properties of electrospun fibrous electrodes was discussed in detail.

Chapter 4 discusses 2-dimensional continuum scale modeling results from multi-physics simulation to predict the improvement of the cell performance with enhanced vanadium ion distribution in multi-layered fibrous electrode. The multi-layered structures were built in profiles of physical properties of fibrous electrode, including, fiber size, Carman-Kozeny constants, and porosity. The performance was evaluated with both gross power density generated from a redox flow cell and pumping power required for operation.

Chapter 5 explores ways of building multi-layered fibrous electrodes with commercial carbon felt and novel electrospun samples introduced in chapter 3 to optimize the power density of a vanadium redox flow cell. Each multi-layered electrode samples were tested in both flow-by and flow-through mode to confirm the importance of convective flow. In order to approach the analysis, two different flow field designs, parallel and interdigitated, were considered for evaluation.

Chapter 6 concludes contents of this thesis. Then, it summarizes the possibility of

future tasks to be done for further improvement of vanadium redox flow cell on top of the works discussed in this thesis.

## **2. Literature Review**

### **2.1. Mechanism of Redox Flow Battery**

Among the various batteries, the redox flow battery is one of the most promising secondary batteries for energy storage system due to its design flexibility attributed to the large adjustable capacity of the storage tanks filled with electrolyte solution. The redox flow battery can store the electrical energy through the chemical reaction induced by electroactive species, which are dissolved in liquid electrolytes. As can be seen in Figure 2-1, two separate external reservoirs containing electrolytes are connected to a cell stack. One of them is filled with catholyte while the anolyte is stored at the opposite side. The two half cells are separated by an ion exchange membrane, which is in general composed of nafion, to prevent the mixing of the redox-active ions while enabling the supporting electrolyte ions to pass through it. Also, nafion is a proton-conductive material, and thus the proton can be exchanged actively between two half cells to maintain electrical neutrality. The catholyte and anolyte in reservoirs are circulated through the separated compartments using pumps. After that, the redox couples in each compartment undergo electrochemical redox reactions on the carbonized electrode surface, the details of which will be discussed further in session 2.3. The current collector is located at each side of electrodes for the electron transfer after the reaction so that the current can be conducted from one cell to the other in the cell stack. Furthermore, bipolar plates act as partitions between compartments, and provide electrical connection from cell to cell in a battery [25]. Thus, it should be highly conductive while possessing proper chemical stability due to the highly acidic environment inside a vanadium redox flow battery.

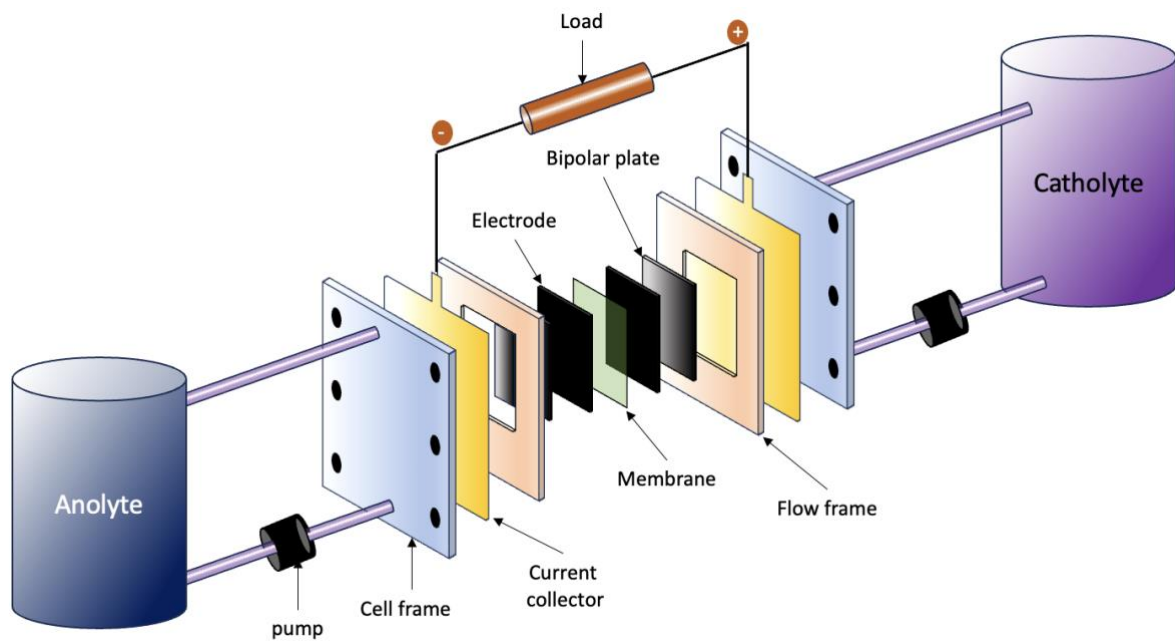


*Figure 2-1– Schematic representation of vanadium redox flow battery [7]*

In practice, energy and power densities are the most important performance factors of redox flow batteries [26]. The energy density relates to the concentration of electroactive species stored in electrolytes. The high concentration enables a greater number of electrons to be produced and exchanged between anolyte and catholyte at a given volume of electrolyte, resulting in high capacity as well as energy density. The power is in fact proportional to the number of cells in stacks. However, the higher cost and the volume would be required to increase the number of cells. Thus, it is a challenge to improve the electrochemical reaction between electrodes and active species in electrolytes. One possible way is increasing the volumetric surface area of active site in electrodes to accelerate the reaction rate, and it is the main objective of projects introduced in this thesis.

## 2.2. Redox Couples

In the case of redox flow batteries, all the active materials are stored in electrolytes.

The electroactive species are dissolved in aqueous solution in its oxidized and reduced states. Many researchers attempted various redox couples depending on the purpose of their research. Table 2-1 shows the list of proposed redox couples in a flow battery with their cell voltage.

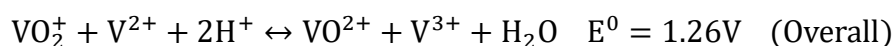
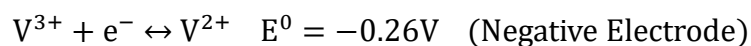
**Table 2-1 – Redox couples attempted for flow cell**

<b>Redox species</b>	<b>Cell voltage (V)</b>	<b>Reference</b>
<b>Cr<sup>3+</sup>/Cr<sup>2+</sup>, Fe<sup>3+</sup>/Fe<sup>2+</sup></b>	1.2	[27]
<b>Cr<sup>3+</sup>/Cr<sup>2+</sup>, Br<sup>2+</sup>/Br</b>	1.44	[28]
<b>V<sup>3+</sup>/V<sup>2+</sup>, ClBr<sup>2-</sup>/Br<sup>-</sup></b>	1.3	[29]
<b>V<sup>3+</sup>/V<sup>2+</sup>, Ce<sup>4+</sup>/Ce<sup>3+</sup></b>	1.87	[30]
<b>Zn<sup>2+</sup>/Zn, Ce<sup>4+</sup>/Ce<sup>3+</sup></b>	2.04-2.48	[31]
<b>V<sup>3+</sup>/V<sup>2+</sup>, VO<sub>2</sub><sup>+</sup>/VO<sup>2+</sup></b>	1.26	[32]

Unfortunately, each redox couple has flaws, which are remained as future works to be resolved. Chromium is utilized as one of the species but tends to slow down the reaction, resulting in low power density. Especially, in the case of Cr/Fe couple, Chromium ions' redox potential and the hydrogen gas generation potential are close to each other, which causes H<sub>2</sub> evolution at negative electrodes at the end of charging process, there by further decrease in battery capacity. Thus, the system needs to be re-balanced to compensate it. Zn/Ce is the couple recently suggested due to significantly high cell voltage. However, the huge electrode potential difference between redox reactions requires a careful selection of materials to avoid any degradation. Another flaw is that the cathode needs to be made of expensive platinized-titanium to oxidize or reduce cerium. Also, low battery capacity with O<sub>2</sub> and H<sub>2</sub> evolution

side reactions need to be resolved [33].

Vanadium ion has been considered as the most representative species at the present time. In particular, the vanadium redox flow battery with V/V couple is considered as a promising next-generation battery because of its safety and high efficiency. In practice, when catholyte and anolyte contain different species, the battery capacity tends to reduce rapidly as repeating charge/discharge cycle due to the cross-contamination through a membrane. Unlike other redox couples, catholyte and anolyte contains the same electroactive element for this couple, which mitigates any undesired side reactions caused by the inevitable ion-crossover. In addition to that, the reaction with vanadium redox couple does not provide any toxic vapors or gases. Thus, vanadium redox flow battery is liberated from any explosion and very little environmental impact compared to other secondary rechargeable systems, such as Li-ion battery. The anolyte contains  $V^{2+}/V^{3+}$  couples, while  $VO_2^+/VO^{2+}$  coupled ions exist in the catholyte. During the charging process,  $V^{3+}$  is reduced to  $V^{2+}$ , whereas the  $VO^{2+}$  is oxidized to  $VO_2^+$ . The reactions are entirely reversed for discharging.



In practice, the vanadium redox flow battery is not yet widely deployed owing to its low power and energy densities compared to lithium-ion batteries, which are commercially used in many application as illustrated by Chai et al [34]. However, the use of lithium-ion batteries is hindered due to its high cost, safety issues, and environmental concerns [35,36]. Also, the power and energy densities of lithium-ion batteries are limited for further

improvement because of the intrinsic specific capacity of the state-of-art electrodes. For this reason, the vanadium redox flow battery has been attended as one of the most promising secondary batteries for replacement.

Electrolyte is one of the key components affecting the overall performance and cost of vanadium redox flow battery [37]. It accounts for 50 % of the total cost of the battery. In practice, one of the main factors restricting the commercialization of vanadium redox flow batteries is the high cost of vanadium ions [38]. The energy density of the battery mainly depends on the solubility of vanadium ion in electrolytes, and the current solubility is defined as 1.6 – 2.0 M. Many researchers are focusing on developing additives to increase the solubility thereby enhancing energy and power density of the battery [39]. However, the high cost would be an additional issue since an excess amount of vanadium ions is required to approach more concentrated electrolytes.

The membrane is another part determining the cycle performance and economic feasibility. It not only isolates anolyte and catholyte to prevent cross-contamination but also allows proton transport to maintain electrical neutrality [40]. At present, Nafion and Daramic are the common materials used for a membrane because of their high proton conductivity [41]. Many researchers invested in developing new materials, additives, and preparation processes for advanced performance [42]. In practice, the economic feasibility has been improved with advanced membranes attributed to reduced contamination, thereby the low cost of electrolyte replacement. However, the power and energy densities were not significantly affected.

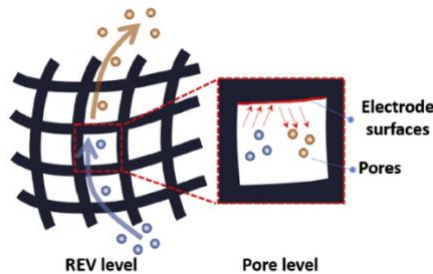
Lastly, the electrode is the main compartment affecting the power density. It is because of the loss of power density caused by polarization and mass transfer delays, which relate to the properties of electrodes [43]. Fortunately, the performance of a redox flow battery can be

improved by modifying the structure of the electrode. In practice, the carbonized electrode in a redox flow battery plays three roles: the path of electrolyte, the active site for electrochemical reaction, and the path of electrons. Thus, its chemical and physical properties, such as permeability, ionic conductivity, and catalytic activity, act as important factors for power density. The goal of the projects introduced in this thesis is to develop novel structures of electrodes, which can improve in all those factors simultaneously. The principles and mechanisms will be discussed in detail in the next sections.

### 2.3. Material and Role of Electrode

In general, polyacrylonitrile (PAN), Rayon-based carbon, or graphite felt is considered as the material for electrodes in a vanadium redox flow battery [8]. Among them, PAN is the most popular polymer due to its high electrical conductivity with abundant carbon contents, high chemical and electrochemical stabilities, and acid resistance [44,45,46]. Sun found that the surface oxygen functional group on the carbonized PAN electrode are utilized as active sites for the reaction [47]. In the aspect of the positive electrode, while charging the battery, the oxidation reaction occurs between  $VO^{2+}$  ions in the catholyte and the electrode surface. As a first step, the ion is exchanged between  $VO^{2+}$  ions and the  $H^+$  ions of the phenolic functional group in the carbonized PAN. After that, the oxygen atom from the C-O functional group in the PAN combines with  $VO^{2+}$  to form  $VO_2^+$ , while the electron moves from  $VO^{2+}$  to the C-O-V bond on the electrode surface. Finally, the  $VO_2^+$  formed on the electrode surface undergoes the ion-exchange with the  $H^+$  ions in the catholyte. All those steps are reversed during the discharging process. The identical mechanism arises between the anolyte and the surface of the negative electrode, but the reduction reaction from  $V^{3+}$  to  $V^{2+}$ . Figure 2-2b)

and c) illustrates each step of the reaction in detail. After the reaction, the PAN fibers are utilized as the path of electrons to be transferred into current collectors, as indicated in Figure 2-3. Then, the electrons pass through the power load in Figure 2-1 to provide electric potential.



(a)

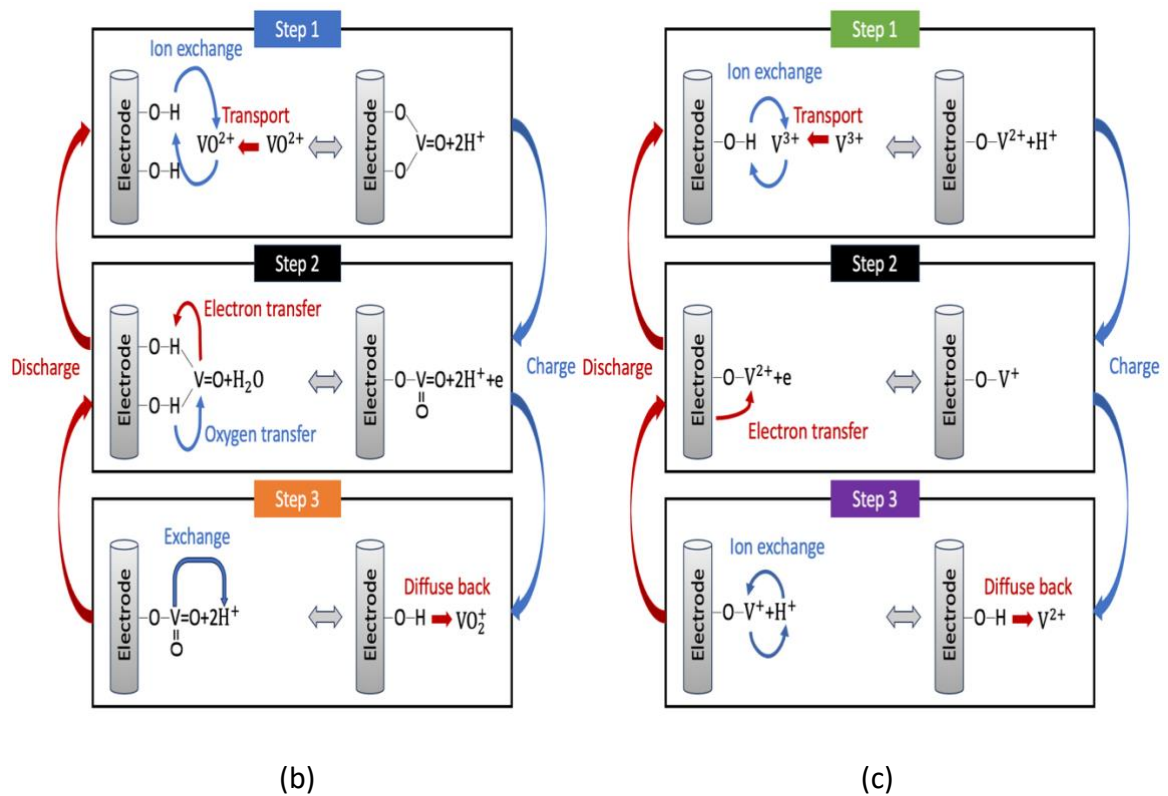


**Figure 2-2-a) Schematic of mass transport of active species through a porous electrode. b) Schematic illustration of redox reaction mechanism on surface of cathode, c) on surface of anode [7]**

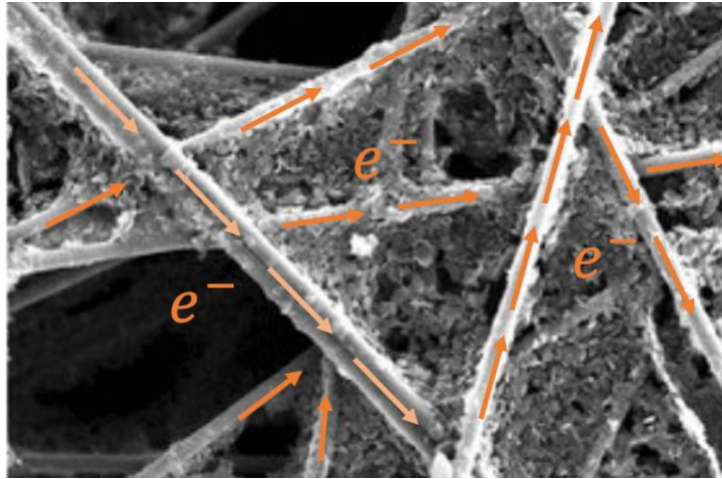


*Figure 2-3 - Structure of fibrous electrode in vanadium redox flow battery [48]*

#### **2.4. Porous Electrode**

In benchtop studies of electrochemical systems, it is common to use planar electrodes of the material of interest (i.e. carbon or alloy). In practical applications however, it is necessary to increase the surface area of the electrode which directly increases the realizable rate of reaction and current output of the system. In most practical batteries, including flow batteries, this is accomplished by using a porous electrode. The performance of porous material in each application is highly dependent on its structural properties, stressing the importance of carefully designing the porous structure. In particular, carbonized porous fibrous materials have shown promise for use as electrodes in electrochemical devices because of their high specific surface area for reaction, high porosity to support flow and diffusion, and good electrical conductivity through the interconnected fibers. One common characteristic of porous materials is their high porosity, usually exceeding 85%. In some cases, it may be desirable to have a lower porosity which will yield a higher volumetric surface area.

In the case of redox flow battery, the internal pores of the electrode provide a massive increase in additional surface area where reaction can occur for a given volume. Also, the

pores among carbonized fibers act as the path of the flowing electrolyte. Vanadium ions in electrolytes transport through the path and undergo electrochemical reaction on fiber surfaces to provide electrons during the charging or discharging process, as depicted in Figure 2-2a) [49]. Thus, the challenge when using a porous electrode becomes effective delivery of reactants deep into the core of the porous domain, which is the central theme of this thesis.

#### 2.4.1. Electrospinning

Production of carbon-fiber layers has been discussed at length in various articles [50,51,52,53]. Generally speaking, the fibers are about 10  $\mu\text{m}$  in diameter because this fiber size is commercially mass-produced for multiple uses, such as reinforced composites. However, moving to much smaller fiber sizes is of interest since the surface area increases exponentially. One option is to use electrospinning, which is convenient for laboratory studies and has the potential for scale-up to large volume production. Another advantage is that various kinds of polymers can be electrospun depending on the application. In practice, electrospun materials have been applied to various electrochemical devices, such as anodes and separator in lithium-ion batteries [54,55,56,57,58,59], the gas diffusion layer (GDL) in a polymer electrolyte membrane fuel cell [60], and electrode in flow batteries [61]. Especially, Liu et al [24] have employed an electrospinning technique to fabricate electrodes containing much smaller fibers to overcome low power density of a vanadium redox flow battery.

Electrospinning is a popular method to fabricate random fibrous material and is highly customizable depending on the desired condition. It is accomplished by applying an electric field between the needle and the collector plate to draw charged threads from polymer solutions, as can be seen in Figure 2-4. The polymer dissolved in a liquid solution is stored in a syringe and is pumped through the needle having a small diameter. In the meantime, the DC

potential higher than 10 kV is applied to the needle. Then, the electrostatic repulsive force between polymer molecules in the solution counteracts the surface tension, which leads to create a cone at the tip of needle. This phenomenon was theoretically examined by Taylor et al [62] and the cone observed at the tip of the capillary needle is known as the Taylor cone. When the high enough electrostatic repulsive force is approached, a jet of solution is expelled towards the grounded collector in a fibrous shape. The electrostatic field causes instability, which leads the filament shear and whip as solvent evaporates. Thus, the fiber is deposited continuously in random pattern on the collector.

In the case of vanadium redox flow battery, PAN particles are dissolved in N,N dimethylformamide (DMF) to make a solution for electrospinning. According to Liu et al [24], the fiber size is determined by the wt % of PAN in the mixture, as can be confirmed through SEM images in Figure 2-5.

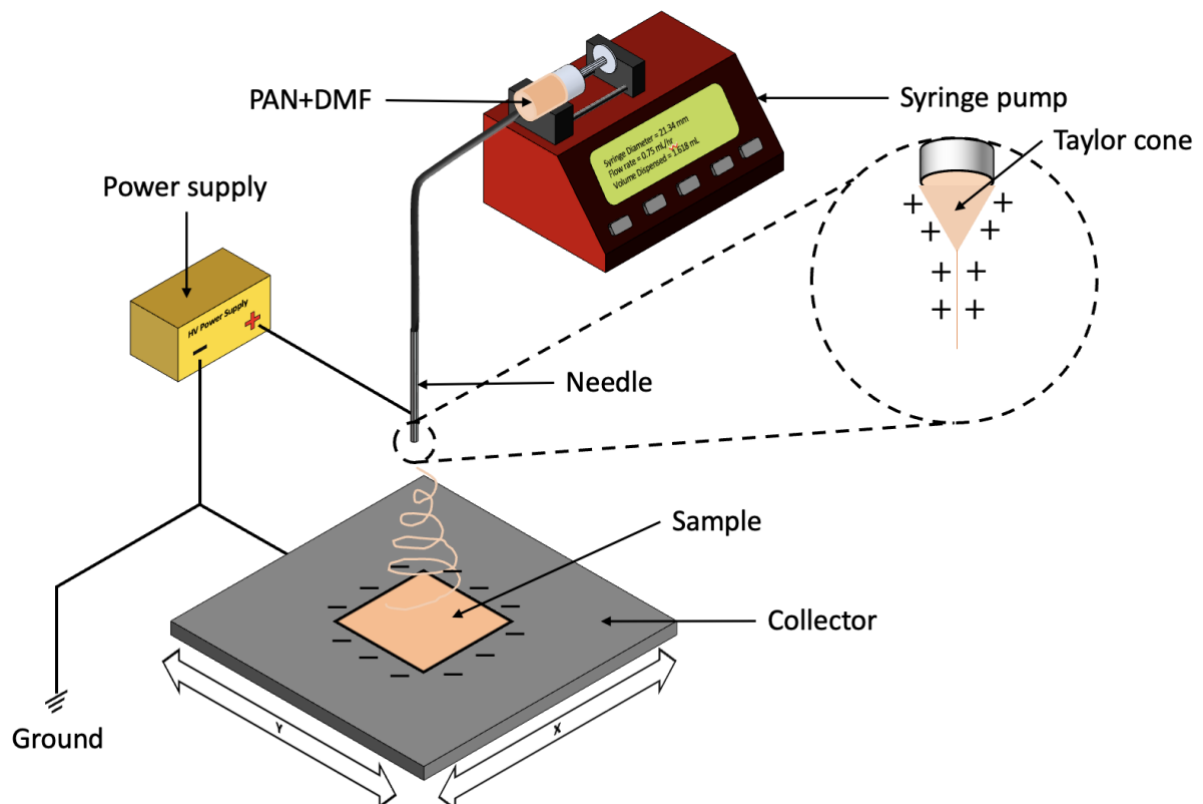


**Figure 2-4 – Design of electrospinner**

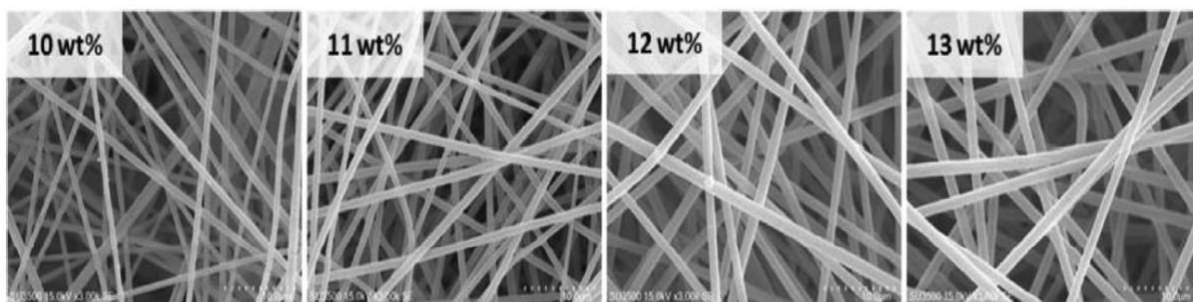


**Figure 2-5 – SEM images of electrospun fibres with different wt% of PAN in the mixture. The scale bar on each image is 10  $\mu\text{m}$ .**

#### 2.4.2. Stabilization and Carbonization

The electrospun PAN fibers then require two different heat treatment processes prior to the application to redox flow cells: stabilization and carbonization. The stabilization is implemented in an oxidative environment at the temperature between 200 and 300°C [63]. The linear macromolecules of PAN are transformed into a rigid form, leading the high thermal stability [64]. The stabilized PAN fiber is then carbonized at the temperature ranging from 1000 to 1700°C [65]. The non-carbon elements are detached during this process, rendering a relatively pure carbon framework, as depicted in Figure 2-6. In this way a carbon-fiber electrode with sub-micron pores can be made with customized properties.

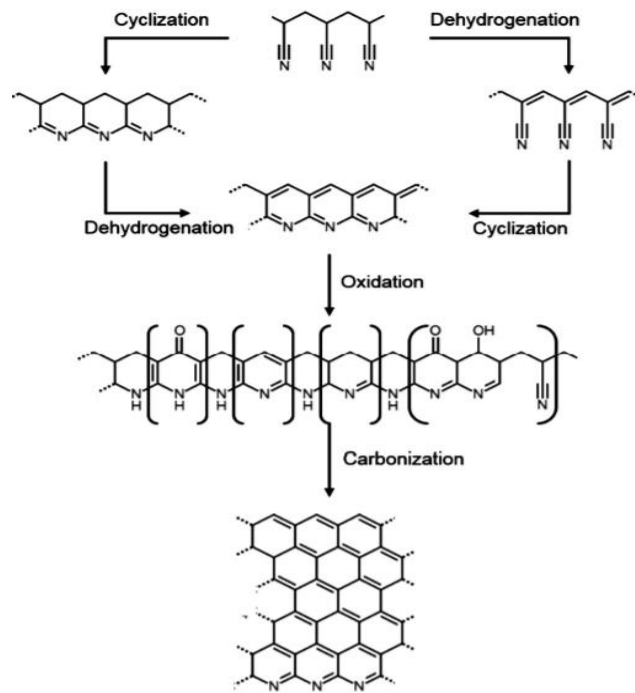


**Figure 2-6 - Change in the structure of polyacrylonitrile during stabilization and carbonization [62]**

In practice, due to the loss of atom, the fiber size tends to reduce during stabilization and carbonization stage, as can be confirmed in Figure 2-7. The problem is that the fibers cannot be made extremely small since this drastically reduces the permeability, constraining the electrolyte transport or increasing the parasitic pumping costs [61,66,67]. Therefore, in order to optimize the cell performance, a path forward is to develop a way of arranging fibers so that sufficient permeability can be retained while maintaining the small fiber size.



**Figure 2-7 - Electrospun polyacrylonitrile (PAN) material before and after carbonization [24]**

## 2.5. Properties of porous electrode

There are several properties to be considered to optimize the efficiency and performance of a porous electrode. When the liquid electrolyte is pumped through the porous electrode, pressure-driven flow through a porous domain is described by Darcy's law:

$$Q = \frac{KA}{\mu L} \Delta P \quad 2-1$$

where  $Q$  is the volumetric flow rate of electrolyte,  $A$  is cross sectional region of electrode,  $\mu$  is the dynamic viscosity,  $L$  is the length of the electrode, and  $\Delta P$  is the pressure drop across the electrode. In practice, the pressure drop relates to the pumping power required to operating a vanadium redox flow battery, which is calculated using Eq.2-2 derived by Zhang et

al [68].

$$P_{pump} = \frac{2 * Q * \Delta P}{\psi_{pump}} \quad 2-2$$

where,  $P_{pump}$  is the pumping power, and  $\psi_{pump}$  is the efficiency of the pump. Therefore, reducing the value of  $K$  in Eq.2-1 leads directly to an increase in operating cost, since the  $\Delta P$  will be greater for a given  $Q$ . Using thicker and shorter electrodes would also affect this goal, but assuming geometry is fixed, only  $K$  can be manipulated, which requires altering the structure of the electrode.

The permeability of a fibrous porous material is well correlated by the Carman-Kozeny relationship [61]:

$$K = \frac{d_f^2 \varepsilon^3}{16k_{CK}(1 - \varepsilon)^2} \quad 2-3$$

where  $K$  is the permeability coefficient, and  $k_{CK}$  is the fitting parameters, which accounts for the material structure, such as fibre morphology and shape. According to the Carman-Kozeny theory, there are thus 3 ways to increase the permeability of porous electrode: increase the porosity, increase the fiber size, or change  $k_{CK}$ .

The specific surface area of the fibrous electrode can be estimated by assuming the continuous filament. The total length of the fiber in the electrode can be calculated using Eq.2-4

$$L = \frac{V_s}{A_c} = \frac{V_b(1 - \varepsilon)}{\frac{\pi}{4} d_f^2} \quad 2-4$$

where  $V_s$  is the total volume of fibre,  $A_c$  is the cross-sectional area of the fibres,  $V_b$  is the bulk volume of electrode,  $\varepsilon$  is the porosity,  $d_f$  is the diameter of fibre. The specific surface area of the electrode can be obtained from Eq.2-5.

$$A_s = \frac{\pi d_f L}{V_b} \quad 2-5$$

By substituting Eq.2-4 into Eq.2-5, the specific surface area is expressed, as shown in Eq.2-6.

$$A_s = \frac{4(1 - \varepsilon)}{d_f} \quad 2-6$$

Eq.2-6 indicates a reverse correlation between specific surface area and fiber size. It means that decreasing pumping power can be accomplished by increasing the fiber size but has a negative impact on the reactive surface area. The porosity is already quite high for fibrous structure (>85%). This leaves the  $k_{CK}$  value, which requires changing the physical arrangement of the solid structure.

Lastly, when considering the fibrous electrode structure, it is necessary to determine how effectively ions can diffuse. This combination of convective and diffusive mass transport in porous media is called 'dispersion'. Ions in the electrolyte diffuse spontaneously due to the concentration gradient, and transport also occurs because of the mechanical mixing caused by the morphology and structure of the pore space in porous media. As can be seen in Figure 2-8, the heterogeneity of streamline for each ion due to the irregular pattern of porous structure changes the direction of flow, indicating that the dispersion is impacted by pore scale process, but it is actually a continuum scale parameter that encapsulates these pore scale effects. In the case of fibrous electrode, the dispersion exists in two different directions. The dispersion in the direction parallel to the geometrical surface of an electrode is called longitudinal dispersion, while the one in the perpendicular direction is transverse dispersion. The dispersion is thus one of the key indicators to evaluate the performance of porous fibrous electrode.

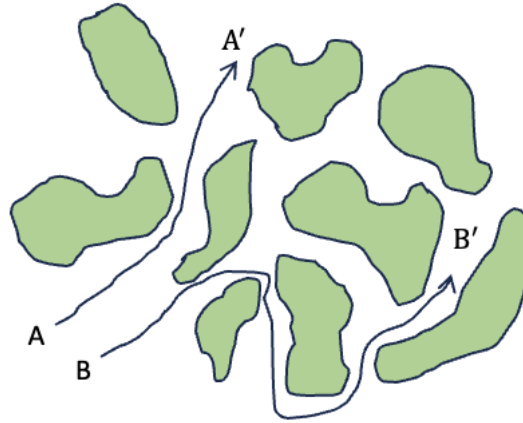


*Figure 2-8 – Pore-scale mechanisms resulting in macroscopic dispersion coefficients*

## 2.6. Electrode characterization methods

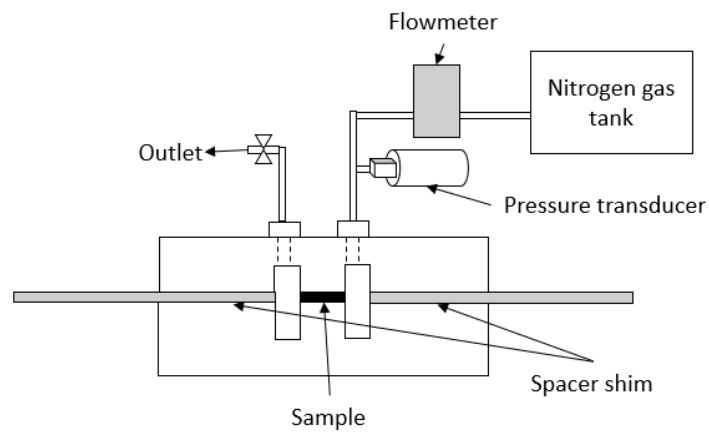
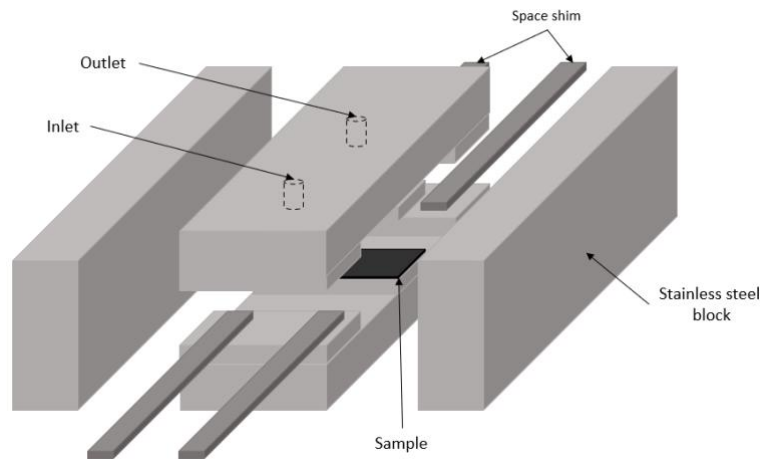
### 2.6.1. Permeability

The permeability is the most significant characteristic that needs to be measured prudently since it crucially determines the efficiency of flow in porous media. In general, the permeability of the porous material,  $K$ , is measured by the Carmen-Kozeny theory, as shown in Eq.2-3. In fact,  $k_{CK}$  depends on various properties and the structure of porous media, and thus it is quite difficult to find sufficient value. Therefore, Darcy's law is alternatively applied for the experimental measurement. However, when gas phase, nitrogen gas for instance, is used as a tracer, Eq.2-1 would be modified to Eq.2-7 [24].

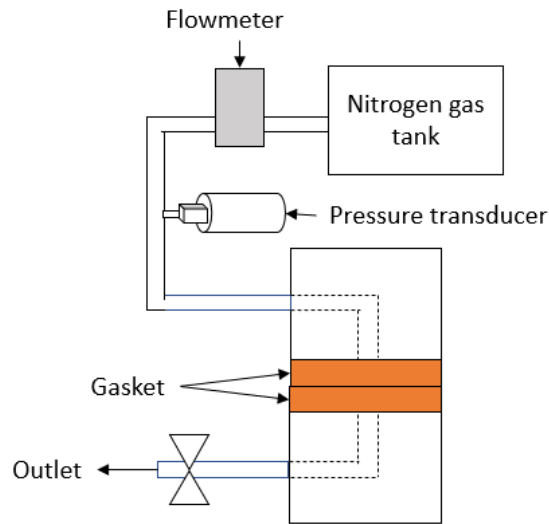
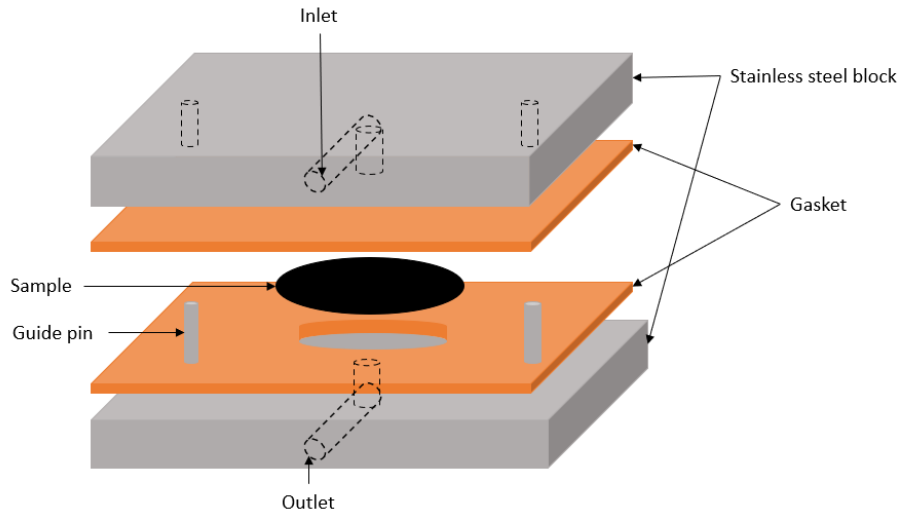
$$m = \frac{KA}{\mu} \left( \frac{P_{IN}^2 - P_{OUT}^2}{\frac{2LRT}{MW_{N_2}}} \right) \quad 2-7$$

where  $m$  is the mass flow rate,  $A$  is the cross-sectional area,  $\mu$  is the dynamic viscosity,  $P_{IN}$  is the inlet pressure,  $P_{OUT}$  is the outlet pressure (1atm),  $L$  is the length of the sample,  $R$  is the gas constant,  $T$  is the temperature, and  $MW_{N_2}$  is the molecular weight of nitrogen gas. Figure 2-9 shows the experimental set-up for the permeability measurement. The nitrogen tank is

connected to the inlet boundary, and the flow rate of nitrogen gas is controlled by the flowmeter. The inlet pressure is measured using the transducer installed, while the atmospheric pressure is maintained at the outlet boundary. The thickness of the sample is adjusted by the stainless-steel spacer shim.



a)



b)

**Figure 2-9 – Experimental set-up for a) in-plane, and b) through-plane permeability measurements**

### 2.6.2. Porosity

The porosity presents the fraction of the void volume in the porous media. One of the decisive reasons for the fibrous electrode application in the vanadium redox flow battery is the outstanding permeability, attributed to the high porosity. In this study, buoyancy method was used to measure the porosity of each sample. According to Archimedes principle, the object loses its weight when submerged in a fluid by the weight of the fluid that it displaces,

and Eq.2-8 is applied to obtain the solid density of the sample.

$$\rho_s = \rho_L \frac{m_{dry}}{m_l} = \rho_L \frac{m_{dry}}{m_{dry} - m_{wet}} \quad 2-8$$

where  $\rho_L$  is the liquid density,  $m_{dry}$  is the dry weight of the sample,  $m_l$  is the weight of liquid displaced, and  $m_{wet}$  is the weight of the submerged sample. In this study, the sample, cut into the size of 7/8" in diameter, is submerged into the silicone oil, having a density of 0.96 g/mL. Then, the solid volume and porosity are calculated using Eq.2-9 and 2-10.

$$V_s = \frac{m_{dry}}{\rho_s} \quad 2-9$$

$$\varepsilon = 1 - \frac{V_s}{V_b} \quad 2-10$$

where  $V_s$  is the solid volume, and  $\varepsilon$  is the porosity of the sample.

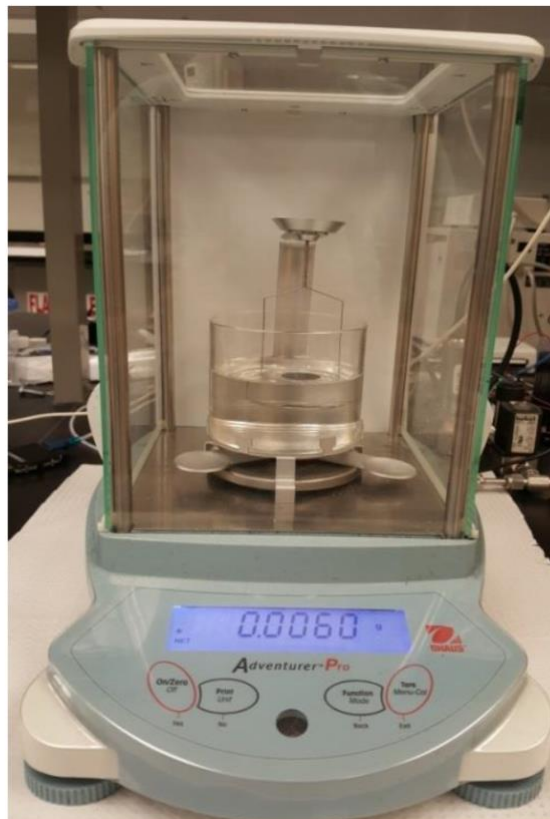


**Figure 2-10 – Porosity measurement set-up**

### 2.6.3. Specific Surface area

Although the sample with the greater pore size provides the advantage in the pumping cost, it would contain relatively the lower specific surface area. As discussed earlier, surfaces of fiber in electrodes act as catalytic surface for reaction, and thus the reaction rate highly depend on the fiber surface area. In other words, it is important to make a balance among pore size, permeability, and specific surface area of the porous material to optimize the cell performance. The experimental technique to measure the internal surface area of porous material is called gas physisorption. The fibrous electrode sample is placed on the holder located inside the chamber filled with specific gas. Then, the pressure inside the chamber is increased slowly to induce the gas molecules adsorb on top of fiber surface. The total cross-sectional area of gas molecules adsorbed in the monolayer reveals the surface area of the sample, as shown in Eq.2-11.

$$A = n_m \times a_{gas} \times N_{Av} \quad \mathbf{2-11}$$

where  $A$  is the total internal surface area of sample,  $n_m$  is the number of gas moles adsorbed in monolayer,  $a_{gas}$  is the cross-sectional area of each gas molecule, and  $N_{Av}$  is the Avogadro's number. The number of gas molecules in monolayer can be extracted using the theoretical equation developed by Brunauer-Emmett-Teller (BET).

$$\frac{\frac{p}{p^o}}{n_{ad}(1 - \frac{p}{p^o})} = \frac{1}{n_{ad,m}c} + \frac{c-1}{n_m c} \frac{p}{p^o} \quad \mathbf{2-12}$$

where  $p$  is the pressure inside chamber,  $p^o$  is the saturation vapor pressure of the adsorbing gas,  $c$  is the BET constant,  $n_{ad}$  is the total number of gas moles adsorbed, and  $n_{ad,m}$  is the number of gas moles adsorbed in a monolayer. In practice, the gas tends to condense in corners and crevices of the sample at relative pressure ( $p/p^o$ ) less than 0.05. Also, gas starts to condense at bulk space of the chamber when  $p/p^o$  is higher than 0.3. Consequently, the

experimental data collected at  $p/p_o$  ranging from 0.05 to 0.3 is considered in general for accuracy. In this thesis, the vapor sorption analysis was performed using a Dynamic vapor sorption (DVS) Resolution device from Surface measurement Systems, which shown in Figure 2-11.



*Figure 2-11 – Dynamic vapor sorption (DVS) resolution device*

## 2.7. Polarization behavior

The polarization behavior is an important source to determine the power density of the redox flow cell, which is calculated by multiplying current density and cell potential, as shown in Eq.2-13.

$$p_{cell} = i * V \quad 2-13$$

Where  $p_{cell}$  is the power density,  $i$  is the current density,  $V$  is the potential of the flow cell. In practice, the potential of the flow cell is usually lower than its open-circuit voltage because of the irreversible losses occurred from the flow of current. For this reason, the potential at

each current density is lower than theoretical value, rendering low power density. In the case of the flow cell, the polarization behavior is critically affected by the structure of porous electrode installed. Typically, there are three different types of polarization loss depending on ranges of current region: activation, ohmic, and mass transfer losses, as shown in Figure 2-12.

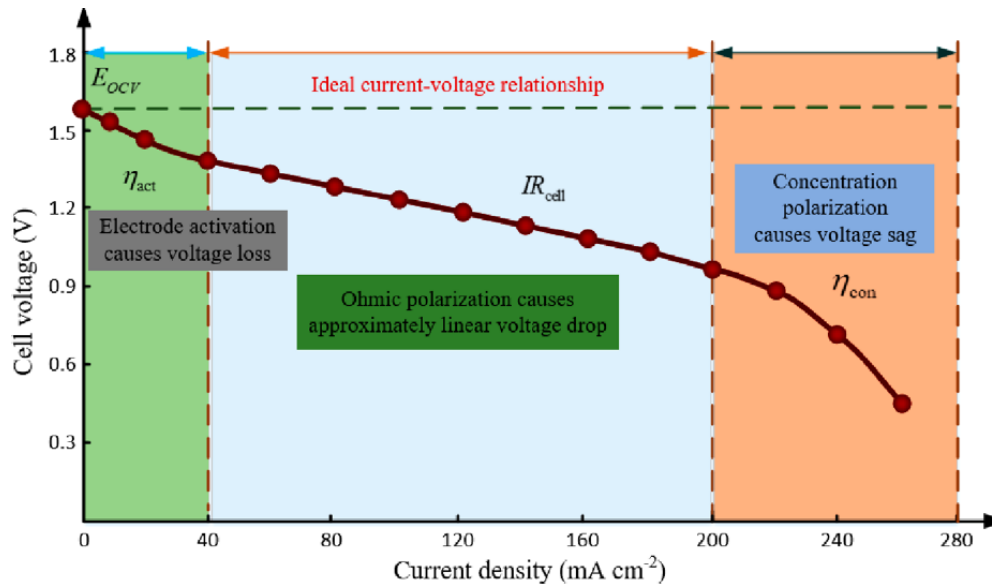


**Figure 2-12 – Polarization behavior from general redox flow cell [69]**

The activation polarization is the cell potential loss occurring at low current density, which is influenced by the electrochemical reaction rate or reaction kinetics. As discussed earlier, the fiber surfaces in electrodes are utilized as an active site for reaction. The reaction rate will be accelerated as greater surface area of fiber is utilized, resulting the system to be less limited by the reaction rate. In other words, the activation polarization of flow cell can be remediated as increasing the fiber surface area when the same material was used for manufacturing the electrode.

The ohmic polarization occurs in the intermediate region of current density. The ohmic loss is attributed to the resistance provided from various cell compartments, which restricts ion and electron transports. Specifically, electron transport is related with the structure of fibrous

electrode. In practice, the ions, such as vanadium and protons, transport through the liquid phase, and thus the properties of electrolyte act as important role. On the other hand, the solid phase of fibers in electrodes is utilized as a path of electron. In other words, the electron can smoothly transport depending on how fibers are structured. One way of enhancing the electron transport would be acquiring the greater number of interconnections among fibers.

Lastly, the mass transport polarization is the most important one since it happens at high current density where the optimal power density occurs. It is in fact opposite to the activation polarization and mostly related with the ion transport in porous electrodes. If the introduction rate of species into the electrode is not high enough compared to the consumption rate from the reaction, the system would be limited by mass transport and provides serious polarization loss. In practice, the introduction rate of species is affected by the permeability of electrode. According to Darcy's law, in the case when the identical pressure drop is applied, the electrolyte would be introduced at higher rate with the porous electrode having a higher permeability. In other words, comparatively the less mass transport loss would occur. Oppositely, when the identical flow rate of electrolyte was applied, the electrode with higher permeability will provide a lower pressure drop, which remediates required pumping power for operation. Thus, it would be a challenge to make a balance between pumping power and the degree of mass transport polarization to optimize the cell performance.

## **2.8. Flow channel**

### **2.8.1. Types of Flow Channel Design**

In the past, the redox flow battery was operated with flow-through electrode configuration [49]. The flow-through electrode is the basic design, which directly introduces the electrolyte into the electrode by the forced-convective flow, and thus, provides the outstanding mass

transportation [70]. However, it requires a thicker electrode to minimize the pressure drop across the cell, incurring the critical ohmic loss. In order to mitigate this flaw, the flow channel has been recently introduced beside electrodes in the vanadium redox flow battery. In practice, the flow channel has three different roles [71,72,73,74]. Not only the electrolyte is distributed on the electrode surface effectively with the field, but also the channel is utilized as a path of the electron transfer to current collectors. Lastly, the channel facilitates heat management to avoid the explosion attributed to overheating. In the case of the vanadium redox flow battery, the latter two functions are eminent at the present time. However, the performance is limited due to the lack of the first function. The battery undergoes a substantial mass transport polarization due to the non-uniform ion distribution in porous electrodes [75]. Thus, in addition to the catalytic activity, it is crucial to design the appropriate flow channel. In the present time, four different designs of the flow channel have been investigated, which are serpentine, parallel, interdigitated, and spiral, as shown in Figure 2-13.

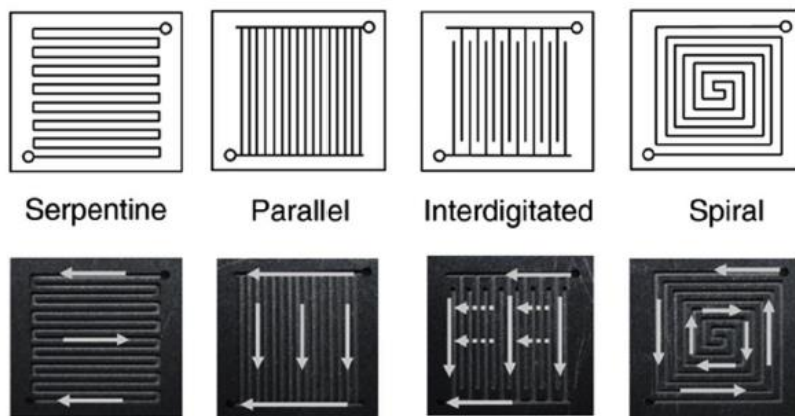


**Figure 2-13 – Designs of flow channel in the Vanadium Redox Flow Battery [75]**

Among them, the parallel channel is a basic design, which is operated in flow-by mode. Flow-by operation relies on passive mass transfer into the porous electrode via diffusion, which has low mass transfer rates but has the benefit of low pressure drops since fluid is flowing in

relatively large channels, and therefore lower pumping costs. However, it does not provide a sufficient convective force, incurring the limited ion distribution in the electrode and inadequate cell performance. In contrast, the serpentine design provides slight convective flow under the rib due to the pressure difference between paths. However, the convective force is not strong enough to induce proper ion distribution in electrodes while much higher pressure drop is required due to the intense long and single path [76]. The flow-through mode with interdigitated flow field is the most promising option. Unlike other designs, the cell with interdigitated flow field forces electrolyte directly into the pore spaces of the porous electrode by convective flow. Therefore, the greater portion of fiber in electrodes can be utilized as active site. In addition to that, the total length of the path is relatively short, leading to the low overall pressure drop [77,78,79,80,81]. However, the pressure drop tends to increase rapidly as smaller pores among fibers are created in electrodes. The spiral flow contains two different entwined spiral paths. The electrolyte is introduced from the edge of the channel and flows through the center of the electrode. After that, the flow changes the direction back to the rim of the channel. In other words, neighboring channels shares fresh and depleted electrolyte, and this phenomenon attains the uniform distribution of vanadium ions. However, the long-interlaced flow path requires relatively the high pressure drop, likewise in the case of the serpentine one. Thus, it provides a worse performance compared to the interdigitated design in terms of both electrochemical performance and pressure drop [74].

## **2.9. Past Works**

In the past, as discussed in the previous session, commercially available carbon-paper, typically used for the gas diffusion layer of proton exchange membrane fuel cells, was utilized

as a common material for the electrode of vanadium redox flow battery. However, the commercial carbon-paper has a relatively low specific surface area due to the large fibers ( $\sim 10\ \mu\text{m}$ ). Recently, an electrospinning technique has been employed to fabricate electrospun fibrous electrode with much smaller fibers to overcome this flaw. However, the fibers cannot be made extremely small since this drastically reduces the permeability, constraining the electrolyte transportation or increasing the parasitic pumping costs (61,66,67). Therefore, in order to maximize the cell performance, a path forward is to develop a way of arranging fibers so that sufficient permeability can be retained while maintaining the small fiber size.

Recent research has been focused on increasing the specific surface area of active site via surface modification of fiber. Maleki et al [82] suggested loading carbon-black particles into the mixture of N,N dimethylformamide/polyacrylonitrile to make electrospun fibers. The carbon-black particles tended to be oriented along the diving voltage during the electrospinning process and thus provided the elongation effect of the fluid jet. Accordingly, the carbon-black particles increased the surface roughness of fibers and constructed extra pores on fibers. In other words, the additional active site could be built on the electrode surface. However, the smaller inter-fiber distance and thus the smaller pores limited the mass transportation of the electrolyte. As a result, inevitably, the lower Coulombic and energy efficiency were attained compared to the case without carbon-black loading. Similarly, Zhou et al [83] provided dual-scale porous electrode by etching fibers with potassium hydroxide, leading to the increased specific surface area but did not circumspectly analyze the electrolyte transportation altered by the roughed surface of fibers. Shao et al [84] investigated nitrogen doping by releasing  $\text{NH}_3$  into the atmosphere during heat treatment of the mesoporous carbon electrode. The nitrogen doped carbon tended to possess high positive charge density.

Thus, the positively charged electrode was utilized as reinforced active sites for the oxidation reaction, meaning electrons could be transferred from electrolyte to electrode. Furthermore, valence electrons of nitrogen atoms provided additional charge to  $\pi$  bonds in graphene layers, leading to an enhanced electrical conductivity. However, the effort did not significantly affect the mass transportation of electrolytes. Overall, their works showed evident enhancement on electrochemical reaction rate with high specific surface area but could not overcome the low efficiency of electrode caused by the limited mass transportation of ions.

Instead of altering surface conditions, there have been recent attempts to produce electrodes with small fiber sizes, while enhancing the ability of fluid to flow through the structure. Yadav et al [85] worked on modifying the morphology of electrospun fibers from the cylindrical to ribbon cross-sectional shape using the coaxial electrospinning technique. The core-shell structure was fabricated by introducing the polystyrene into the center of the fiber, while the shell is formed with polyacrylonitrile. The polystyrene was extracted by submerging the electrospun fiber into liquid chloroform, rendering the hollow core to be collapsed into ribbons. As a result, the specific surface area was doubled compared to the original cylindrical fibrous electrode, yet the permeability remained high since the fibers occupied less pore space. However, the low through-plane permeability provided serious mass transport polarization loss.

As is evident from the literatures, it is challenging to accomplish both high specific surface area and high permeability simultaneously, due to their inverse correlation.

## **2.10. Research Target**

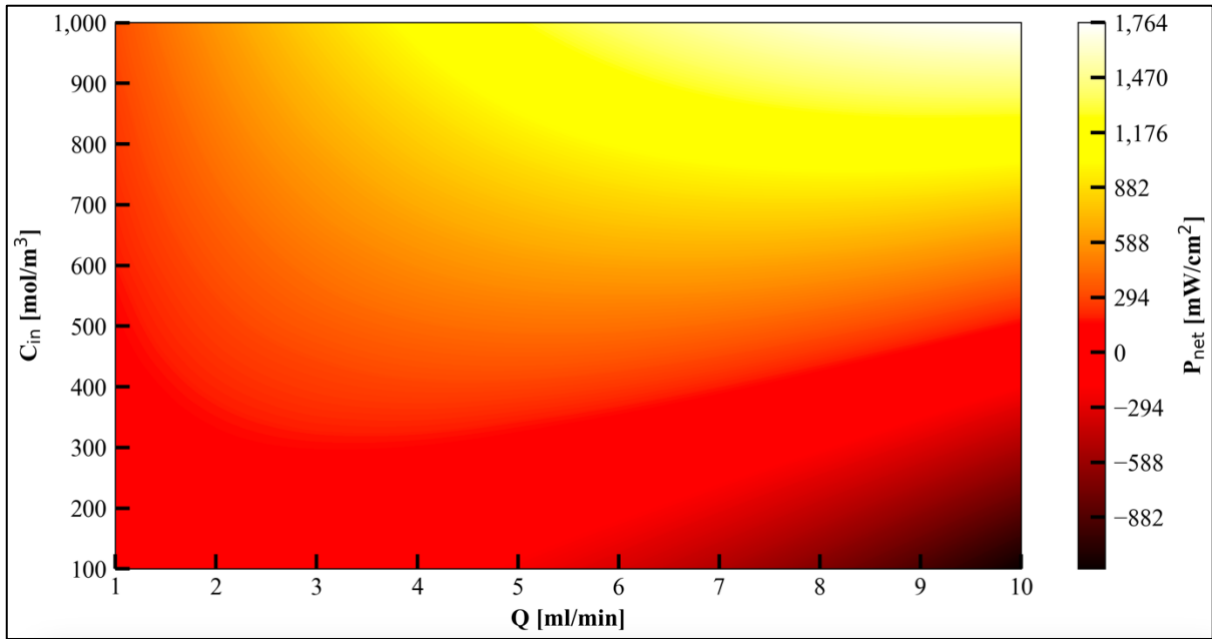
As discussed in previous sessions, it is important to make a balance between gross

and pumping power density to maximize overall net power density of a redox flow cell, which is calculated using the equation below.

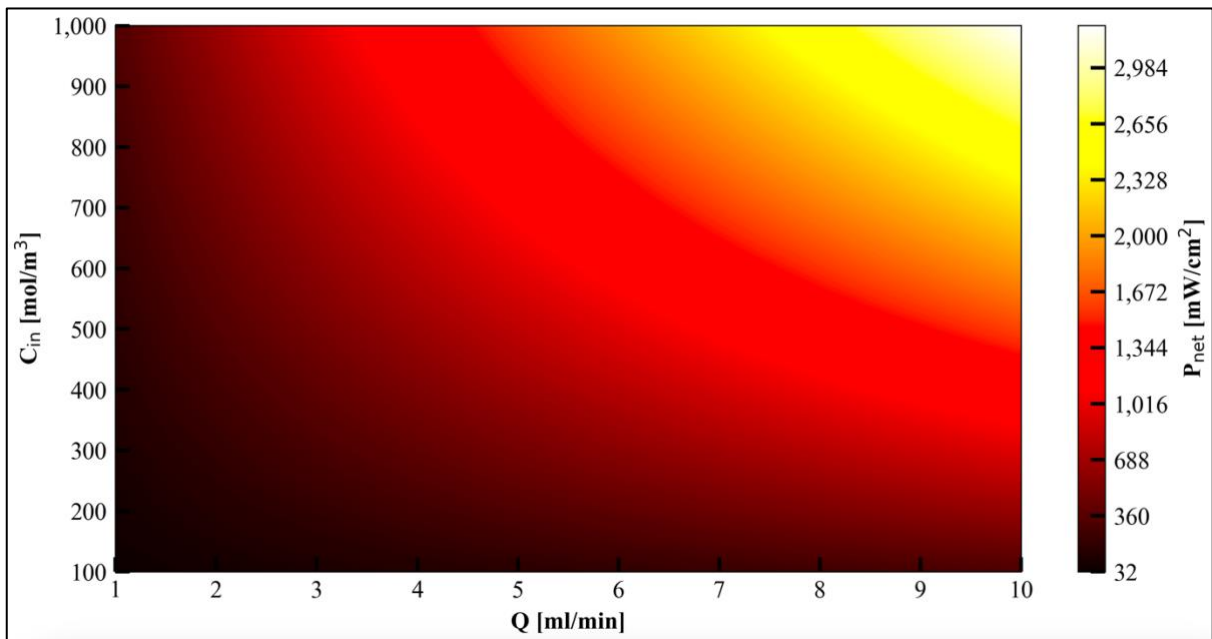
$$p_{net} = P_{gross} - P_{pump} \quad \mathbf{2-14}$$

where  $P_{net}$  is the overall net power density provided,  $P_{gross}$  is the maximum gross power density that could be read out from polarization curve, and  $P_{pump}$  is the pumping power required per unit area of electrode for cell operation. For instance, Figure 2-14 shows the result of net power density obtained from a vanadium redox flow battery in two different modes: without flow field (direct injection of the electrolyte through the cross-sectional area of electrode) and interdigitated flow field. The interdigitated flow field containing 5 inlet and 5 outlet channel paths with 1 mm width of ribs was considered. The following conditions were assumed for analysis.

- Electrode size: 2.5 cm × 2.5 cm (6.25 cm<sup>2</sup>)
- Permeability of electrode: 1 × 10<sup>-13</sup> m<sup>2</sup>
- Viscosity of electrolyte: 0.05 Pa.s
- Number of inlet channel: 5
- Number of outlet channel: 5
- Perfect polarization behavior ( $V_{cell}=1.26V$ )
- Flow of electrolyte at in-plane direction only
- All the reactant introduced in an electrode is consumed by reaction



a)



b)

**Figure 2-14 – Change of net power density in terms of inlet concentration of reactant and flow rate of electrolyte with a) flow-through mode (without flow field) and b) interdigitated flow field**

It can be confirmed from Figure 2-14 that the redox flow cell without a flow field tends to provide negative net power density at low inlet concentration of reactant or high flow rate of

electrolyte because of relatively high pumping power required with longer travel length of electrolyte compared to the gross power density produced. On the other hand, the cell with an interdigitated flow field tends to approach much higher net power density due to negligible pumping power requirement with shorter travel length, which shows the significant advantage of flow field application. In practice, the structure of fibrous electrodes acts as similar role. The higher surface area of fiber (active site) and the advanced fibrous structure inducing uniform ion distribution increase the gross power density. Simultaneously, the pumping power can be reduced with low permeability of electrodes. However, the permeability of electrodes and surface area of fiber are in general inversely correlated. The key challenge of this thesis is to make a balance among those electrode properties to maximize the net power density. In order to approach this goal, this thesis explores a way of constructing novel electrospun fibrous structures in electrodes. Specifically, projects focus on designing innovative fibrous layers, which induce uniform ion distribution over the whole region of the electrode to approach high gross power density while maintaining a high permeability to minimize the pumping power required for operation. The structure of the fibrous electrode was modified in terms of fiber size, fiber arrangement, and porosity. The fiber size was controlled with a novel manufacturing method, electrospinning. Porosity was altered by applying compression during the carbonization process. Lastly, the fibers were arranged into novel multi-layered structures by stacking different layers to induce uniform ion distribution. Furthermore, a model was developed using multi-physics simulation to predict the performance of redox flow cells in terms of the properties of fibrous electrodes.

In practice, the power density of a vanadium redox flow battery has been reported in previous reports. It has been originally reported that a vanadium redox flow battery reaches  $100 \text{ mW}/\text{cm}^2$  with a typical current density of  $80\text{-}100 \text{ mA}/\text{cm}^2$  [86]. Kumar et al [135] could

improve the power density with a higher flow rate of electrolyte and the application of flow fields, but it was still lower than  $0.2 \text{ W/cm}^2$ . On the other hand, Charvat et al [87] could approach up to  $1.1 \text{ W/cm}^2$  with optimized compression and thermal activation of electrodes. Jiang et al [88] could even reach the higher power density of  $2.78 \text{ W/cm}^2$  with a novel way of carbonizing graphite-based electrodes. In fact, the huge difference in power density among each reference was attributed to various operating conditions and designs of redox flow cells, such as cell size, electrode materials, electrode treatment, electrode thickness, electrolyte components, electrolyte flow rate, flow field design, membrane types, materials of current collectors, etc, which obscures direct comparison. In other words, it is quite difficult to confirm the improvement quantitatively. To avoid this complexity, the performance of novel electrodes introduced in this thesis was evaluated qualitatively by comparing them with cases of reference fibrous electrodes. For all experimental runs, identical redox flow cell hardware was used, which contains the same sizes and materials for each compartment with same operating conditions. The two samples, SGL25AA and SGL39AA, were considered as reference electrodes. They are the fibrous materials commonly used as gas diffusion layers (GDL) in Polymer Electrolyte Membrane Fuel Cells (PEMFC).

### **3. Improvement of Vanadium Redox Flow Battery Performance Obtained by Compression and Laser Perforation of Electrospun Electrodes**

#### **3.1. Introduction**

Engineered porous materials are utilized in numerous applications, such as membrane filtration, oil extraction, electrochemical devices, and so on [89,90,91,92,93]. The performance of the porous material in each application is dependent on its structural properties, motivating the need to carefully design the porous structure. Carbonized fibrous materials are widely used as electrodes in various types of batteries because of their high specific surface area for reaction, high porosity to support flow and diffusion, and good electrical conductivity through the interconnected fibers.

Fibrous felts or mats are commonly used in redox flow batteries, which are one of the most promising secondary batteries for energy storage system (ESS) due to the adjustable capacity of the storage tanks filled with electrolyte solution, and various redox couples have been tested exhaustively for use, such as V/V, Zn/Br, Zn/Ce, V/Br, and V/Fe [94,95,96,97,98,99,100], as discussed in Chapter 1. Among them, the vanadium redox flow battery has been preferred because of its safety and high efficiency. The anolyte and catholyte contain compatible active species, vanadium ions, and thus the undesirable side-reactions are significantly diminished compared to other redox couples [101]. In practice, the flaw of vanadium redox flow battery is the high capital cost attributed to the pricy vanadium. US Department of Energy (DOE) targeted the capital cost at 100-150 \$ kWh<sup>-1</sup> (86-129 €

kWh<sup>-1</sup>) for ESS commercialization, while the several economic analyses present the cost of 300-1500 € kWh<sup>-1</sup>. However, recently, the way of electrochemical rebalancing for vanadium redox flow batteries has been suggested, which provides economic benefit [102]. In general, almost 90% of the global carbon fiber production is polyacrylonitrile (PAN) based [63,103,104,105,106,107,108]. PAN is a popular polymer pre-cursor when making carbon fibers due to the high carbon yield and good properties of the resultant carbon such as high electrical conductivity, chemical and electrochemical stability, acid resistance, and active surface area. The electrode in a vanadium redox flow battery is typically a fibrous mat structure of carbonized fibers with a high specific surface area of active sites capable of high current densities. Production of carbon-fiber layers has been discussed at length in various articles [52,53,109]. The recent studies focused on modifying the properties of commercial carbon-fiber with materials, such as perovskite, SO<sub>3</sub>H - functionalization, and porous nanocomposite with ZrO<sub>2</sub>, to enhance the electrochemical activity [110,111,112]. However, commercially available fibrous carbon mats are mass produced with a fiber diameter of 10 μm for multiple applications, which is quite large to provide high enough surface area of active site. In the case of the vanadium redox flow battery, smaller fiber diameters are preferential due to the exponential increase of surface area owing to smaller diameters. As introduced in session 2.4, one option to produce a fibrous mat with smaller fiber diameter is to use electrospinning. This approach is convenient for laboratory studies and has the potential for scale-up to large volume production [113,114,115]. Liu et al [24] explored the possibility of using electrospinning to fabricate fibrous electrodes with fiber diameters less than 1 μm which showed markedly improved performance, especially within the kinetic activation region.

One common characteristic of electrospun mats is their high porosity, usually

exceeding 90%, which enhances fluid transport. However, it is also desirable to have a lower porosity to achieve a higher volumetric surface area. Also, small pores among the fibers reduce the permeability, constraining the electrolyte transportation or increasing parasitic pumping costs [61,66,116]. Therefore, a path forward is to develop a way of arranging fibers so that sufficient permeability can be retained while maintaining the small fiber size. These competing objectives have proven to be difficult to simultaneously satisfy. For instance, as introduced in session 2.9, Yadav et al. [85] showed that using ribbons could increase the surface area compared to standard electrospun materials, but this hurt the through-plane transport of ions and limited the performance of the battery at higher current density. The present work addresses this impasse by employing a technique whereby the porosity of the mat is decreased by compressing it during the stabilization step, which is a much simpler way to increase the specific surface area than the ribbon approach of Yadav et al., and this was followed by laser perforation to enhance the through-plane transport. The structural and transport properties of the resultant material are quantified extensively, showing an impressive boost in all transport metrics that are pertinent to flow battery operation. These materials are also tested in flow battery operation and shown to provide substantial performance improvements over the entire range of current density.

## **3.2. Experimental Methods**

### **3.2.1. Electrospinning**

Fibrous samples were prepared using the electrospinning setup described by Kim et al [117], though with different conditions to ensure electrospinning rather than electrospraying. Polyacrylonitrile (PAN) (Scientific Polymer Product Inc, MW 150000) was dissolved into the N,N-dimethylformamide (DMF) (Sigma Aldrich, ACS reagent, 99.8%). The size of the fiber can

be controlled by adjusting the wt% of PAN resin in the mixture [24,118]. In this study, 12 wt% was used for all samples since this gave the thickest fiber that could be created without difficulties due to high viscosity of the spin dope. The mixture was prepared by combining the resin and solvent in a beaker, stirred for 20 hrs to ensure homogeneity, and then placed in a syringe. The target volume and the flow rate of the solution for each run were controlled using the syringe pump (New Era Pump Systems Inc, NE-1010). The flow rate was maintained at 0.5 mL/hr while the target volume was adjusted to obtain different initial thicknesses. The solution was ejected from the tip of a 16-gauge needle with the voltage provided by a negative-polarity power supply (Glassman High Voltage Inc, PS/MJ30N0400-11). A voltage of ~12 kV was applied on the needle to obtain the continuous filament. A flat plate was used as the collector, and it was grounded by a copper wire. A sample size of 120 mm by 120 mm was created for each run, and the needle was rastered across the target with a pitch size and spacing of 10 mm, at a speed of 15 mm/s was applied. The needle to collector distance was maintained as 8.5 cm.

### 3.2.2. Stabilization and Carbonization

The electrospun materials were stabilized and carbonized in a tube furnace (MTI Corporation, GSL-1700X-UL). Samples were cut from the master sheet to a size of 76.2 mm by 101.6 mm and clamped between two stainless steel plates separated by a pair of spacer shims with thicknesses known to be within 1  $\mu\text{m}$ . The samples were heated at a rate of 5  $^{\circ}\text{C}/\text{min}$  until the temperature reached 250  $^{\circ}\text{C}$  where it was stabilized for 3 hours. After stabilization, the furnace was allowed to cool back to room temperature, and the sample was removed from the stainless-steel plates and placed between two graphite plates without compression to keep them flat during carbonization, then put back into the furnace for

carbonization. Nitrogen gas was introduced into the furnace at a flow rate of  $\sim 200$  sccm and the temperature was continuously increased at a rate of  $5$  °C/min again. The temperature was held for 40 minutes at plateaus of  $850$  °C and  $1050$  °C.

### 3.2.3. In-Plane and Through-Plane Permeability

Both in-plane and through-plane permeability of the electrospun samples were measured. Permeability of each sample was measured based on Darcy's law, as described by Gostick et al. [66]. Nitrogen gas was used and thus was accounted for the compressibility of the fluid [32]. A rectangular sample size of  $12.7$  mm by  $50.8$  mm was considered for in-plane permeability measurement, whereas the circular shape with the diameter of  $22.2$  mm in the case of through-plane one. The flow rate of nitrogen gas ranged from  $10$  to  $100$  sccm was applied (Omega Engineering Inc, FMA-2617A). The inlet pressure was measured using a transducer appropriate to the anticipated pressure drop (Omega Engineering Inc, PX409-050DWU5V, PX409-005CG10V, PX409-10WDWU5V), while atmospheric pressure was assumed at the outlet boundary. The thickness of the sample was adjusted by the stainless-steel spacer shim for the in-plane measurement, while thickness was not controlled for the through-plane measurement (i.e., the samples were not compressed).

In addition to the standard linear setup, an alternative method of measuring the in-plane permeability was considered based on a radial flow configuration as described by Mukherjee et al. [119]. This method was considered here so that the permeability of the samples could be determined without any compression since the radial holder requires no gaskets or sealing. The sample was cut into the disk form with inner and outer radii of  $3.175$  mm and  $12.7$  mm. The nitrogen gas permeated radially from inner to outer radius, and Eq.S4 and S5 were considered to calculate the permeability.

#### 3.2.4. Porosity

The buoyancy method, which has been shown to be well suited for measuring the porosity of thin fibrous materials [120], was used to measure the porosity. The samples were cut into disks 22.2 mm in diameter, and their dry weight was measured. Each piece was then submerged into silicone oil (Sigma Aldrich Inc, 63148-62-9), having a density of 0.96 g/mL, and weight again while submerged to obtain the wet weight. To estimate the bulk volume of the sample, the sample thickness was manually measured using a micrometer (Mitutoyo, 293-348-30). The micrometer contained the thimble, which holds the measuring force lower than 5 N to prevent compression during the measurement. The thickness was measured for both uncarbonized and carbonized samples to confirm the material loss.

#### 3.2.5. Specific Surface Area

Although samples with higher porosity and permeability are advantageous for transport phenomena, this leads to relatively lower specific surface area. In this study, Brunauer-Emmett-Teller (BET) theory was applied to isotherm data obtained using dynamic vapor sorption (DVS) (Surface Measurements Systems Ltd, P29F00061) to extract the specific surface area. Cyclohexane (Sigma Aldrich, ACS reagent, 99%) was used as an adsorbate to ensure uniform wetting on the solid surface. The use of the DVS technique was necessary since the surface areas presented by the samples in this work are not high enough to be reliably registered by conventional pressure-based physisorption devices. A typical isotherm for an electrospun sample is shown in Figure S1.

### 3.2.6. Laser Perforation

The CO<sub>2</sub> laser cutting machine (LS-1416s BOSS Laser) was used to create the artificial hole on top of the electrospun fibrous electrode with the intention of enhancing through-plane transport. A piece of the fibrous sample was fixed with tape on top of the stainless-steel plate to ensure a flat surface and a well-focused laser beam. The perforations were made in a Cartesian grid-pattern. The raster speed of a laser head was set as 10 mm/s while the power was maintained at 15 W. The distance between the tip of the laser head and the sample was kept at 5mm. The holes were created at every consistent 1000 μm or 2000 μm intervals to approach a constant hole density of 100 or 200 holes per 1 cm<sup>2</sup>. In practice, due to the fixed size of a local lens installed on the machines, the applicable minimum size of hole was limited at 100 μm in diameter. The size was considered for all the sample in this study to minimize the loss of fiber surface caused by the perforation. The sample was perforated as manufactured through electrospinning technique, without any form of treatment.

### 3.2.7. Tomography

#### 3.2.7.1. *Sample Preparation and Image Acquisition*

Nano-scale X-ray computed tomography of the electrospun fibrous films was used to study and visualize the 3D structure of the electrospun fibrous films and was accomplished using a ZEISS Xradia 810 Ultra X-ray computed tomography microscope with a monochromatic X-ray beam energy of 5.4 keV. This technique is a powerful tool to provide insights into the internal structure of the various porous materials used as electrodes in electrochemical cells [121,122,123]. High-resolution (HRES) Zernike phase contrast mode (16 × 16 μm field of view) with a voxel size of 16 nm and a resolution of 50 nm was used to acquire 451 radiographs

while rotating the sample about a vertical axis from  $-90^\circ$  to  $+90^\circ$  with an exposure time of 600 s per 2D projection. Prior to acquiring a tomographic dataset, a set of reference radiographs were acquired which were later used to correct for the transmitted X-ray beam. Samples were fixed on a stainless-steel pin using epoxy adhesive and mounted on a pin-vise holder. Gold fiducial markers were placed on the region of interest with a micromanipulator and used for sample alignment. After tomographic acquisition further corrections for the marginal drifts of the 2D projections were affected using the ZEISS XRMController software and the fiducial marker. 3D reconstruction of the radiographs was performed using the ZEISS XMReconstructor software.

#### **3.2.7.2. *Image Processing***

Obtaining a binary image of solid and void from the greyscale images required some filtering to remove noise. A non-local means filter was used to remove noise while preserving edges between void and solid [124]. The results are shown in Figure S2. The reduction in the noise was sufficient to allow a global threshold to be applied. The experimentally obtained porosity of the samples was used as a guide to set the threshold value. For the uncompressed sample a threshold of 0.52 was applied giving a porosity of 0.88 compared to 0.89 obtained experimentally. For the compressed sample a threshold of 0.55 was used to obtain a porosity of 0.77 compared to the experimental value of 0.77. To ensure the threshold yielded a physically realistic image any floating solid voxels were also trimmed, though this only changed the porosity by 0.005 at most. It should also be noted that a sensitivity study was performed to confirm that changing the threshold level up or down by 0.05 only changed the observed transport properties by a few percent. This is explained in more detail in Section 3.3.1.2.

### 3.2.7.3. *Image Analysis*

Several quantitative image analysis tools were used to extract measurements and properties from the tomography images. The local thickness filter was applied to both void and solid phase to extract the pore and fiber size distributions. The local thickness filter used here was achieved by inserting spheres of a given size  $R$  into the image, then marking any voxels which were overlapped by a sphere with the value of  $R$  [125]. The size of  $R$  is decreased by 1 voxel and the process repeated, though any voxels which were already labelled with a previous value of  $R$  were not overwritten. The resulting image can subsequently be analyzed by counting the number of voxels labelled with each size to extract a volume weighted size distribution. This filter was applied to both the void and solid phase to get pore and fiber size distributions, respectively.

The electrical conductivity of the fibers and gas diffusivity of the voids was estimated using direct numerical solution of the Laplace equation using the voxels as the computational mesh. A simple first-order finite discretization was used for efficiency since the domains were large. For the solid phase, boundary conditions of  $1\text{ V}$  and  $0\text{ V}$  were assigned on opposite sides of the domain and a charge balance was applied to each voxel. The current flow into the domain was computed to get the total flux,  $i$ , then the effective conductivity of the domain was found from:

$$i = \frac{\sigma_{eff}}{L} \Delta V \quad 3-1$$

where  $L$  is the length of the domain in the dimension under study and  $\Delta V$  across the domain was always  $1\text{ V}$ . Electrical tortuosity,  $\tau^e$ , is defined as:

$$\tau^e = \frac{\phi}{\sigma_{eff}} \sigma_{bulk} \quad 3-2$$

where  $\sigma_{\text{eff}}$  is the observed conductivity of the sample,  $\sigma_{\text{bulk}}$  is the intrinsic conductivity of the carbon constituting the fibers, and  $\phi$  is the solid volume fraction (i.e., the fraction of the domain through which the conduction occurs). Note that a high solid volume fraction increases the effective conductivity, analogous to a high porosity increasing the effective diffusivity as described by Eq.3-2.

Analogously, the void phase diffusion was computed by applying boundary conditions of 1 mol/L and 0 mol/L on opposing faces, and the effective diffusivity was found from:

$$n = \frac{D_{\text{eff}}}{L} \Delta C \quad 3-3$$

where  $n$  is molar flux,  $D_{\text{eff}}$  is the effective diffusivity, and  $\Delta C$  is the concentration difference.

The effective diffusivity was then converted to tortuosity values,  $\tau$ , using:

$$\frac{D_{\text{eff}}}{D_{\text{AB}}} = \frac{\varepsilon}{\tau} \quad 3-4$$

where  $\varepsilon$  is the porosity, and  $D_{\text{AB}}$  is the standard diffusivity caused by the concentration gradient. In both cases, any non-percolating solid / blind pores were removed from the image prior to performing the simulation as these would lead to singular matrices. The number of voxels removed was always very small and had a negligible impact on the porosity.

### 3.2.8. Flow Cell Validation

The electrochemical performance tests were implemented at 25 °C using a commercial single flow cell supplied by Fuel Cell Technology Inc for the electrolyte preparation as well as the polarization analysis. An interdigitated flow channel flow field was used since it was determined as the design providing the highest cell performance in previous studies [70]. The flow field was composed of 3.18 mm thick impregnated graphite with 7 inlets and 7 outlets having 1 mm wide and 1mm deep for each channel as well as 1 mm width of ribs. The

size of the active area of the flow cell was as  $5 \text{ cm}^2$ . Each electrode sample was cut into the size of  $2.23 \times 2.23 \text{ cm}$  and sealed within an opening in the PTFE sealing gasket. The gasket was compressed in 85-90% of the thickness of uncompressed electrode so that the sample can be compressed by 10-15%. Nafion 117 (Nafion Store, Ion Power Inc) was submerged into DI water for 24 hours to be used as a membrane [126]. Furthermore, the nitrogen gas was introduced into the system 30 minutes before and during the experiments to prevent the capacity fade in the presence of oxygen. The flowrate of the electrolyte was controlled by the peristaltic pump (MasterFlex) with an Easy-Load II pump drive (Cole-Parmer). The flowrate of electrolyte was consistently maintained as 10 mL/min. The potentiostat (BioLogic VSP with booster VMP3B-20) was used to charge or discharge the cell.

Vanadyl sulfate ( $\text{VO}\text{SO}_4$ ) (NOAH Technologies, 99.5% purity) and sulfuric acid (Sigma Aldrich, 95.0-98.0%) were used without any additional treatment to make all the electrolytes used in this study. The electrolyte was prepared through the electrolysis, as mentioned in the previous literature [127]. The deionized water ( $>18.2 \text{ M}\Omega \text{ cm}$ ) was used to dilute the solution to the desired rate. For the cell performance test, 40 ml of solution containing 1.6 M  $\text{VO}\text{SO}_4$  and 3 M  $\text{H}_2\text{SO}_4$  mixture was poured into the catholyte reservoir while 20 ml of the same solution was at the anolyte side. The electrolyte was prepared by charging at a constant current density of  $20 \text{ mA cm}^{-2}$  with 1.65 V cut off voltage. Then, it was continued by switching to apply constant voltage of 1.65 V until the current density decreased down to a very low value ( $0.1 \text{ mA/cm}^2$ ), indicating nearly 100% state of charge (SOC) to oxidize the  $\text{V}^{4+}$  to  $\text{V}^{5+}$  in the catholyte while reducing the  $\text{V}^{4+}$  to  $\text{V}^{2+}$  in the anolyte. After that, 20 ml of  $\text{V}^{4+}/\text{V}^{5+}$  electrolyte at the catholyte was removed from the reservoir to balance the electrolyte capacity.

The cell performance was evaluated based on the galvanostatic polarization. After the

electrolyte preparation through the electrolysis, the cell was discharged to 0.6 V at 100 mA/cm<sup>2</sup> and charged back at the identical current density for half of the previous discharge time to reach 50% state-of charge (SOC). The galvanostatic polarization was performed with a 30 second hold per step so that a steady state potential can be attained. The cell was recharged back to 50% SOC at the same current density between each discharging step to retain polarization accuracy.

### **3.3. Results and Discussion**

#### **3.3.1. Impact of Compression During Stabilization**

##### **3.3.1.1. *Structural Changes***

The basic structure of each sample was observed using SEM and the resulting images are shown in Figure 3-1. Images (a) and (c) show the sample prior to compression whereas images (b) and (d) show the carbonized sample after compression. Comparing the images of the pristine samples to the images of the compressed samples it is clear that the fibers were compacted into each other by the compression during stabilization. This compaction of the fibers results in a reduced porosity as will be confirmed quantitatively below. The fiber diameter of pristine and compressed samples was estimated to be identical based on the SEM images. More exact size distributions of the samples will be explored below using image processing tools on X-ray tomography images.

Compression during the stabilization step was beneficial because the fibers were still quite pliable. According to Newcombe et al [63], the structure of PAN molecule changes depending on the temperature during the stabilization and carbonization steps. Prior to and during the stabilization step, the uncarbonized polyacrylonitrile (PAN) is in the form of flexible linear chains, enabling the fibers to be compacted into each other by the force of the steel

plates. After stabilization was complete the molecules were converted from linear chains to stable rings, leading to the thermally stable and stiffened fibers so they maintain their shape after the stainless-steel plates are removed. Upon putting the stabilized sample back into the furnace for high temperature carbonization, the compressed shape persisted which was crucial since the high temperatures would be problematic for the metal plates. The samples were placed between thin graphite plates during the carbonization step to prevent them from curling, but these were quite light so did not contribute to compression.

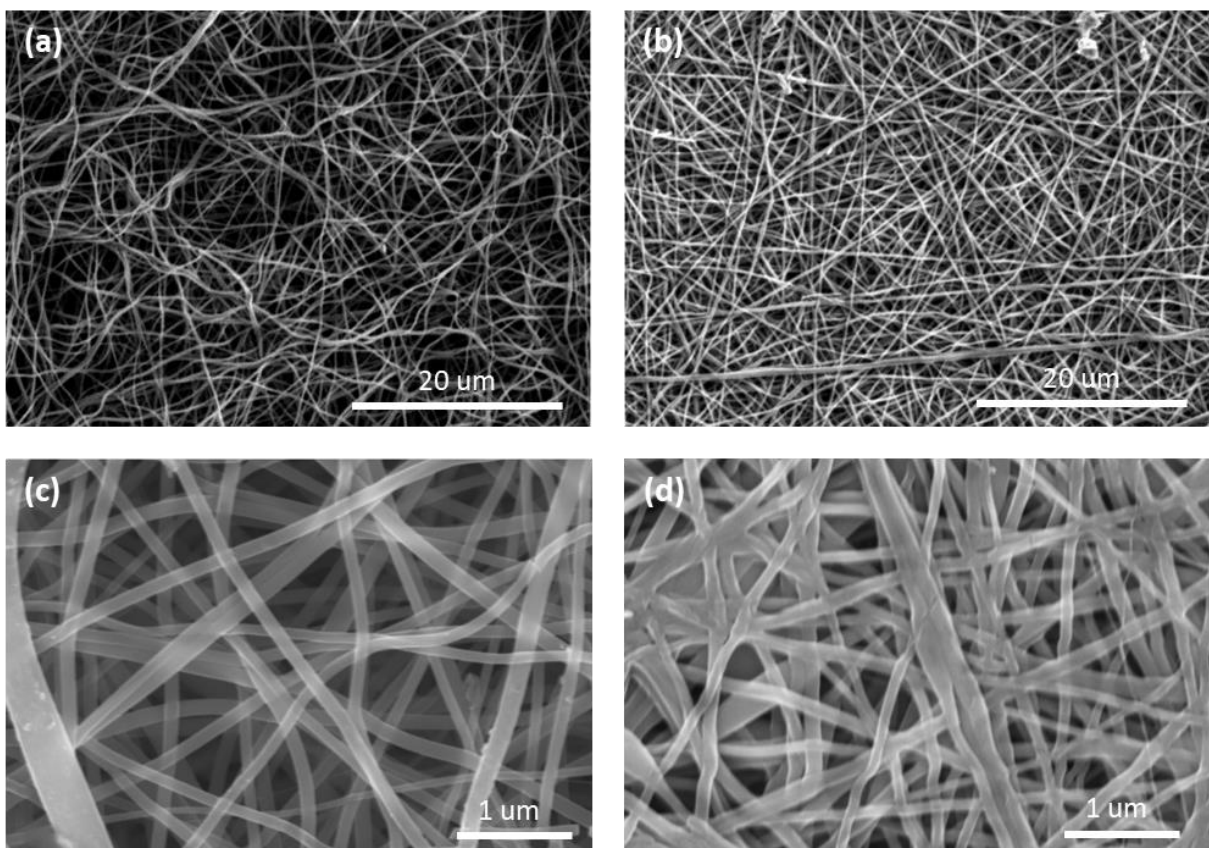


***Figure 3-1– SEM images of pristine (a and c) and compressed (b and d) carbonized samples at low and high magnification***

#### *Thickness and Porosity*

The thickness of each sample was measured at four different points at the edges to confirm the possibility of variation. The thickness was impacted by both stabilization and

carbonization. The uncarbonized fibrous sample, electrospun with 10 ml of 12 wt% PAN solution, had a thickness of around 450  $\mu\text{m}$  but shrunk to a thickness ranging from 330  $\mu\text{m}$  to 350  $\mu\text{m}$  after the stabilization and carbonization process. In the case of the compressed sample, the thickness was measured as 170  $\mu\text{m}$  after carbonization although 178  $\mu\text{m}$  spacer shim was used during the stabilization process, indicating some slight additional shrinkage during carbonization. According to Choi et al [128], the stabilized PAN fiber contains oxygen bonded to carbon. During the carbonization at temperatures of 1050°C, oxygen and the heterocyclic nitrogen atoms are split off from the stabilized PAN molecule, leading to the further reduction of the sample thickness. For this reason, a spacer shim slightly thicker than the desired sample thickness is suggested.

The porosity of SGL25AA ( $\varepsilon = 0.88$ ) and pristine sample ( $\varepsilon = 0.89$ ) were quite similar despite much different fiber sizes. This means that the electrospun sample contained a greater surface area of active site while maintaining almost the identical void volume for electrolyte flow. However, much smaller voids were created among the sub-micron sized fibers in the electrospun sample, leading to lower permeability. In other words, it is a challenge to compromise between high surface area and high permeability. The pore size distribution of each sample will be discussed more in detail in the next section. On the other hand, the compressed electrospun sample had much lower porosity ( $\varepsilon = 0.78$ ) than the uncompressed one ( $\varepsilon = 0.89$ ), as depicted in Figure 3-2a).

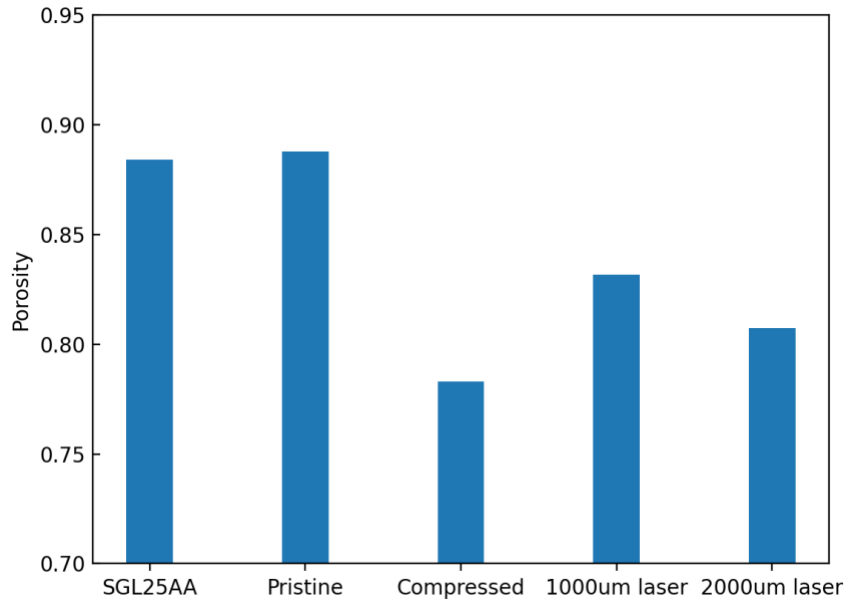
#### *Pore and Fiber Size Distributions*

X-ray computed tomography images were obtained for the carbonized samples with and without compression being applied during the stabilization step. Volumetric renderings of both samples are shown in Figure 3-2b).

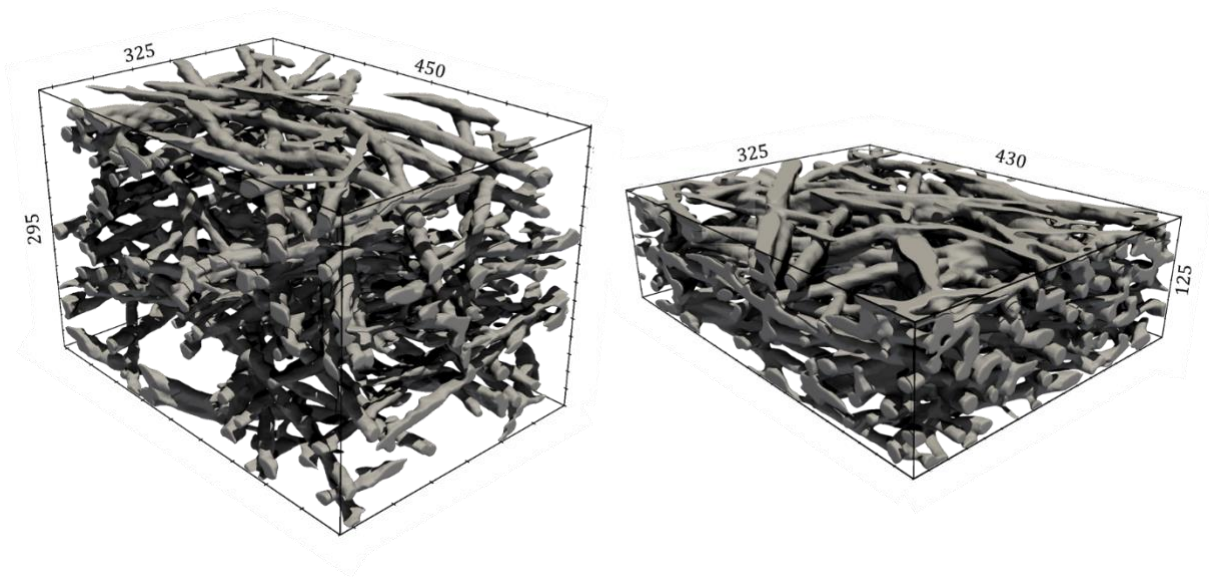
Due to the field of view vs resolution trade-off, these images do not capture the full thickness of the samples. The resolution was 16 nm per voxel, which allowed for at least 10 voxels across the fiber diameter to ensure the solid phase was represented accurately. This high magnification, however, means that the images obtained were only 4 – 5  $\mu\text{m}$  along each edge, much smaller than the total thicknesses (listed in Table 3-2). It was therefore necessary to assume that the subdomains imaged were representative of the whole. The different thickness of the two images was due to imaging conditions and not related to the different overall thickness of each sample.

By visual inspection it is apparent that the compressed sample has a higher fiber density. Figure 3-3a) shows the pore size distribution of each sample as determined by the local thickness filter. The pore sizes in the compressed sample are about half that of the uncompressed, which shows a consistent reduction with 50% sample thickness. The distribution is also tighter, while the uncompressed sample shows a bimodal behavior with some excessively large pores in the 600 – 800 nm range. Presumably the large voids are preferentially sacrificed during the compression step.

Figure 3-3b) shows the fiber size distribution analyzed in the same manner as the pore sizes. The size distributions are very similar, which is to be expected given they were produced from the same starting material and exposed to the same thermal treatment. A key feature of the fiber morphology that is not represented by the size distribution is the increased inter-fiber contact area caused by compression. Attempts to quantify this by analyzing skeleton branch points were not conclusive, however solid phase conductivity was computed, as discussed below, and showed a notable improvement in conductivity in the compressed sample.



a)



b)

**Figure 3-2 – a) Porosities of samples with different pre- and post-processing conditions applied, and b) volumetric renderings of the segmented images with the uncompressed sample on the left, and compressed sample on the right. Axis values indicate voxels, which were 16 nm in length.**

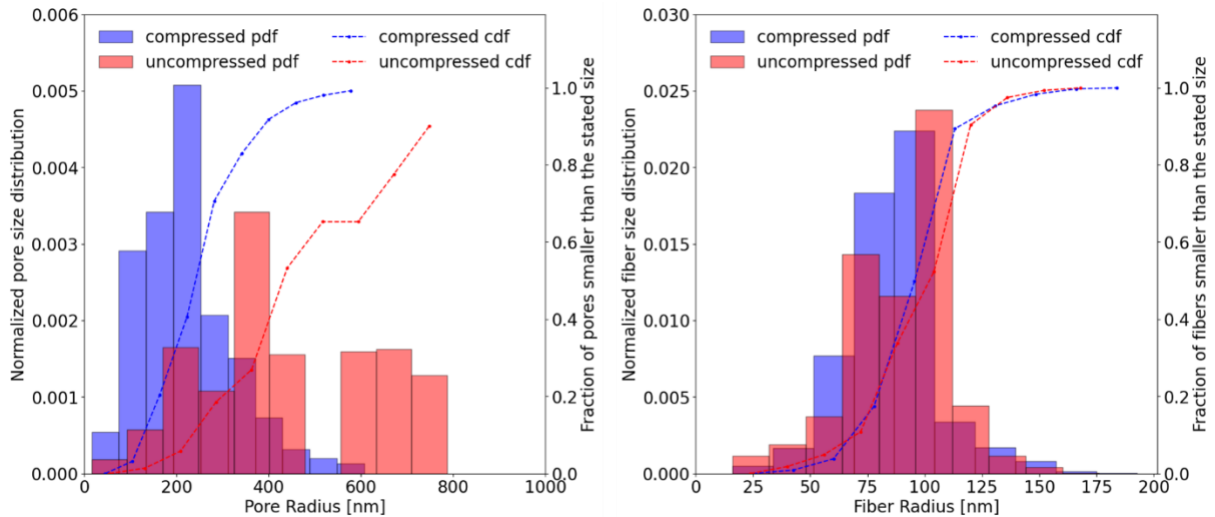


**Figure 3-3 – a) Pore size distributions for compressed and uncompressed samples, and b) Fiber size distributions for pristine and compressed samples**

#### *Specific Surface Area*

The specific surface areas of each fibrous sample per unit of mass and volume were measured using the BET method with cyclohexane as the adsorbing species, and the results are displayed in Table 3-1. The specific surface area of the pristine electrospun sample was compared to a commercially available SGL25AA sample with significantly larger average fiber diameter of approximately 7  $\mu\text{m}$ . The resulting gravimetric and volumetric surface areas of the pristine sample were over 7 times greater than that of the commercially available sample proving the great advantage of the nano-sized electrospun fibers. Also, as was expected, the sintered sample showed a 10% decrease in the gravimetric specific surface area likely caused by the increased interconnected area among fibers. As for the volumetric surface area, the compressed sample was actually increased by 1.82 times compared to the pristine sample. This increase is not at all caused by an increase in the total surface area but rather a decrease in the sample volume that resulted from compression. Therefore, the compression during stabilization yielded a thinner sample but with a small decrease of about 10% of total area.

**Table 3-1 - Specific surface area of electrospun fibrous samples**

<b>Sample</b>	<b>SSA (<math>m^2/g</math>)</b>	<b>SSA (<math>m^2/m^3</math>)</b>
<b>GDL25AA</b>	1.29	$2.71 \times 10^5$
<b>Pristine</b>	9.14	$2.00 \times 10^6$
<b>Compressed</b>	7.66	$3.35 \times 10^6$
<b>Compressed/laser (1000 <math>\mu m</math>)</b>	7.68	$3.14 \times 10^6$
<b>Compressed/laser (2000 <math>\mu m</math>)</b>	7.66	$3.24 \times 10^6$

- ❖ SSA: Specific surface area
- ❖ Compressed/laser (x): Compressed and laser perforated sample with x distance between holes

### **3.3.1.2. Effect on Transport Properties**

#### *Gas diffusivity*

The in-plane gas tortuosity of each sample was simulated using direct numerical simulation. The results were converted to tortuosity and are reported in Table 3-2, both samples have quite low tortuosity, with the compressed sample being somewhat higher due to its lower porosity. This data, though limited, follows the Bruggeman correlation with an exponent of 1.0, which is actually the expected value for diffusion through a bed of cylinders:

$$\tau = \varepsilon^{-1.0} \quad \text{3-5}$$

An interesting feature of these data is that the tortuosity values show very little anisotropy. This is especially true for the compressed sample where the in-plane and through-plane values are identical. This is probably due to the relatively high porosity and small domain size, meaning that the diffusion gas has minimal interaction with the solid structure. However, this low level of diffusional anisotropy was also observed by Jervis et al [129], so this behavior may

be common. As a point of comparison, the gas diffusion layer used in fuel cells has a tortuosity in the through-plane direction that is approximately twice that in the in-plane direction. Those materials are generally made from rigid linear fibers which might encourage anisotropy compared to the more flexible and pliant fibers produced during electrospinning. As will be discussed below, flow in the through-plane direction was quite hindered, which is attributed to compaction of the fibers on the surfaces of the samples, although neither of the tomograms contained the surface regions.

**Table 3-2 - Transport and physical properties of pristine and sintered samples**

Property	Pristine sample	Compressed
$\epsilon$ [ $cm^3/cm^3$ ]	0.89	0.77
$\delta$ [ $\mu m$ ]	330	170
$K_{TP}$ [ $m^2$ ]	$2.83 \times 10^{-14}$	$1.37 \times 10^{-14}$
$\tau_{IP}^g$	1.09	1.32
$\tau_{TP}^g$	1.15	1.32
$\tau_x^e$	3.14	2.65
$\tau_y^e$	3.31	2.02
$\tau_z^e$	245.56 <sup>a</sup>	7.00

❖  $\delta$ : Sample thickness

❖  $K_{TP}$ : Through-plane permeability

❖  $\tau_{IP}^g, \tau_{TP}^g$ : Tortuosity of void phase at in-plane and through-plane direction

❖  $\tau_x^e, \tau_y^e, \tau_z^e$ : Tortuosity of solid phase at x, y, and z direction

The value of  $\tau_z^e$  for the pristine sample is anomalously high to the presence of an air gap in the middle of the imaged domain

### *Permeability*

Permeability values were experimentally obtained for the uncompressed, compressed, and compressed sample with laser perforated holes. These were all compared with the commercially available SGL25AA. In Figure 3-4, the points shown as a circle shape indicate the permeability measured with the method introduced by Gostick et al, which applies a different degree of compression to samples at each step [66]. On the other hand, points with a cross symbol present the value measured radially using the method from Mukherjee et al without any compression [119]. As can be confirmed in the figure, SGL25AA had higher in-plane permeability compared to other electrospun materials due to its larger pores, or equivalently its large micron-sized fibers as described by Eq.S1.

There was no significant difference in in-plane permeability between uncompressed and compressed samples, despite the relationship between the porosity and permeability described in Eq.S1. This phenomenon reveals the crucial impact of the transformed fiber shape on the in-plane permeability. The fibers in the compressed sample presented lower resistance to the flow at in-plane direction, which can only be attributed to some change in the morphology since the fiber sizes remain constant. The evidence for this morphology change is also seen in the large drop in the solid phase tortuosity. Also, shown in Figure 3-4 is the Carman-Kozeny model given by Eq.S1. The  $k_{CK}$  constant in the denominator was determined for each sample by trial and error. The commercial SGL25AA and the pristine electrospun sample distinctly followed the trend of Carman Kozeny theory while the compressed sample deviated from the line at low porosity, as indicated by the symbol 'x' in Figure 3-4. The holder used to apply compression was quite thick stainless steel, but apparently still not strong enough affect the desired compression. In other words, these points are plotted at their expected porosity, but their actual porosity was higher, likely falling

on the Carman-Kozeny line.

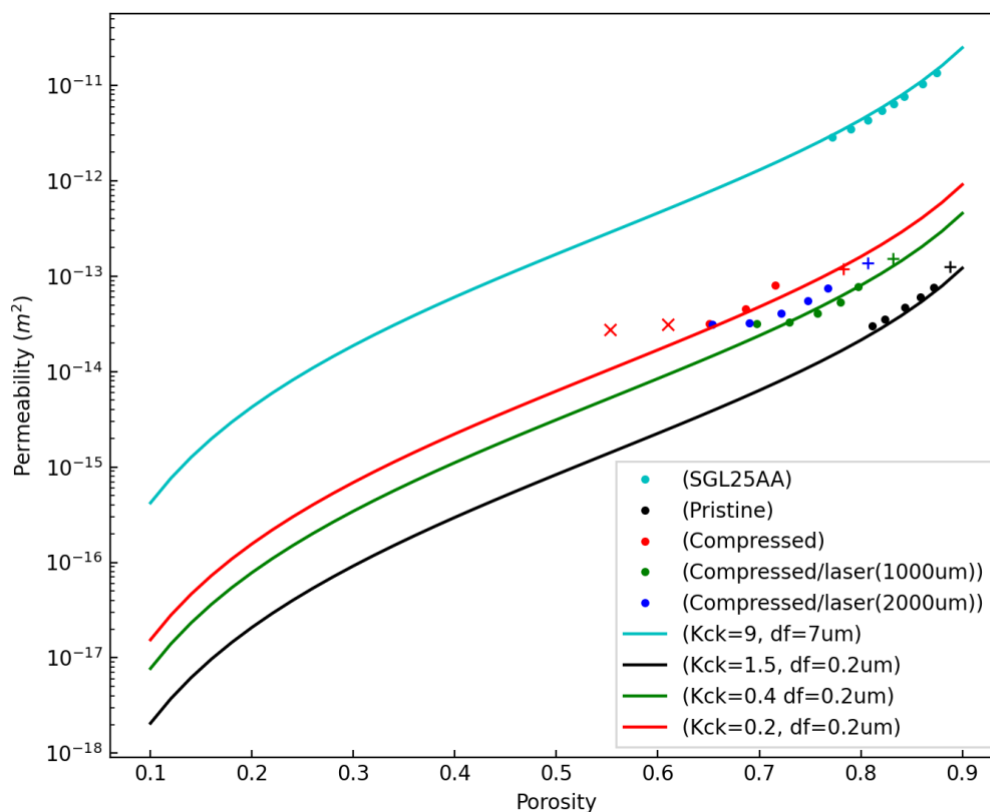


**Figure 3-4 - In-plane permeabilities at different degree of compression**

The through-plane permeability values showed a similar trend, with the SGL25AA having a much higher permeability coefficient ( $4.39 \times 10^{-12} \text{ m}^2$ ) than the electrospun samples owing to its larger fibers. The compressed sample and pristine electrospun has through-lane permeability coefficients about 100x lower than the commercial materials. Unlike the in-plane permeability, the compressed sample had a lower through-plane permeability ( $1.37 \times 10^{-14} \text{ m}^2$ ) than the uncompressed one ( $2.83 \times 10^{-14} \text{ m}^2$ ). The compression process resulted in a visibly densified or compacted layer of fibers on the surfaces, which present a thin barrier to fluid flow through the layer.

### *Electrical Conductivity*

A downside of high porosity electrodes is that the effective electrical conductivity of the solid structure drops. This is relevant to fibrous media where the conduction occurs within the fibers, and especially the through-plane direction since conduction in this direction requires fiber-to-fiber contacts. An expected benefit of the compression applied in this work was an increased number of contact points between fibers, and/or more intimate contact at each point. To analyze the impact of compression, conductivity simulations were performed on the volumetric images of solid phase using a simple finite-difference conduction solver. Conductivity was assessed in all three directions for both the compressed and uncompressed samples. The resultant voltage fields are shown in Figure 3-5, and the computed electrical tortuosity values are given in Table 3-2. The first result to note is the poor electrical conductivity of the uncompressed sample in the through-plane direction, which had a tortuosity of 246. This high value is obviously an anomaly and was found to be caused by the presence of just a single fiber connecting the top and bottom regions. This gives rise to a sharp change in the voltage gradient visible as the red and blue regions in the voltage fields in Figure 3-5 since all current flows through a single choke point, which dominates the resistance. This effect is an artifact of the small size of the imaged domain, but it is still noteworthy that contact points in the through-plane direction could be so sparsely distributed. Upon compression the conductivity in the z-direction is vastly improved with a tortuosity of  $\sim 7$ . In the in-plane directions the tortuosity before compression was  $\sim 3.2$  while after compression is dropped to an average of 2.3. Since the compressed sample had a higher solid volume fraction (0.23 vs 0.12) this reduction in tortuosity represents and even further improvements in the effective conductivity. For the same value of  $\sigma_{\text{bulk}}$ , the in-plane effective conductivity was increased by a factor of 3 on average. The through-plane effective conductivity of the

compressed sample is much higher (i.e., over 70 times higher), though this is an anomaly due to the artifact found in the present image. It was not possible to remove this artifact from the simulation since the gap between the top and bottom sections was angled in such a way that no rectangular domain could be extracted for study. If the trends observed for the compressed sample hold for the uncompressed one, then the TP tortuosity would be nearly 10, and the effective conductivity of the compressed sample is expected to have an effective conductivity 60% higher than the uncompressed one. It was also confirmed that the chosen threshold did not substantially alter the results. For instance using a threshold of 0.55 instead of 0.6 on the compressed sample yielded a tortuosity of 1.88 in the y-direction instead of 2.02, while a threshold of 0.65 yielded tortuosity of 2.37.

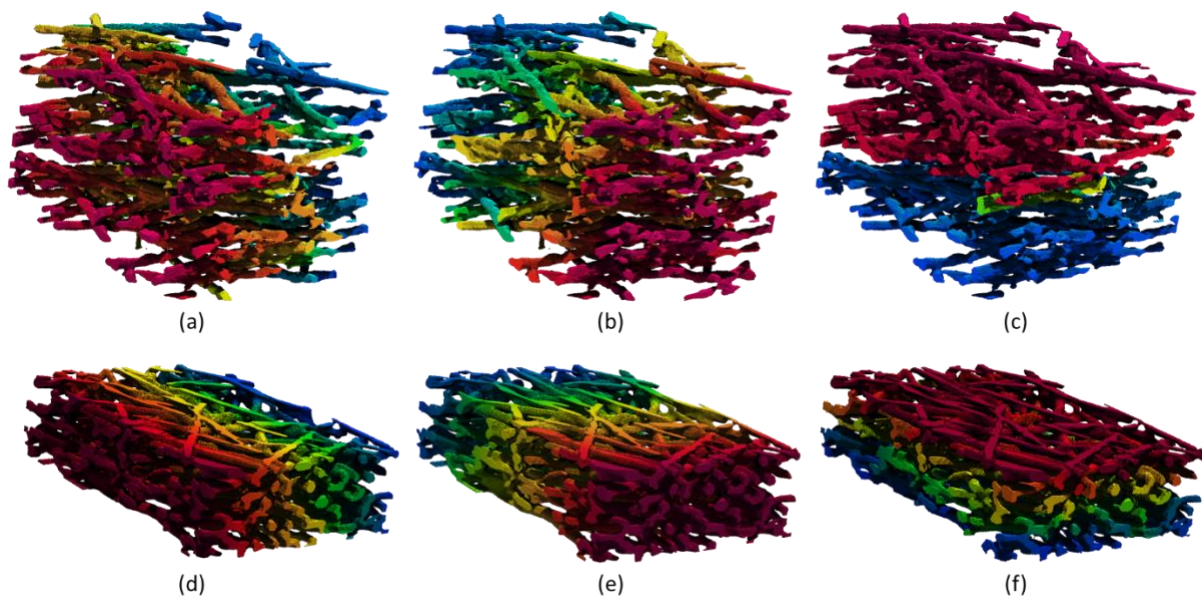


***Figure 3-5 – Voltage gradients obtained with direct numerical simulations of electron conduction in the solid phase. Top row: Uncompressed, bottom row: Compressed. Color represents the voltage gradient ranging from 1 (red) to 0 (blue)***

### 3.3.2. Impact of Laser Perforation

In practice, especially in the case of the battery with flow channels, such as proton

exchange membrane fuel cell (PEMFC) or redox flow battery, through-plane permeability is an important characteristic of the materials ability to induce uniform ion distribution. For instance, in the ribbon shaped fibrous material developed by Yadav et al. using a co-axial electrospinning technique [85], the high surface area of active sites in this material resulted in a very promising reduction of activation losses. However, the sample could not avoid serious mass transport losses despite having good in-plane permeability. The suspected reason was the low through-plane permeability, which hindered ion diffusion into the electrode.

In order to overcome the low through-plane permeability of the compressed fibrous electrode, holes with 100  $\mu\text{m}$  in diameter were created using a  $\text{CO}_2$  laser, as shown in Figure 3-6. The through-plane permeabilities of each sample were  $2.54 \times 10^{-11} \text{ m}^2$  (1000  $\mu\text{m}$  distance) and  $1.87 \times 10^{-11} \text{ m}^2$  (2000  $\mu\text{m}$  distance). As expected, more densely packed holes provided higher through-plane permeability and porosity due to the extra voids created, while the change of in-plane permeability is relatively stable since the holes were created in the through-plane direction. The volumetric specific surface area lost by the perforation was relatively little (-6.42% for 1000  $\mu\text{m}$  distance and -3.45% for 2000  $\mu\text{m}$  distance between holes) while the gravimetric surface area remained consistent regardless of the perforations since both the solid phase and fiber surfaces were lost by the  $\text{CO}_2$  laser simultaneously. In addition to that, despite the 16 % reduction of the fiber surface area per mass, both compressed and laser perforated sample showed improved volumetric surface (162.4% for 1000  $\mu\text{m}$  and 156.4% for 2000  $\mu\text{m}$  distance between holes) compared to the pristine one. Crucially the through-plane permeability was improved enormously in both laser perforated samples, validating the effectiveness of the laser perforation technique for enhancing through-plane transport. Overall, as illustrated in the previous section, permeability of fibrous material is in general inversely correlated to the specific surface area,

however, in the case of the compressed and laser perforated samples, both high specific surface area and permeability could be achieved simultaneously, demonstrating its outstanding physical properties.

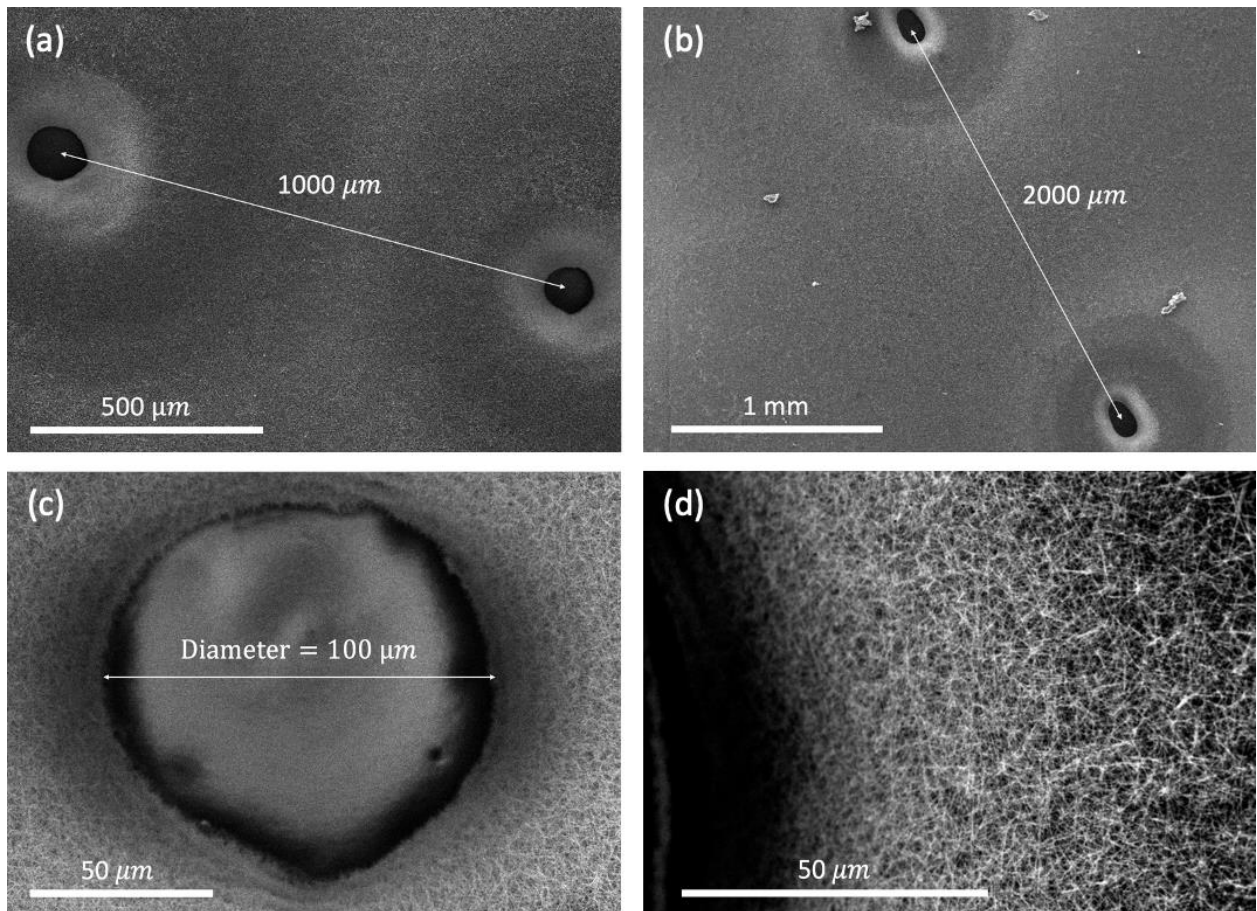


**Figure 3-6 – SEM images of laser perforated sintered sample (178  $\mu\text{m}$ ) with the distance of a) 1000  $\mu\text{m}$  and b) 2000  $\mu\text{m}$  between holes, laser perforated hole with the magnification of c) x1600 and d) x2700**

### 3.3.3. Cell Performance Assessment by Polarization Curves

The polarization behavior and the power density of a flow cell with each type of electrode is shown in Figure 3-7. In the case of the electrospun samples, the thickness was reduced to the half of pristine electrode via compression, as illustrated in session 3.3.1.1. Thus, two pieces of compressed samples were stacked at each side of the cathode and anode to match the thickness and superficial velocity. Overall, all electrospun electrodes provided

higher cell voltage over the entire range of current density compared to the commercial SGL25AA sample, which highlights the advantage of nano-size fiber produced via electrospinning. Although all samples were made of carbon without any catalyst, the electrospun samples contained more than 10 times higher specific surface area, which facilitated the reaction rate resulting in far less voltage loss in the activation region. When comparing between the various electrospun samples, the compressed electrode contained more concentrated fiber compared to the pristine, leading to a further increase of volumetric specific surface area and this is also shown by the lower activation loss observed in Figure 3-7. However, the performance of the compressed material drops below that other samples at higher current density, which can be attributed to the more densely packed fibers on the surfaces hindering the through-plane transport of vanadium ions. This through-plane transport limitation was also blamed for the weak performance of the ribbon electrodes of Yadav et al. In the present work it was considered whether this limitation could be overcome by creating artificial holes in the sample by laser perforation. For the polarization analysis, the distance among holes was maintained at 1000  $\mu\text{m}$ . The large artificial holes ( $d_f = 100 \mu\text{m}$ ) provide access to the relatively small pores between the electrospun nano fibers, as shown in Figure 3-6. It is believed that these holes provide two services to transport within the electrode. They allow flowing electrolyte to penetrate deeper into the electrode, thereby creating a more uniform distribution of reactant over the available surface areas. They also allow for ions to conduct from the membrane into the bulk of the electrode more readily, thereby lowering an ohmic losses. Detailed modeling of the complex interplay between these various transport processes is required to confirm these conjectures, and it would provide additional insight into the range of structural parameters that should be explored. Regardless, the observed performance increase is very notable however, with a 50% increase in power

density over a commercial electrode, and 17% increase of a normal electrospun fibrous mat.

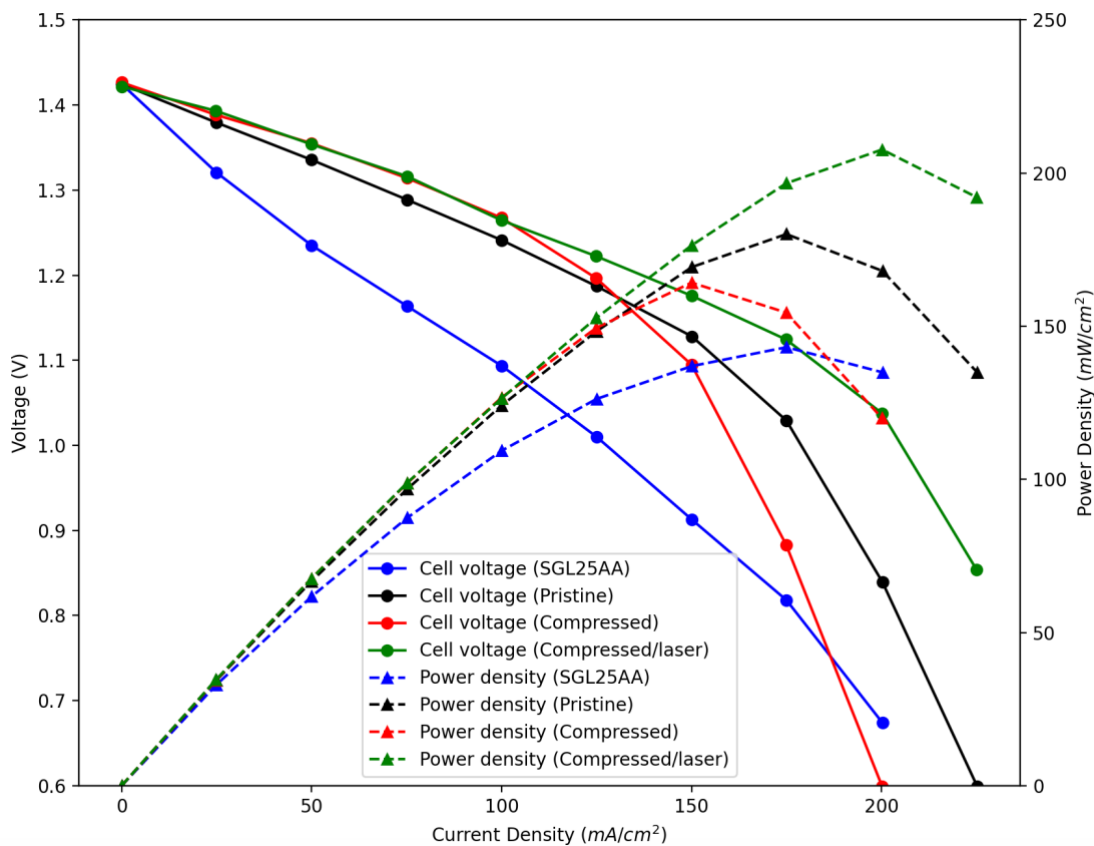


*Figure 3-7 - Polarization and power density curves at 50% state of charge*

### 3.4. Conclusion

This study presents a way of fabricating sintered electrospun fibrous materials by applying compression during the stabilization process thereby improving its physical properties in almost all categories. The specific surface area of the compressed electrospun samples were 50% higher than the pristine electrospun material. The sintered sample had higher in-plane permeability if compared at the same porosity, suggesting some beneficial morphological change in the structure occurred. The solid phase tortuosity was also lower by 40% in the in-plane direction and 70× in the through-plane direction. The gas phase tortuosity was slightly worse for the compressed sample, about 13% higher, but had a low

tortuosity overall so this property is not likely to be a rate limiting factor. The only property which was substantially worse in the compressed samples was the through-plane permeability, which was more than  $2\times$  lower. To remedy this problem, artificial holes were created by a laser perforator, which lead to vastly higher through-plane permeability with negligible loss in surface area. When tested in a running flow battery, the new electrode material, compressed electrospun mats with laser perforations, outperformed a commercial electrode over the entire range of current density, and the peak power density was 50% higher. This work illustrates that it is possible to break the surface area vs permeability trade-off, since in-plane absolute permeability was maintained while increasing surface area by more than  $2\times$ . Moreover, this work also showed that though-plane transport can be enhanced by simple laser perforations, overcoming through-plane transport problems that have been observed in fibrous mats previously.

### **Acknowledgements**

This works was supported by the Natural Science and Engineering Research Council (NSERC) of Canada

## 4. Multiphysics Simulation of Multi-layered Fibrous Electrodes for Vanadium Redox Flow Battery

### 4.1. Introduction

The principal sources of renewable energy, such as solar and wind, depend on weather conditions so heavy reliance on them leads to unstable electric grids. Energy storage systems (ESS) are a key technology to overcome this problem [7,8,130,131,132]. Renewable energy must be stored during periods of peak availability, so that they it be utilized flexibly without being interrupted by local weather [9]. Several types of batteries have been considered for the energy storage system, such as lead acid, lithium ion, sodium sulfate, and redox flow battery. Among them, the redox flow battery is one of the most promising due to the arbitrarily adjustable capacity of the electrolyte storage tanks [13,14,15,16]. Among various redox couples, the vanadium redox flow battery is considered as a promising next-generation battery because of its safety and high efficiency. However, redox flow batteries are not yet widely deployed owing to their relatively low energy and power density. In practice, while the lithium-ion battery, which has been widely used for electric devices, provides higher than  $150 \text{ Wh L}^{-1}$ , the energy density of vanadium redox flow battery is less than  $30 \text{ Wh L}^{-1}$  [133], which is limited by the solubility of the least soluble redox species. Additionally, the power density of vanadium redox flow battery is lower than desired (i.e.,  $\sim 0.2 \text{ W cm}^{-2}$ ) due to mass transport issues in electrode [134,135]. In order to overcome this latter issue, efforts have been focusing on enhancing the porous electrode structure. In general, commercially available porous carbon-papers used for redox flow batteries have a relatively low specific surface area due to their large fibers ( $\sim 10 \mu\text{m}$ ). Numerous efforts have attempted to employ

electrospinning to fabricate fibrous electrode with sub-micron sized fibers and observed a marked improvement in performance especially in the activation region where the additional surface area promoted higher reaction rates [24,89,129,136,137,138]. The downside of using smaller fibers is that it also reduces the permeability, increasing the required pressure to supply the same flow rate, although this is not usually discussed. Pumping costs are parasitic to the overall system efficiency, so they represent an important engineering problem and opportunity. Therefore, a path forward is to design the fibrous structure to increase permeability for ease of flow while maintaining the small fiber size to support high reaction rates.

In general, as discussed earlier in Section 2.8, there are two types of electrode configuration used in flow batteries: flow-through and flow-by [49,75]. The flow-by mode occurs when the flow channels are arranged in a serpentine or parallel arrangement. Flow-by operation relies on passive mass transfer into the porous electrode via diffusion, which has low mass transfer rates but has the benefit of low pressure drops since fluid is flowing in relatively large channels, and therefore lowering pumping costs. On the other hand, the flow-through design forces electrolyte into the pore space of the porous electrode by convective flow and thus provides outstanding mass transport rates [70]; however, it incurs higher pressure loss since the flow occurs through the small constrictions of the pores inside the electrode. In order to mitigate the high pressure-drop, an interdigitated flow channel configuration is usually used which provides much shorter flow paths [68]. However, this creates a secondary problem as “dead zones” form over the channels since the flow tends to bypass this region as it flows over the ribs [61]. This reduces the power density of the cell since substantial regions of the electrode are effectively inoperative. Increasing the realizable power density of the electrode, whether by reclaiming these dead-zones or other means, is

therefore a high priority objective. In this study, multi-physics simulations were used to study the polarization behavior of multi-layered fibrous electrodes in conjunction with interdigitated flow fields, to understand the tradeoffs between performance enhancement and pumping cost. The structural and transport properties of the various electrode layers were varied, and the simulations predict an impressive boost in flow battery efficiency, in terms of polarization losses. Although the present work used the all-vanadium system as a test case, the approach and general findings can be translated to other redox couples, including Zn/Br, Zn/Ce, V/Br, and V/Fe [18,23,94,95,96,97,98,99,100] since the impact of electrode structure is not strongly related to electrolyte components.

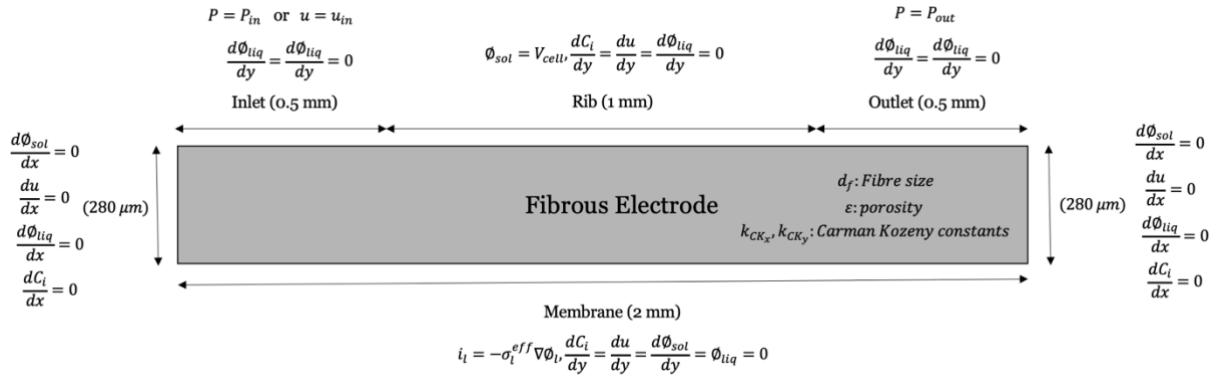
## **4.2. Modeling Approach**

### **4.2.1. Geometry**

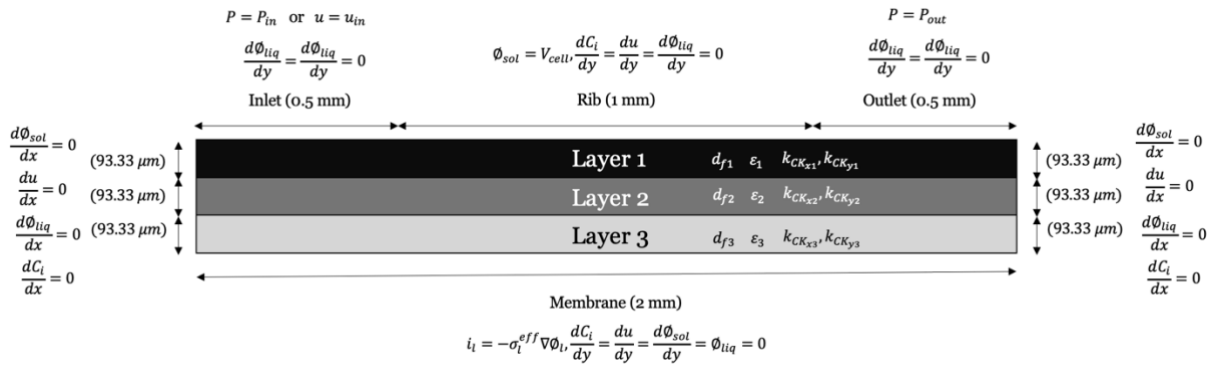
The scope of this study was limited to the cathode of a vanadium redox flow cell during discharge so that the impacts of specific interventions could be more conclusively analyzed. The experimental performance data from Messaggi et al [139] was used for validation, since this is one of the few published studies available in the literature using a half-cell arrangement thereby allowing for comparison to our model. The model domain was a 2D cross-section of an electrode spanning 2 half-channels and a full rib, representative of one “unit cell” of an interdigitated flow field design. The cell dimensions and boundary conditions are shown in Figure 4-1. The electrolyte was injected from the top face rather than the edge as would be the case for a flow-through arrangement. The size of inlet and outlet boundaries were set as half of the rib width (1 mm), meaning the channel-to-rib width ratio was 1. Messaggi et al [139] used a commercial carbon paper electrode, SGL39AA, so for the validation of the present model the electrode properties of this material were used. Because the thickness of

single carbon paper electrode in a cell was 280  $\mu\text{m}$ , this was used as the domain for thickness.

For all the subsequent multilayered cases three layers, each of 93.33  $\mu\text{m}$ , was used so as to provide equivalent total electrode thickness for comparison.



a)



b)

**Figure 4-1 - Domain of cathode containing a) single, and b) multi-layer with boundary conditions applied on Multiphysics simulation**

The following single redox reaction occurred in the cathode:



Steady-state and isothermal conditions were assumed. The conservation of each ionic species at the liquid electrolyte was presented according to Eq.4-2:

$$\nabla \cdot N_i = S_i \quad 4-2$$

where  $S_i$  denotes the source term depending on the electrochemical reaction rate,  $i_{cat}$ , as indicated in Eqs.4-3, 4-4, and 4-5.

$$S_{VO^{2+}} = -\frac{i_{cat}}{F} \quad 4-3$$

$$S_{VO_2^+} = \frac{i_{cat}}{F} \quad 4-4$$

$$S_{H^+} = \frac{2 i_{cat}}{F} \quad 4-5$$

where  $F$  is Faraday's constant.

#### 4.2.2. Ion Transportation

The Nernst-Planck equation was used to represent the flux of ionic species,  $N_i$  ( $VO_2^+$ ,  $VO^{2+}$ ,  $H^+$ ,  $HSO_4^-$ ) in the presence of both concentration and voltage gradients, while the concentration of  $SO_4^{2-}$  was calculated from the electroneutrality principle ( $\sum_n z_i^n c_i^n = 0$ ), as given in Eq.4-6:

$$N_i = -D_{i,eff} \nabla c_i - z_i U_{i,eff} F c_i \nabla \phi_l + u \cdot c_i \quad 4-6$$

where  $z_i$  is the charge number,  $\phi_l$  is the potential of the liquid electrolyte, and  $c_i$  is the molar concentration. The diffusive flux through a porous electrode is less than through open space, reduced by the porosity as well as the geometric specifics of the void space, typically ascribed to tortuosity. Thus, the diffusion coefficient of each species,  $D_i$ , was converted into the effective value using Eq.4-7.

$$D_{i,eff} = \frac{\varepsilon}{\tau} D_i \quad 4-7$$

where  $D_{i,eff}$  is the effective diffusion coefficient, and  $\varepsilon$  is the porosity of fibrous electrode. The tortuosity of the cathode,  $\tau$ , was obtained from the percolation thresholds and Archie's law parameters [24].

$$\tau = \left( \frac{1 - \varepsilon_p}{\varepsilon - \varepsilon_p} \right)^\alpha \quad 4-8$$

where  $\varepsilon_p$  is the percolation threshold, and  $\alpha$  is the Archie's law parameter. Note that tortuosity is dependent on the specific details of the solid structure and is direction dependent. In the case of randomized fibrous structure, we used values proposed by Tomadakis et al [140]. A percolation threshold of  $\varepsilon_p = 0.11$  was used in both in-plane and through-plane directions; however, the Archie's law parameter was direction dependent:  $\alpha = 0.521$  for in-plane and  $\alpha = 0.785$  for through-plane transport.  $U_{i,eff}$  is the effective ionic mobility derived by Nernst-Einstein equation [141].

$$U_{i,eff} = \frac{D_{i,eff}}{RT} \quad 4-9$$

where  $R$  is the gas constant,  $T$  is the temperature. The velocity of the electrolyte,  $u$ , was expressed based on Darcy's law modified from Eq.2-1 [142].

$$\vec{u} = -\frac{K}{\mu} \nabla P \quad 4-10$$

where  $\mu$  is the dynamic viscosity,  $\Delta P$  is the pressure drop across the electrode, and  $K$  is the permeability. The permeability of fibrous material is well described by the Carman-Kozeny theory in Eq.2-3 [66,143,144], which provides a convenient correlation in terms of controllable and measurable structural features. In Eq. 2-3,  $k_{CK}$  is a fitting parameter which accounts for the material structure, such as fiber morphology, orientation, and shape. Note that the velocity predicted by Darcy's law is a vector quantity, implying that permeability is direction dependent. Since neither  $d_f$  or  $\varepsilon$  are direction dependent, this means that  $k_{CK}$  varies with direction. It has been shown for instance that  $k_{CK}$  varies between 4 and 8 between two perpendicular in-plane directions of a material with some degree of fiber alignment [145]. This fact will be leveraged below.

#### 4.2.3. Electrochemical Reaction

The local current generated by the reaction between the catholyte and cathode was described by the Butler-Volmer equation:

$$i_{cat} = k_o A_s F \left[ c_{VO^{2+}}^s e^{\frac{\alpha \eta F}{RT}} - c_{VO_2^+}^s e^{\frac{-(1-\alpha) \eta F}{RT}} \right] \quad 4-11$$

where  $i_{cat}$  is the generation rate of current,  $c_{VO^{2+}}^s$  and  $c_{VO_2^+}^s$  are  $VO^{2+}$  and  $VO_2^+$  concentration on the surface of fiber,  $\alpha_{cat}$  is the dimensionless transfer coefficient. The volumetric surface area of a fibrous electrode,  $A_s$ , was calculated using Eq.2-6 [24]. Eq.2-6 is called the filament analog model, and it estimates the surface area of a fibrous material as a collection of non-intersecting cylinders.  $\eta$  is the overpotential defined as the interfacial potential difference between ion (electrolyte) and electron (solid carbon) phase, defined as:

$$\eta_{cat} = \phi_s - \phi_l - E_{oc} \quad 4-12$$

where  $E_{oc}$  is the open circuit voltage determined by the half-cell cathode reaction, and  $\phi_s$  and  $\phi_l$  are the potential at solid and liquid phase. In practice, the open circuit voltage is derived from thermodynamic analysis based on Nernst equation, shown below.

$$E_{oc} = E^0 + \frac{RT}{F} \ln \left( \frac{C_{VO^{2+}}}{C_{CO_2^+} C_{H^+}^2} \right) \quad 4-13$$

where  $E_0$  is the standard potential at the half-cell cathode, and  $C_{H^+}$  is proton concentration. However, Messagi et al [139] experimentally found the open circuit voltage of the half-cell [ $\sim 1.13V$ ] at 60% State of Charge (SOC), and thus it was directly applied to the model in this study. The species transport in electrolyte, electrochemical reaction, and the current in the solid phase are all coupled through the conservation of charge. Thus, the potential at each liquid and solid phase were obtained from the electron and proton conservation expressed in Eqs.4-14, 4-15, and 4-16.

$$i_s = -\sigma_{s,eff} \nabla \phi_s \quad 4-14$$

$$i_l = F \sum_i z_i (-D_{i,eff} \nabla c_i - z_i U_{i,eff} F c_i \nabla \phi_l + u \cdot c_i) \quad 4-15$$

$$-\nabla i_s = \nabla i_l = S_R \quad 4-16$$

$$i_l = -\sigma_l \nabla \phi_l \quad (\text{In membrane}) \quad 4-17$$

where  $i_l$  is the current density at the liquid electrolyte,  $\sigma_s$  and  $\sigma_l$  are the electrical and ionic conductivities in the solid carbon and electrolyte phases. The boundary condition at the membrane was expressed with Eq.4-17. The conductivity at the solid phase depends on the structure of porous electrode, and thus was converted into the effective value as follows:

$$\sigma_{s,eff} = (1 - \varepsilon)^{3/2} \sigma_s \quad 4-18$$

In addition, the consumption rate of ions was related to the diffusion occurred by the concentration difference between bulk and solid surface, as modeled by the film transfer theory of mass transfer below. Since the discharging process was considered in this study,  $VO_2^+$  transferred from bulk to fiber surface while  $VO_2^{2+}$  is transported in the opposite way.

$$-A_s h_m F (c_{VO_2^{2+}}^s - c_{VO_2^{2+}}^b) = i_{cat} \quad 4-19$$

$$A_s h_m F (c_{VO_2^+}^s - c_{VO_2^+}^b) = i_{cat} \quad 4-20$$

where  $h_m$  represents the pore-level mass transfer coefficient, which was obtained from the expression in terms of the superficial velocity, as shown in Eq.4-21 [146]:

$$h_m = 1.6 \times 10^{-4} \cdot u^{0.4} \quad 4-21$$

By combining all the properties, the Butler-Volmer expression in Eq.4-11 was rearranged to Eq. 4-22 [139].

$$i_{cat} = \frac{k_o A_s F}{1 + \frac{k_o}{h_m} \left( e^{\frac{\alpha \eta F}{RT}} - e^{-\frac{(1-\alpha) \alpha \eta F}{RT}} \right)} (c_{VO_2^{2+}}^b e^{\frac{\alpha \eta F}{RT}} - c_{VO_2^+}^b e^{-\frac{(1-\alpha) \alpha \eta F}{RT}}) \quad 4-22$$

#### 4.2.4. Dissociation of Sulfuric Acid

The dissociation takes place as a parallel reaction with the sulfuric acid in two-steps, which provides additional protons. In this study, the sulfuric acid was assumed to be a strong acid, and thus the first step of the dissociation below was fully complete. The dissociation rate of the second step was expressed using Eq.4-23.



$$r_d = k_d * (-\beta) \quad 4-23$$

where  $r_d$  is the dissociation source term,  $k_d$  is the dissociation reaction coefficient, and  $\beta$  is the degree of dissociation of  $HSO_4^-$  which is determined experimentally [139].

#### 4.2.5. State of Charge (SOC)

The concentration of each ionic species at the inlet boundary changes depending on the state of charge (SOC). In this study, SOC was set at 60% to validate the model with the experimental data given by Messaggi et al [139]. The inlet concentrations were expressed in terms of SOC, as indicated in Eqs. 4-24, 4-25, 4-26, and 4-27.

$$c_{VO^{2+}} = (1 - SOC) * c_{VO_2^+,in} \quad 4-24$$

$$c_{VO_2^+} = SOC * c_{VO_2^+,in} \quad 4-25$$

$$c_{H^+} = c_{acid} - (1 - SOC) * c_{VO_2^+,in} \quad 4-26$$

$$c_{HSO_4^-} = c_{acid} + c_{VO_2^+,in} \quad 4-27$$

#### 4.2.6. Model Parameters

The values of general parameters applied in the model were listed in Table 4-1. The specific physical properties of electrodes, such as Carman-Kozeny constants, fiber size, and

porosity, were varied at each layer, as indicated in Table 4-1 and Table 4-2. The model described above was solved using COMSOL Multiphysics.

**Table 4-1 - Fixed model parameters**

Symbol	Description	Value	Reference
$C_{VO_2^+,in}$	$VO_2^+$ inlet concentration ( $mol/m^3$ )	1000	[139]
$D_{VO_2^+}$	$VO_2^+$ diffusion coefficient ( $m^2/s$ )	$3.9 \times 10^{-10}$	[147]
$D_{VO_2^+}$	$VO_2^+$ diffusion coefficient ( $m^2/s$ )	$3.9 \times 10^{-10}$	[147]
$D_{H^+}$	$H^+$ diffusion coefficient ( $m^2/s$ )	$9.312 \times 10^{-9}$	[142]
$D_{SO_4^{2-}}$	$SO_4^{2-}$ diffusion coefficient ( $m^2/s$ )	$1.065 \times 10^{-9}$	[142]
$D_{HSO_4^-}$	$HSO_4^-$ diffusion coefficient ( $m^2/s$ )	$1.33 \times 10^{-9}$	[142]
$F$	Faraday's constant (C/mol)	96485	[139]
$k_d$	$HSO_4^-$ dissociation reaction rate ( $s^{-1}$ )	$1 \times 10^{-4}$	[139]
$k_o$	Reaction rate constant (m/s)	$5 \times 10^{-7}$	Fitted
$P_{out}$	Pressure at the outlet of electrode domain (Pa)	$1 \times 10^5$	Fitted
$R$	Gas constant ( $m^3 \cdot Pa/mol \cdot K$ )	8.314	[139]
$SOC$	State of Charge	0.6	[139]
$T$	Temperature (K)	298	[139]
$V_{oc}$	Open circuit voltage (V)	1.13	[139]
$\alpha$	Charge transfer coefficient	0.5	[148]
$\alpha'_x$	Archie's Law parameter at in-plane direction	0.521	[61]
$\alpha'_y$	Archie's Law parameter at through-plane direction	0.785	[61]
$\beta$	$HSO_4^-$ degree of dissociation	0.25	[139]
$\epsilon_p$	Percolation threshold	0.11	[61]
$\mu$	Dynamic viscosity of catholyte ( $Pa \cdot s$ )	0.005	[142]
$\rho$	Density of catholyte ( $kg/m^3$ )	1350	[149]
$\sigma_l$	Membrane conductivity (S/m)	2	fitted
$\sigma_s$	Electrode conductivity (S/m)	1000	[150]

**Table 4-2 - Transport related parameters used in each study**

	Electrode Details			
	3L	3L:kCK	3L:df	4L:eps

$\varepsilon$	Layer 1	0.859	0.859	0.859	0.809
	Layer 2	0.859	0.859	0.859	0.859
	Layer 3	0.859	0.859	0.859	0.909
$k_{CK,TP}$	Layer 1	8	16	8	8
	Layer 2	8	8	8	8
	Layer 3	8	4	8	8
$k_{CK,IP}$	Layer 1	4	8	4	4
	Layer 2	4	4	4	4
	Layer 3	4	2	4	4
$d_f [\mu m]$	Layer 1	1	1	0.2	1
	Layer 2	1	1	1	1
	Layer 3	1	1	1.8	1
$K_{TP} [\mu m^2]$	Layer 1	0.25	0.125	0.01	0.113
	Layer 2	0.25	0.25	0.25	0.25
	Layer 3	0.25	0.5	0.81	0.71
$K_{IP} [\mu m^2]$	Layer 1	0.5	0.25	0.02	0.227
	Layer 2	0.5	0.5	0.5	0.5
	Layer 3	0.5	1	1.61	1.417

#### 4.2.7. Model Validation

The model was validated by comparing the polarization behavior with the experimental data obtained by Messaggi et al [139]. The properties of SGL39AA were applied in the electrode domain. The fiber size in SGL39AA is 8  $\mu m$  in diameter and the porosity was measured experimentally as 0.88 [151]. However, they state that the sample was compressed by 15% when assembled in the cell, thus the porosity was adjusted to 0.859 based on this compression, as outlined by Messaggi et al [139]. The general values of Carman-Kozeny constants were applied (4 at in-plane and 8 at through plane direction) from Gostick et al [66]. The average velocity of the electrolyte at the inlet of the interdigitated flow channel was calculated using the equation below [77,152].

$$u_{in,avg} = \frac{Q}{N_{c,in} W_c L_c} \quad 4-28$$

where  $u_{in,avg}$  is the average velocity at the inlet channel path,  $Q$  is the volumetric flow rate,  $N_{c,in}$  is the number of channels at the inlet,  $W_c$  is the width of channel, and  $L_c$  is the length of channel. The channel dimensions were taken from the geometry of the interdigitated flow channels used by Messaggi et al [139]. The volumetric flow rates of 10, 20, and 60 ml/min were considered to match the result with the experimental data. As these flow rates were the total flowing into the cell, it was necessary to determine the actual flow velocity in the flow channel. Their cell consisted of 12 channels with a 1 mm width and length of 5 cm, corresponding to average superficial velocities of  $2.62 \times 10^{-4}$  m/s,  $5.24 \times 10^{-4}$  m/s and  $15.72 \times 10^{-4}$  m/s at 10, 20 and 60 ml/min, respectively. Values of all parameters applied to the domain are given in Table 4-1. Membrane conductivity ( $\sigma_l$ ) and reaction rate constant ( $k_o$ ) were the only parameters adjusted to fit the model to the experimental results. According to Tsampas et al [153], the conductivity of the membrane ranges from 1 to 5 S/m depending on its thickness, and thus the fitted value (2 S/m) falls well within the acceptable range. As shown in Figure 4-2, the polarization behavior predicted by the model at each flow rate is close to the experimental data, validating the qualitative and quantitative capabilities of the model.

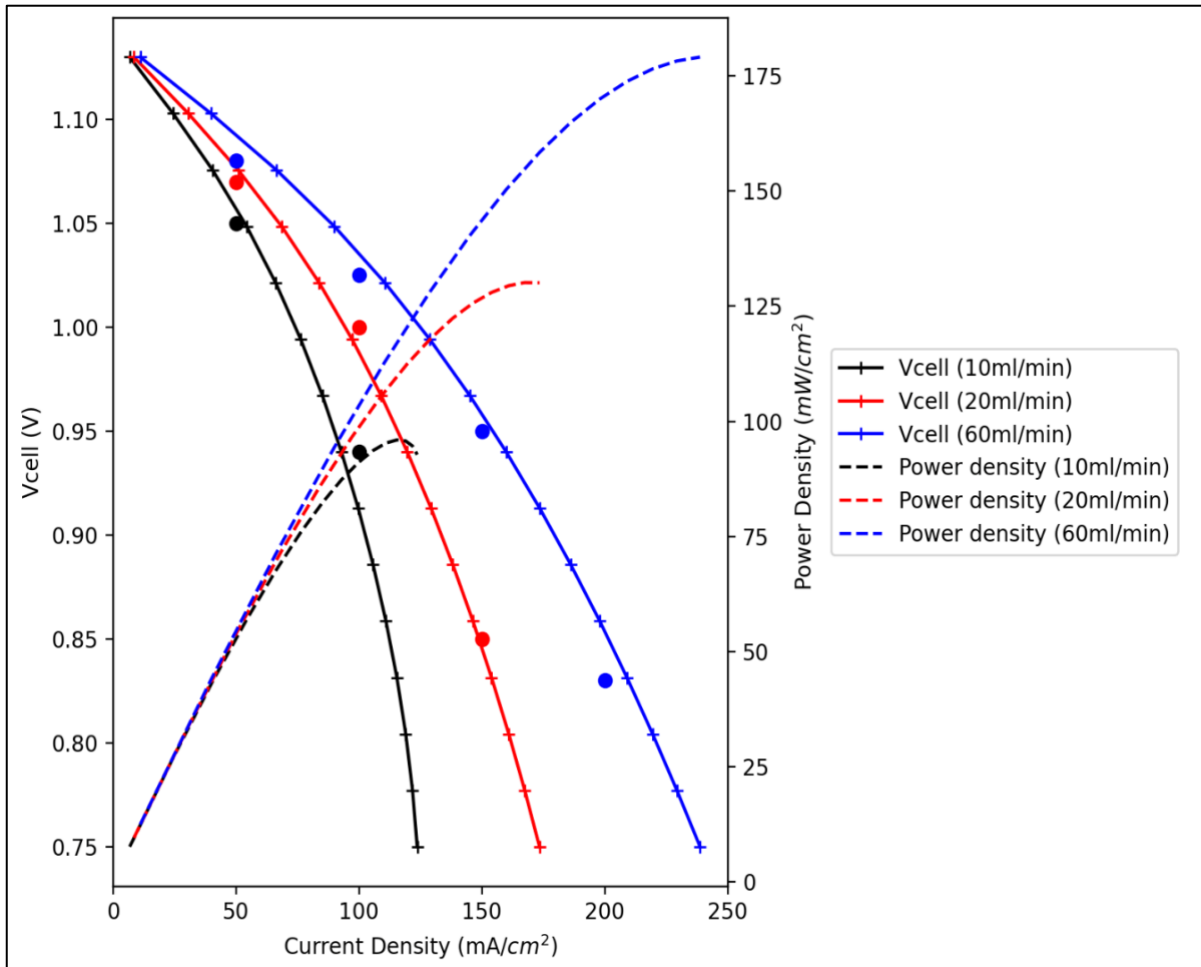


**Figure 4-2 – Polarization and power density curves at different flow rate of electrolyte across the SGL39AA domain**

### 4.3. Results and Discussion

#### 4.3.1. Baseline Case: Electrospun Electrodes with Same Properties in All Layers

Electrospun fibrous electrodes are appealing for use in vanadium redox flow batteries due to their high specific surface area. According to Liu et al [24], fiber sizes of approximately  $1 \mu m$  can be achieved with solutions containing 10 wt% of polyacrylonitrile in N,N, dimethylformamide so this was considered as the baseline size in this study, which was varied higher and lower as discussed later. In agreement with what has been seen experimentally [138], the present model indeed predicts the better polarization performance of the electrospun material over the entire range of current density, as shown in Figure 4-3a) and b).

The lines with circular markers are for the baseline case where all three layers have the same nominal properties, while the black lines indicate the performance of the SGL39AA material used in the validation study under directly comparable conditions. To avoid cluttering the graph only the line for the lowest and highest flow rate are shown to indicate the range.

Electrospun fibrous electrodes are appealing for use in vanadium redox flow batteries due to their high specific surface area. According to Liu et al [24], fiber sizes of approximately 1  $\mu\text{m}$  can be achieved with solutions containing 10 wt% of polyacrylonitrile in N,N-dimethylformamide so this was considered as the baseline fiber size in this study, referred to as sample 3L. In agreement with experimental data [138], the model predicts the electrospun electrodes performs better than the commercial carbon fiber materials, as shown in Figure 4-3.

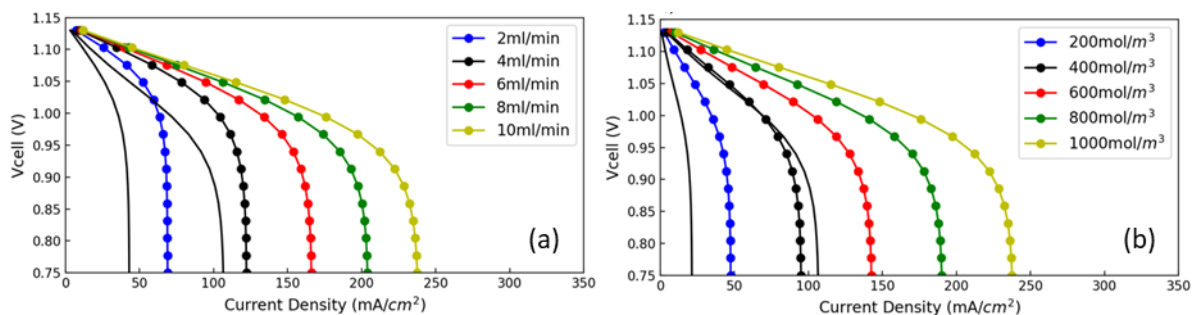


**Figure 4-3 - Polarization curves for the baseline case. Panel (a) shows the performance as a function of fluid flow rate for a constant inlet concentration of  $1000 \text{ mol/m}^3$ . Panel (b) shows the case for different inlet concentrations at a constant flow rate of  $10 \text{ mL/min}$ . The black lines represent the SGL39AA material at the highest and lowest value of the varied parameter to indicate the performance range.**

As expected, the current density at a given voltage increases with the flow rate since even at low current density, when mass transfer limitations are considered unimportant, the reaction rate as described by Eq.4-19 and 4-20 is still proportional to the flow rate of electrolyte (Eq.4-21). This underscores the importance of having electrodes with high permeability so that high flows can be applied to reduce overpotential without incurring excessive pumping

cost. The tradeoff between pumping cost and cell performance in these electrospun electrodes is discussed later.

An additional interpretation of the data shown in Figure 4-3 can be obtained by converting the current density to the electrochemical conversion factor,  $X$ , as follows:

$$X = \frac{I}{(C \times Q)zF} \quad 4-29$$

where  $I$  is the current observed in the cell and the denominator is the total possible current that could be generated at the given flow rate ( $Q$  in  $\text{m}^3/\text{s}$ ) and concentration ( $C$  in  $\text{mol}/\text{m}^3$ ) if all the reactants were consumed. This interpretation is shown in Figure 4-4. Figure 4-4(a) shows that as the flow rate increases, the conversion decreases, which can be understood in terms of a reduced residence time. A useful feature of Figure 4-4 is the maximum value of  $X$  that is obtained for each condition is a function of the electrode architecture. For the case of the baseline electrospun material, at a flow rate of 10 ml/min and inlet concentration of 1000  $\text{mol}/\text{m}^3$ , the maximum conversion is around  $X_{max} = 0.62$ . By contrast the commercial material only achieved  $X_{max} = 0.28$  under the same conditions. As will be shown below, the value of a  $X_{max}$  is a characteristic of the material structure and also correlates directly with the maximum power density.

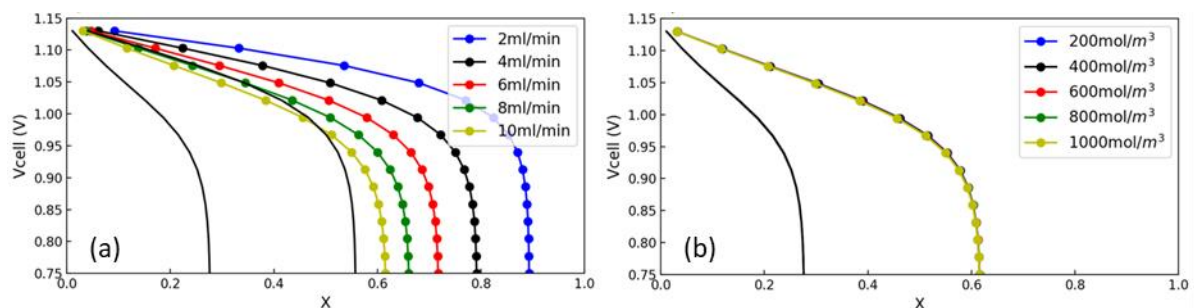


**Figure 4-4 - Polarization behavior plotted against electrochemical conversion factor. Panel (a) shows the performance as a function of fluid flow rate for a constant inlet concentration of 1000  $\text{mol}/\text{m}^3$ . Panel (b) shows the case for different inlet concentrations at a constant flow rate of 10 mL/min. The black lines represent the SGL39AA material at the highest**

*and lowest value of the varied parameter to indicate the performance range.*

#### 4.3.2. Varying Properties Between Layers

The baseline case in the previous section had the same properties applied to all layers, so it acted like a single layer structure. As was observed, the performance, as judged by limiting current or maximum electrochemical conversion, was higher than the commercial materials, but still showed room for improvement. In a recent study we explored the behavior of a multi-layered electrode with different porosity in each layer using a pore network model [154]. In this section we revisit some of those designs and consider changes in the fiber size and fiber alignment (which impacts that value of the permeability coefficient). Accordingly, we first look at sample 3L:eps, where the porosity was varied between the layers with a lower porosity near the rib and the highest porosity near the membrane. This corresponds with the L-M-H case of Misaghian et al [154], but the changes between layers are not as extreme, varying by 5% between layers instead of 10%. Along the same vein, in Sample 3L:df we use 3-layer arrangements with smaller fibers near the rib and larger fiber near the membrane since this would create the same trend in permeability between layers as 3L:eps. And similarly, in Sample 3L:kCK we varied the Carman-Kozeny constants for the in-plane and through-plane direction to capture the effect of anisotropy, such that the permeability was lower near the rib and higher near the membrane, also the same trend as the other samples. Table 4-2 also includes the resultant in-plane and through-plane permeabilities at each layer, and it can be confirmed that in all cases the layer near the membrane had the highest permeability. The polarization behavior of all these cases is shown together in Figure 4-5. The first trend to note is that all the interventions resulted in notable increases in the limited current density. Specifically, the limiting current in the best performing case (3L:df) is approximately 25%

improved over the baseline case (3L).

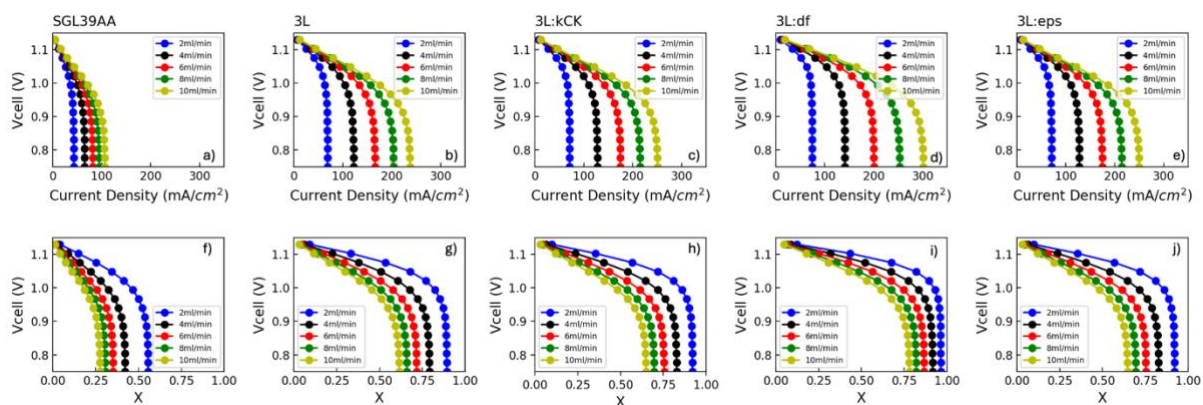


**Figure 4-5 – Complete set of polarization curves for all 5 electrode materials studied here as a function of electrolyte flowrate for a constant inlet concentration of  $1000 \text{ mol/m}^3$ . Panels (a-e) show the standard polarization curve while panels (f-j) show the electrochemical conversion defined by Eq.4-29.**

The result of converting the current density to an electrochemical conversion is shown on the bottom rows of Figure 4-5. The most notable feature is that for a fixed set of conditions (i.e. the same flow rate and inlet concentration), the value of  $X_{max}$  differs between electrodes. This suggests that  $X_{max}$  could potentially be used as a single metric to quantify the relative performance of an electrode material. Figure 4-6 shows the polarization behavior at a constant flow rate ( $10 \text{ mL/min}$ ) while varying the inlet concentration. The most striking feature of this data is that the  $X_{max}$  value for a given electrode is independent of the concentration. This lends even more support to the use of  $X_{max}$  as a useful metric to compare different electrodes.

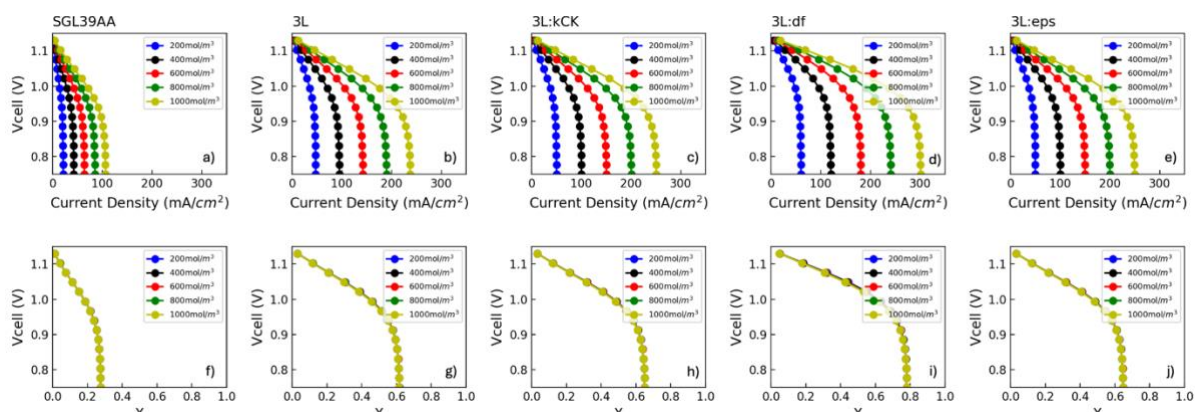


**Figure 4-6 - Polarization curves for all electrodes studied here as a function of inlet concentration at a constant flow rate of 10 mL/min. Panels (a-e) shows the standard polarization curves while panels (f-j) show the electrochemical conversion defined by Eq.4-29.**

The behavior of  $X_{max}$  is summarized in Figure 4-7. What this graph shows more clearly is that the maximum conversion for a given electrode is essentially independent of inlet concentration of reactant while it decreases with increasing flow rate of electrolyte. The independence of  $X_{max}$  on  $C$  suggests that an electrode's  $X_{max}$  value is a concise metric for quantifying its relative performance. For instance, since actual performance depends on the concentration or state-of-charge, comparing electrodes based on their peak power or limiting current is situation dependent. However, the  $X_{max}$  value for an electrode is a universal value that correlates directly with maximum current density regardless of state-of-charge. Figure 4-7(a) shows  $X_{max}$  does depend on flow rate, which is expected since the residence time changes. However, it is still noteworthy that the trends agree with the performance of each electrode. For instance, the 3L:df electrode performed the best in terms of standard polarization, and also shows the highest trend of  $X_{max}$  values.

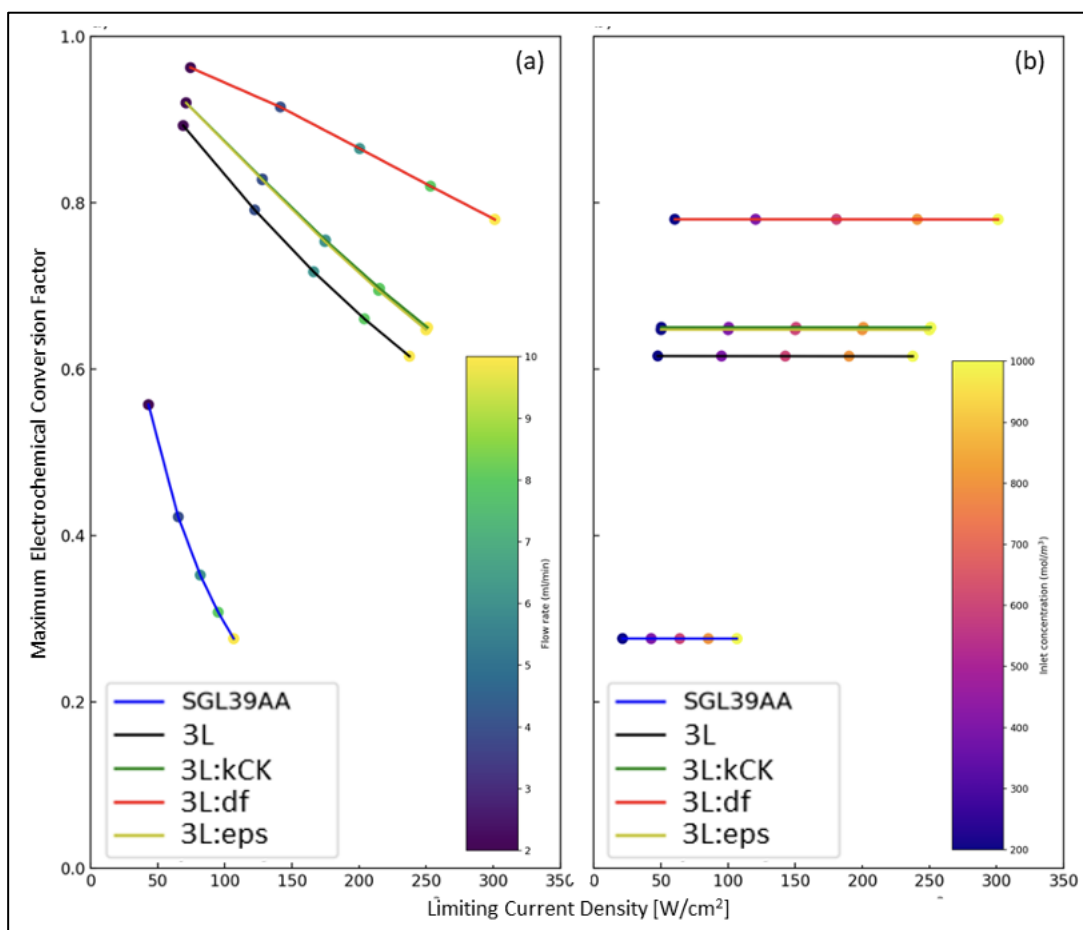


**Figure 4-7 – Maximum electrochemical conversion factor as a function of limiting current density. Points for each electrode structure are connected by a colored line according to the legend. The marker colors indicate a) flow rate of electrolyte and b) inlet concentration of  $VO_2^+$**

#### 4.3.3. Pumping Cost Analysis

Clearly a sizable increase in current and power density can be achieved by customizing the properties of each layer. The permeability values listed in Table 4-2 for each layer reveal that the electrospun samples are less permeable than commercial materials, so it is expected that pressure drops will be higher, and thus so will the pumping cost. It is essential to also evaluate the pumping cost for these electrodes to understand whether or not the increased performance actually provides a net gain in power output. The pumping cost can be estimated as:

$$P_{pump} = \frac{Q\Delta P}{\varphi} \quad 4-30$$

where  $Q$  is the flow rate of the electrolyte introduced into the inlet boundary,  $\Delta P$  is the pressure drop across the electrode, and  $\varphi$  is the efficiency of the pump. For a real redox flow cell, the pumping power should be approximately doubled because separate pumps are required on each of the cathode and anode side. However, since only the half-cell (cathode) was considered in this study, the pumping power was calculated for only the cathode side. Also, the efficiency was assumed to be 100% to avoid confounding the analysis with externalities.

Knowing the pumping power, it is possible to adjust the cell power output to a net output. This is actually the key metric since the aim is to increase the *net* power output of the system, not just increase the power density of the electrode itself. In other words, obtaining a small increase in cell performance by incurring a larger increase in parasitic pumping cost is a net negative. A convenient way to quantify the impact of the pumping cost is to define the pumping efficiency:

$$\eta_{pumping} = \frac{V_{cell}i_{cell}A_{elec} - P_{pump}}{V_{cell}i_{cell}A_{cell}} \quad 4-31$$

where  $\eta_{pumping}$  is the pumping efficiency,  $V_{cell}$  is the cell voltage,  $i_{cell}$  is the current density provided, and  $A_{cell}$  is the area of electrode. Figure 4-8 shows the pumping efficiency for each electrode listed in Table 4-2 as a function of current density, flow rate, and inlet concentration. The effect of varying flow rate and inlet concentration on the pumping efficiency can be seen from the marker color. In all cases, the pumping efficiency rises sharply with increasing current, reaches a peak value, then decreases again. The initial low value is

because the power generated by the cell is very small at low currents, while the pumping power is constant. As current increases, the cell power becomes much larger than the pumping power, so the  $\eta_{pumping}$  rises. Eventually, the  $\eta_{pumping}$  drops again after peak power has been achieved in the cell since the pump power becomes a larger fraction of the power output again.

In Figure 4-8a), the higher flow rates could achieve higher currents, but at lower net efficiency due to extra pumping power required for operation. On the other hand, Figure 4-8b) shows that the efficiency is totally independent to the inlet concentration since the pumping power only relies on the flow rate of electrolyte. Consequently, the efficiency remained identical at all current densities.

In Figure 4-8, panels (a-d), it can be seen that higher flow rates result in lower  $\eta_{pumping}$  due to extra pumping power required for operation, despite the fact that these conditions result in the highest peak power and limiting currents (see Figure 4-5). On the other hand, Figure 4-8(e-h) shows that the efficiency is independent of the inlet concentration since the pumping power only depend on the flow rate of electrolyte and not the composition (assuming viscosity and density don't change substantially). Consequently, the pumping efficiency remained constant at all current densities.

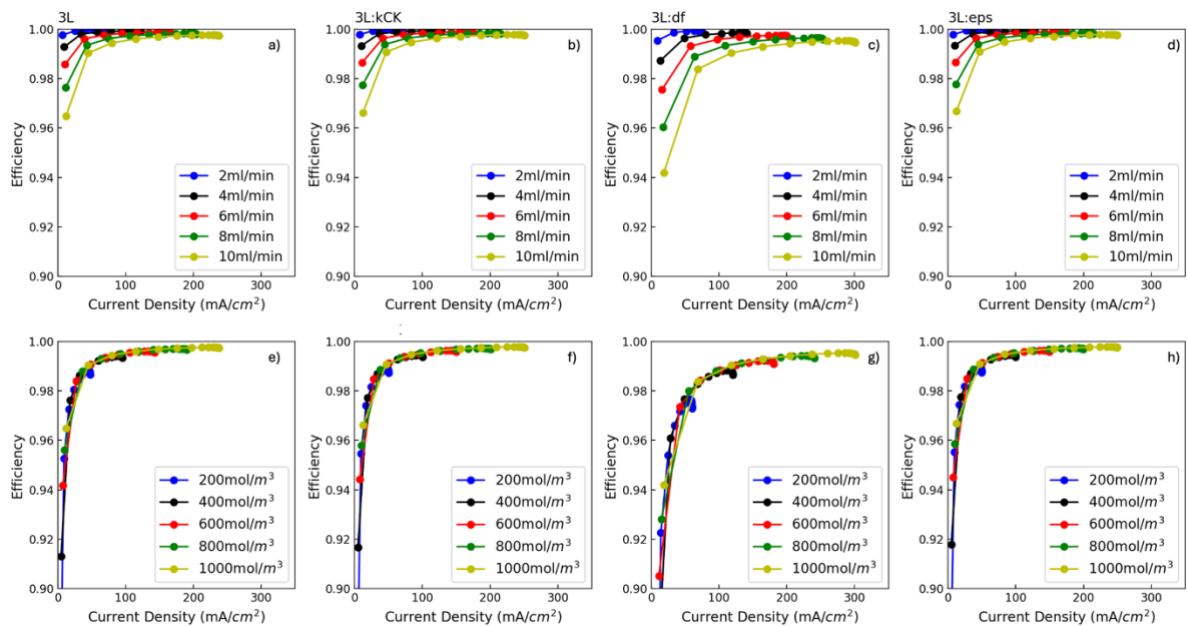


**Figure 4-8 – Pumping efficiency vs current density for all the multilayered structures. Panels (a-d) show the efficiency as a function of flow rate for a constant inlet concentration of  $1000 \text{ mol/m}^3$ . Panels (e-h) show the pumping efficient as a function of inlet concentration for a constant inlet flow rate of  $10 \text{ mL/min}$ ,**

The data from Figure 4-8 can be condensed by plotting the maximum pumping efficiency for each case as a function of the power generated at that point. Figure 4-9 therefore compares the pumping efficiency each flow rate, inlet concentration, and electrodes structures. Overall, the best performing structure in net power density was Sample 3L:df, which had different a fiber sizes in each layer. This result is meaningful since the modification which is beneficial to increasing power density can actually be a net negative once the pumping power is considered. Note that the SGL39AA sample had exceptionally high pumping efficiencies because it has large fibers thus high permeability. However, it is worth pointing out that the pumping efficiency for the custom electrospun samples was maintained at over 99% in all cases.

The analysis in terms of inlet concentration in Figure 4-9b) shows the opposite trend. The pumping efficiency increases at higher inlet concentration for all samples, due to the fact

that a greater amount of reactant is available for reaction while the flow rate was constant at 10 mL/min. In other words, the maximum *gross* power density increases with concentration, while pumping power remained constant. Thus, it would be beneficial if fresh electrolyte with a stable  $\text{VO}_2^+$  concentration was continuously injected rather than circulating the electrolyte. In this way, SOC would be fixed at 100% for the whole discharging period.

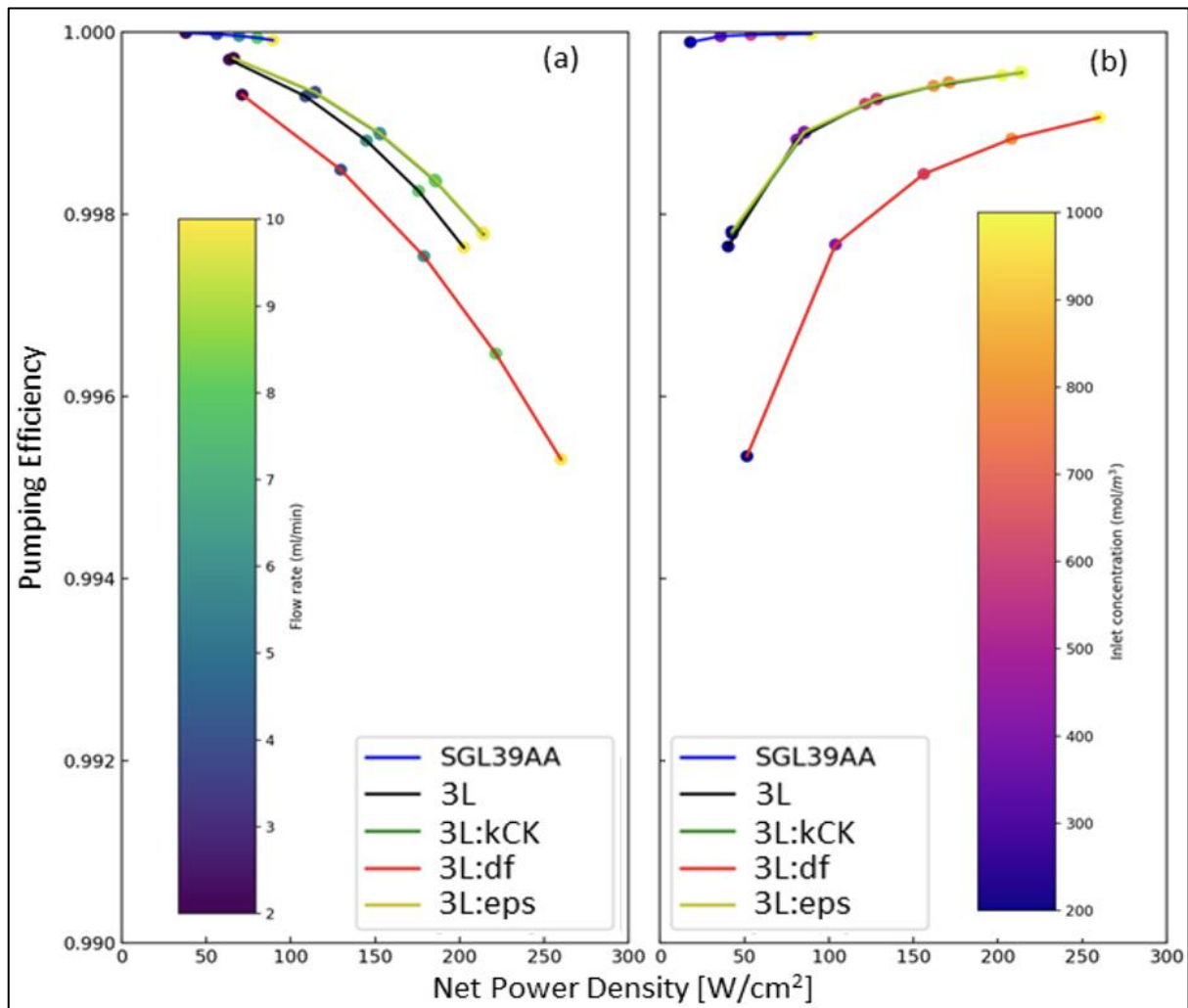


**Figure 4-9 – Peak values of pumping efficiency vs the net power density for each condition for all structures. Each line corresponds to a given material, indicated in the legend. Panel (a) shows the peak pumping efficiency as a function of flow rate for a constant inlet concentration of 1000 mol/m<sup>3</sup> with the color of each marking corresponding to the flow rate. Panel (b) shows the peak pumping efficient as a function of inlet concentration for a constant flow rate of 10 mL/min with the color of each marker corresponding to each concentration.**

#### 4.3.4. Optimization

In the above sections, each parameter in each layer was set to arbitrary values, but it is of interest to allow these parameters to vary freely in each layer to see if a combination can be found with a better overall performance. To this end COMSOL optimization feature was employed to find the best possible combinations. The flow rate of electrolyte was fixed at 10 mL/min while inlet concentration of  $VO_2^+$  was at  $1000 \text{ mol/m}^3$ , corresponding to a 60% state of charge. Upper and lower limits were specified for each parameter based on physically realizable properties. Starting with Sample 3L:cCK, the Carman-Kozeny constants were varied between  $k_{CK,IP}$  between 1 and 16, and  $k_{CK,TP}$  between 2 to 32. Along the same vein, in Sample 3L:df, the fiber size was varied between 0.2 and 1.8  $\mu\text{m}$ . Lastly, in Sample 3L:eps, the porosity was varied between 0.76 and 0.96. Table 4-3 shows the values of parameters at each layer where optimal net power density was approached for each case.

<b>Table 4-3 - Parameters determined by parameter sweep</b>		
Permeability Optimization (3L:kCK)		
	$k_{CK,IP}$	$k_{CK,TP}$
Layer 1 (Near Rib)	8.3397	24.261
Layer 2	3.2146	5.7526
Layer 3 (Near Membrane)	1.2881	2.0202
Fiber size optimization (3L:df)		
	Fiber size ( $\mu\text{m}$ )	
Layer 1 (Near Rib)	0.2	
Layer 2	0.2	
Layer 3 (Near Membrane)	0.328	

Porosity optimization (3L:eps)	
	Porosity
Layer 1 (Near Rib)	0.759
Layer 2	0.764
Layer 3 (Near Membrane)	0.819

Figure 4-10 shows the polarization curves for the three cases listed in Table 4-3. As before, the case with different fiber diameters in each layer provides the most improvement.

It can be confirmed in all cases that the layer near the membrane had the highest permeability, and the permeability decreases as getting close to rib. This arrangement tends to force the electrolyte to the region close to the membrane, which suggest that focusing the reaction zone closer to the membrane helps performance, presumably by reducing the pathlength required for the protons to react a reactive site.

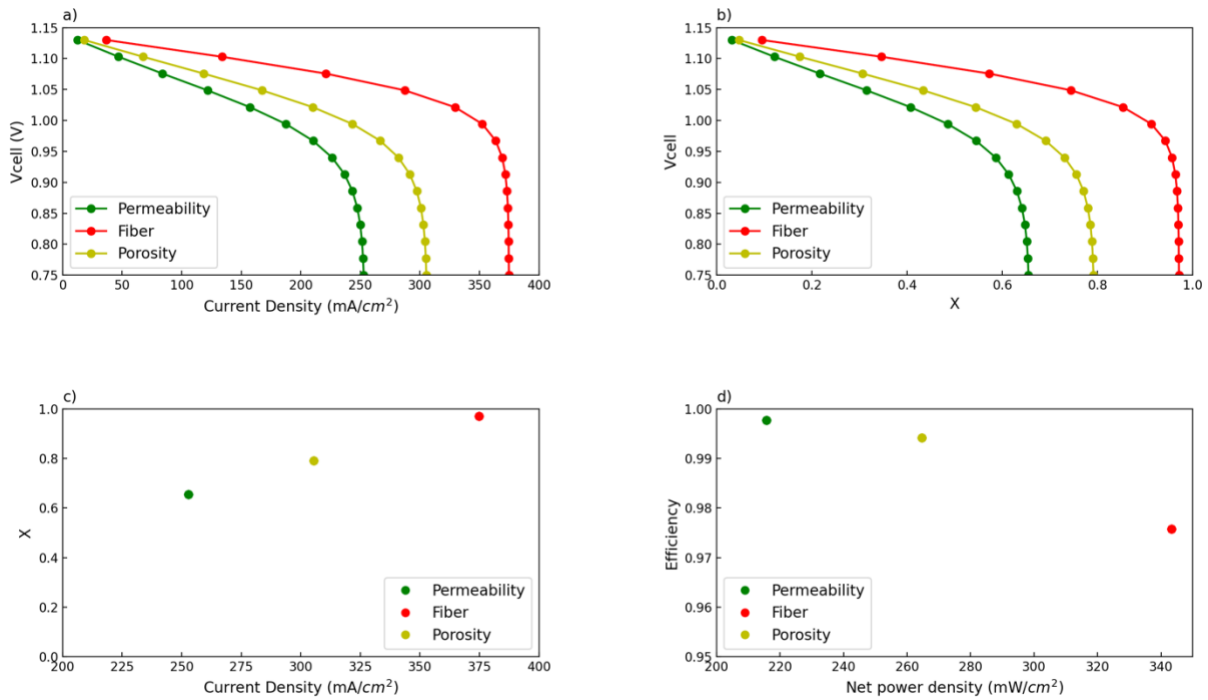


**Figure 4-10 – a) Polarization curve, b) the data with the current density expressed as electrochemical conversion factor, c) maximum electrochemical conversion factor as a function of peak current density, and d) peak values of net efficiency values vs the net power density obtained at that condition for multi-layered electrodes built with optimal conditions. All cases were using a flow rate of 10 mL/min and an inlet concentration of 1000 mol/m³.**

Also, Figure 4-10c) shows that the conversion factor could approach almost 100% with the multi-layered electrode with varying fiber size between layers, resulting in the highest maximum current density. This structure however provided to lowest pumping efficiency as shown in Figure 4-10d). However, although the pumping efficiency was reduced by 2% (99% to 97%) this provided a 57% increase in maximum net power density compared to the sample with varying  $k_{CK}$  between layers which was the next best performing material (220  $\text{mW}/\text{cm}^2$  to 345  $\text{mW}/\text{cm}^2$ ).

#### 4.4. Conclusion

This study validated and extended a multiphysics performance model of multi-layered

fibrous electrodes for a vanadium redox flow battery cathode. The main aim of the model was to assess the relative impact of varying physical properties in a 3-layered electrode structure. This model had the additional benefit that pumping cost could be calculated and weighed against the realized performance gains. Pumping cost analysis for novel electrode structures has not been extensively explored in most existing literature. The result showed that placing a layer with higher overall permeability near the membrane resulted in improved performance and lower pumping cost. The increase in performance was attributed to the shifting of the reaction zone towards the membrane, resulting in shorter path lengths for ion transport and reduced ohmic loss. The reduced pumping cost was the result of providing a high permeability layer. Crucially, a layered structure was necessary to force the flow closer to the membrane, so three layers of high permeability would not achieve the same benefit.

A “pumping efficiency” was defined as the ratio of the net power output by the cell (gross power less the pumping power) to the gross power output. For commercial electrodes with large fibers and high permeability this value was above 99%, since the pumping power was quite low. For the multilayer electrodes studied here the pumping efficiency dropped to between 97 and 98%. This relatively small drop may be worthwhile given that very substantial increases in current and power density were obtained, though this tradeoff needs to be considered on a case-by-case basis.

Additionally, current density was converted to an electrochemical conversion factor. It was found that for a given flow rate, each electrode presented a unique value. Higher performing electrodes, in terms of limiting current density and power density, tended to have a higher electrochemical conversion factor, but this value was independent of inlet concentration, unlike peak power or limiting current, so could potentially provide a more general metric for comparing electrodes between different settings.

Overall, this work illustrates that multilayered structures made from electrospun fibers outperform single layer structures substantially by directing the flow to strategic locations. Moreover, the layered structure allowed these higher performance results to be achieved while simultaneously reducing the pumping cost. The additional pumping cost incurred by the higher performance electrodes, compared to commercial materials, is not negligible but is relatively small compared to the increase in power density. In cases where a small footprint is required electrospun multilayered electrodes could provide a useful option.

#### **4.5. Acknowledgements**

This work was supported by the Natural Science and Engineering Research Council (NSERC) of Canada through the CREATE ME2 program.

## **5. Multi-layered Structure Built with Compressed and Laser Perforated Electrospun Fibrous Electrode for Vanadium Redox Flow Battery**

### **5.1. Introduction**

Fossil fuels have been the primary energy source worldwide for several centuries, but this long-standing dependence needs to end soon. Not only do they cause green-house gas emission, leading to climate changes thereby global warming, but they are a finite natural resource facing danger of depletion, predicted for exhaustion within 100 years [155]. Not to mention the other various pollutants caused by fossil fuel causing damage ecosystems as well as human health [156,157,158]. In order to overcome these problems, renewable energy such as solar and wind must be harnessed. However, they depend on weather conditions, leading to unstable electric grids [159,160,161,162,163,164]. Energy storage systems (ESS) is the general name of the devices that can be used to solve this problem. In practice, ESS are categorized depending on the form of energy stored. Batteries, for instance, store energy in the form of chemical energy and convert back to electrical energy when needed. In practice, the ESS with batteries have been utilized in various applications, such as portable devices, transport vehicles, and stationary energy resources [165,166,167,168,169]. Another type of battery that is of particular interest for large-scale storage is the vanadium redox flow battery because of its safety and high efficiency. However, the vanadium redox flow battery is not yet widely commercialized due to its lower energy and power density. In the case of vanadium redox flow battery, the electric power is generated from the electrochemical reaction between ions in liquid electrolytes and carbonized surface of electrode. In other words, the rate of electrochemical reaction depends on the surface area of electrode. High surface area

electrodes are made of porous materials that also need to conduct electricity, like porous carbon. The challenge when using a porous electrode becomes effective delivery of reactants deep into the core of the porous domain. The electrode in a vanadium redox flow battery is in general composed carbonized fibers since this arrangement provides high specific surface area of active sites while the fibers allow for a stable mechanical structure, and of course being electrically conductive. One possible way of increasing the volumetric surface area is reducing the fiber size. Among various methods of making a fibrous layer, electrospinning is a good option for laboratory studies since it is convenient and flexible, and also has the potential for scale-up to larger volume production. Liu et al [24] controlled the fiber size by adjusting the wt % of polymer in solution. However, it has remained a challenge to make small fibers without also drastically reducing the permeability, constraining the electrolyte transportation or increasing the parasitic pumping power [61,66,67].

In addition to creating an electrode with increased surface area, the distribution of flow in the electrode is also quite important for overall performance. The flow channel is placed adjacent to the electrode to provide uniform ion distribution to the entire electrode. Various flow channel designs have been considered [170-182], but among them the flow-through mode with interdigitated flow field is the most promising option since it allows for forced convective transport with a short flow path. Darling et al [77] evaluated the performance of redox flow battery assembled with interdigitated flow channel design and observed significant decrease of pressure drop thus lower parasitic pumping losses compared to the case without any flow field (i.e., purely flow-through). However, the total active area of the cell is reduced because there exist “dead zones” above the channels [61]. Increased power density can be accomplished by reclaiming these dead-zones or by increasing the power in the active portions.

A path forward is therefore to simultaneously develop a fiber arrangement that promotes a more uniform reaction distribution while also maintaining small fiber sizes to keep the high overall specific surface area of active sites. This study will introduce the application of multi-layered structure built with novel electrospun fibrous material in an electrode to solve this problem. The compressed and laser perforated electrospun fibrous electrode developed by Lee et al [138] was applied to build multilayer electrodes, with each layer possessing different properties to support different processes.

## 5.2. Experimental Method

The electrospun fibrous electrode samples used in this chapter were manufactured as described in in Chapter 3. The Only difference was that the artificial holes were created at 1000  $\mu\text{m}$  intervals to create a constant hole density of 100 holes per 1  $\text{cm}^2$ .

### 5.2.1. Electrolytes

Vanadium oxysulfate ( $\text{VOSO}_4$ ) (Alfa Aesar, 99.9% purity) and sulfuric acid (Sigma Aldrich, 95.0-98.0%) were used without any additional treatment to make all the electrolytes used in this study. The electrolyte was prepared through the electrolysis, as mentioned in the previous literature [127]. Deionized water ( $>18.2 \text{ M}\Omega \text{ cm}$ ) was used to dilute the solution to the desired rate. For the cell performance tests, 20 mL of solution containing 1.6 M  $\text{VOSO}_4$  and 3 M  $\text{H}_2\text{SO}_4$  mixture was used in the catholyte reservoir while 10 mL of the same solution was used at the anolyte side. The electrolyte was prepared by charging at a constant current density of 20  $\text{mA cm}^{-2}$  with 1.65 V cut off voltage. Then, it was continued by switching to apply constant voltage of 1.65 V until the current density decreased down to a very low value (0.1  $\text{mA/cm}^2$ ), indicating nearly 100% state of charge (SOC) to oxidize the  $\text{V}^{4+}$  to  $\text{V}^{5+}$  in

the catholyte while reducing the  $V^{4+}$  to  $V^{2+}$  in the anolyte. After that, approximately 10 mL of  $V^{4+}/V^{5+}$  electrolyte at the catholyte was removed from the reservoir to balance the electrolyte capacity. Then, the charge-discharge experiments were started.

### 5.2.2. Cyclic Voltammetry

Cyclic voltammetry was performed to analyze the electrochemical properties of the custom electrodes. A solution containing 0.05 M  $VOSO_4$  and 3.0 M  $H_2SO_4$  was used as the electrolyte. Cylindrical graphite and Ag/AgCl electrode were used as counter and reference electrodes, and they were submerged into the electrolyte ca. 1.5 cm. Each electrospun and carbonized working electrode was cut into a 1.5 by 1.5 cm square and completely submerged. A potentiostat (SP-150) was used perform the tests over a voltage ranging from 0 to 1.5 V at a scan rate of 10 mV/s.

### 5.2.3. Flow cell validation

The electrochemical experiments were implemented at 25°C using a single flow cell (A-Cell, Redox-Flow, Denmark) for the electrolyte preparation as well as the polarization behavior. The polarization behavior was evaluated in potentiostatic mode. The interdigitated and parallel flow channels were used. Both designs were composed of 3.18 mm thick impregnated graphite having 1 mm wide and 1mm deep channel as well as 1 mm width of ribs. In the case of the interdigitated flow design, the pattern had 7 inlets and 7 outlets channels. The active area of the flow cell was 6.25 cm<sup>2</sup> with each electrode sample cut into 2.5 cm x 2.5 cm squared then sealed with a PTFE gasket. The gasket was compressed in 85-90% of electrode during assembly so that the sample can be compressed by 10%-15%. Nafion 117 (Nafion Store, Ion Power Inc) was submerged into DI water for 24 hours to be used as a membrane [126].

Furthermore, nitrogen gas was introduced into the system 30 minutes before and during the experiments to prevent the capacity fade in the presence of oxygen by oxidizing the active species in the electrolyte. The flowrate of the electrolyte was controlled by the peristaltic pump (Watson Marlow). The flowrate of electrolyte was consistently maintained at 10 mL/min. The polarization curve was obtained with a 30 second hold per step to analyze the cell power performance to ensure a steady state current density was attained. The cell is recharged at 1.65 V back to 100% SOC between each discharging step to retain polarization accuracy. The current density was recorded at the cell voltage from 0.6 to 1.45 V with 0.05 V interval between steps.

#### 5.2.4. Pumping power

The pumping power of the operating cell with each fibrous electrode was measured experimentally with the bench-scale Redox Flow Battery Tester and liquid vanadium electrolyte. These tests were performed at the same flow conditions as the electrochemical performance tests, but were done separately. Using the measured pressure drop and applied flow rate, the pumping power of the redox flow cell was calculated with Eq.2-2 [68] assuming 100% efficiency of the pump. In the case of the redox flow battery, the pumping power should be approximately doubled since a separate pump is operated at each of cathode and anode side. The viscosities of the two electrolytes may differ slightly causing minor differences, but this was assumed to be negligible.

Both interdigitated and parallel flow channel designs were considered for pumping power analysis. The liquid solution was introduced from the holes and left the cell through the holes at the outlet afterward. Similar as the case of polarization test, the thickness of the electrode was controlled by the PTFE gaskets. The gasket with 85-90% thickness of the uncompressed

sample was applied at each run such that when assembled operation, electrode compression is 10-15%.

For the experimental setup, pressure sensors (Omega Engineering Inc, PX409-050DWU5V, PX409-005CG10V, PX409-10WDWU5V) were connected to the inlet port. The specific model of sensor was used depending on the pressure drop so to maximize accuracy. The outlet was exposed to the atmospheric conditions, but the absolute pressure was obtained from a nearby weather station. The flowrate of solution was controlled by a syringe pump (New Era Pump Systems INC, NE-1010) connected upstream of the pressure sensor. The inlet pressure was measured at multiple volumetric flowrates ranging from 10 to 100 mL/min for each fibrous sample.

### **5.3. Results and Discussion**

#### **5.3.1. Characterization of samples**

In this study, the electrospun samples manufactured as described in Chapter 3 were utilized to create a multi-layer electrode structure to be used for *in situ* testing. Figure 5-1 shows the SEM of pristine and sintered electrospun fibrous electrodes as well as the artificial holes created by the CO<sub>2</sub> laser. As the figure shows, the fibers were condensed into a tighter arrangement during the compression step, leading to a higher volumetric specific surface area of active sites for the electrochemical reaction, but also worse mass transfer properties. Since both pristine and sintered samples were produced with identical electrospinning conditions, the absolute mass of solid phase was consistent for all compressions. However, the porosity was lower, so it follows that the size of the pore space between the fibers was reduced. In particular, it has been observed that the lower porosity near the surfaces hinders flow of electrolyte into the domain, as evidenced by the mass transfer limited performance seen in

related work [85]. In order to overcome this problem, artificial holes with 100  $\mu\text{m}$  in diameter were created via  $\text{CO}_2$  laser perforation, which is at least an order of magnitude larger than the natural pores among fibers, as shown in Figure 5-1d). Fortunately, the fibers around holes were not damaged by the laser so fluid could enter the domain via the inner perimeter of the perforations.

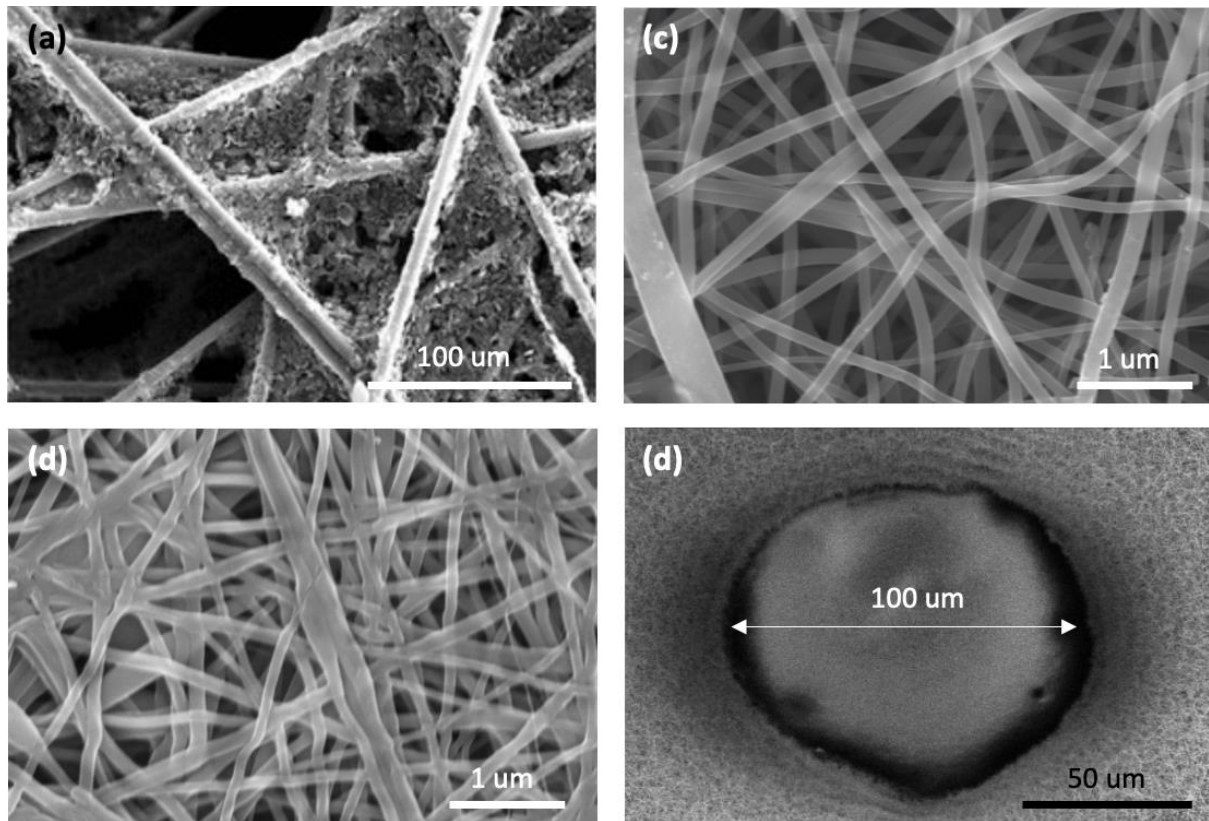


**Figure 5-1 - SEM images of a) pristine and b) sintered electrospun fibrous sample at the magnification of X20000, c) laser perforated hole with the magnification of x1600**

### 5.3.2. Cyclic Voltammetry

From the cyclic voltammetry analysis, the peak oxidation and reduction current density as well as the peak potential difference ( $\Delta E_p = E_{pa} - E_{pc}$ ) were observed to evaluate the electrocatalytic activity. Pristine and compressed electrospun samples were made in identical thickness to the commercial SGL25AA to match the volume. As depicted in Figure 5-2, all fibrous samples demonstrate good reversibility by their oxidation and reduction current peaks.

The commercial SGL25AA presents the lowest oxidation and reduction current density peaks compared to electrospun samples. According to the past work from Yoon et al [183], the catalytic activity is enhanced by increasing the surface area of active site in electrodes. In other words, the lower surface area due to the larger fibers ( $d_f = 10 \mu\text{m}$ ) in SGL25AA led to poor activity. For more detailed observation, Brunauer-Emmett-Teller (BET) theory was applied to sorption isotherms to measure the actual specific surface area of each sample, as indicated in Table 5-1. Dynamic vapor sorption (DVS) (Surface Measurements Systems Ltd, P29F00061) was used with cyclohexane (Sigma Aldrich, ACS reagent, 99%) as an absorbate for measurement. As the table shows, SGL25AA has almost an order of magnitude less fiber surface area than the pristine electrospun sample per unit volume, which agrees with the lower activity seen during the cyclic voltammetry analysis.

The peak current densities of the reduction and oxidation reactions of the compressed electrode ( $12 \text{ mA/cm}^2$  and  $-9 \text{ mA/cm}^2$ ) were greater than the pristine one ( $10 \text{ mA/cm}^2$  and  $-8 \text{ mA/cm}^2$ ). It can be confirmed from Table 5-1 that the specific surface area was increased by 50% with compression during the stabilization process, which agrees with the qualitative assessment of the SEM images in Figure 5-1. Accordingly, the compressed electrospun sample achieved the highest oxidation and reduction current density peaks. Furthermore, the peak potential difference of the compressed electrode (380mV) was lower than the pristine one (440mV), indicating an improved reversibility for the vanadium  $\text{V}^{4+}/\text{V}^{5+}$  redox reaction.

***Table 5-1 - Specific surface area of electrospun fibrous samples***

<b>Sample</b>	<b>SSA (<math>\text{m}^2/\text{g}</math>)</b>	<b>SSA (<math>\text{m}^2/\text{m}^3</math>)</b>
---------------	---	---

<b>GDL25AA</b>	1.29	271015
<b>Pristine</b>	9.14	2000512
<b>Compressed</b>	7.66	3352383

- ❖ SSA: Specific surface area
- ❖ Sintered/laser (x): Sintered and laser perforated sample with x distance between holes

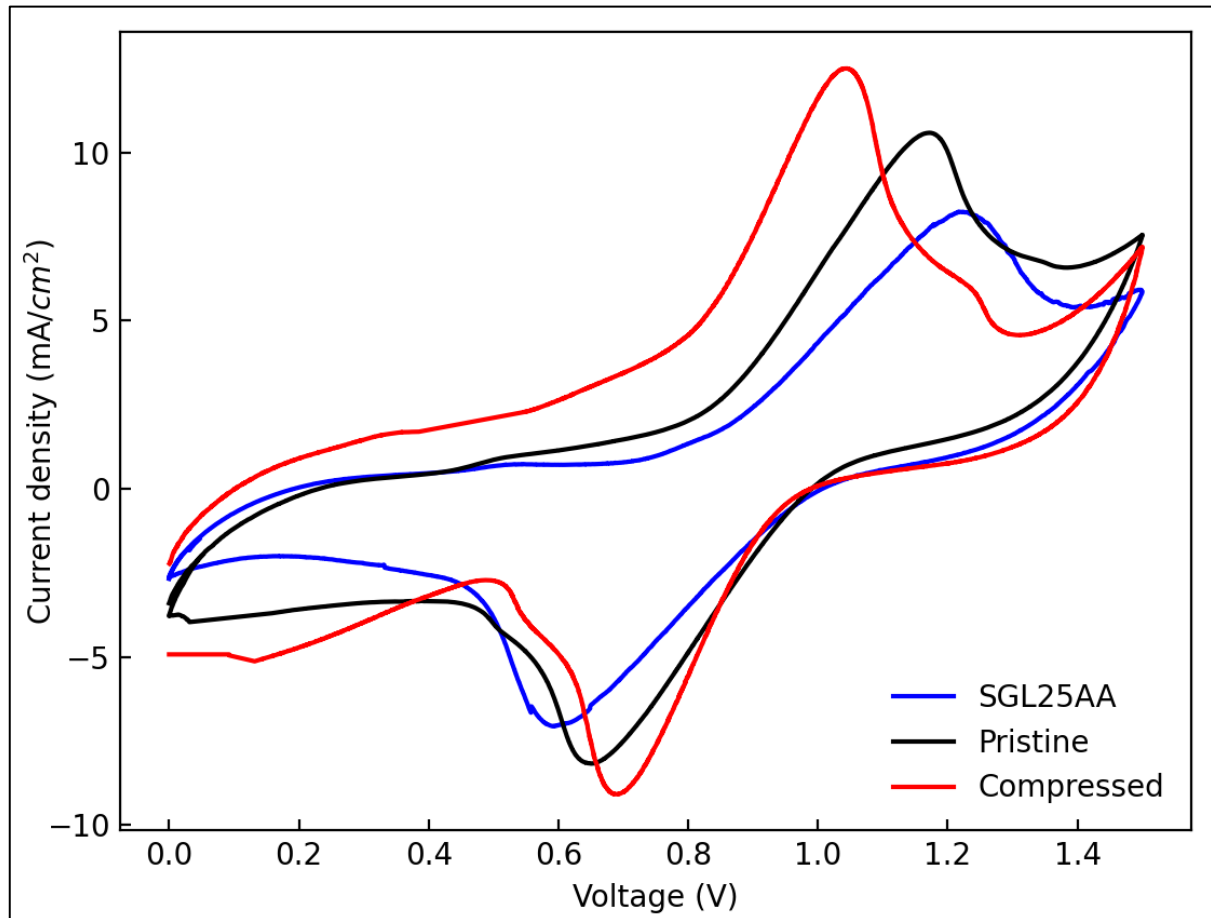


*Figure 5-2 – Cyclic voltammogram of SGL25AA, pristine, and compressed electrospun fibrous electrodes in terms of areal current density in 0.05M  $VOSO_4$  + 3.0M  $H_2SO_4$  electrolyte at a scan rate of 10mV/s*

### 5.3.3. Application of interdigitated flow design

#### 5.3.3.1. *Cell performance test*

The polarization behavior was tested as described in Chapter 3 but slightly different conditions. Electrode samples were cut into the size of 2.5×2.5 cm and applied at each side

of the cell. The cell voltage ranging from 0.6 to 1.45 V was considered to analyze the polarization behavior and the power density of a vanadium redox flow cell with each electrode, as indicated in Figure 5-3. For comparison to the previous results, all the samples discussed in Chapter 3 were tested here, though they were stacked together to provide the same thickness and domain volume as the other tests. These tests are referred to as “single layer” since they have a single type of material for all layers. The single layered samples performed similarly to the case in Chapter 3. The electrospun electrodes consistently display higher cell voltage over the entire range of current density compared to the commercial SGL25AA sample. However, the low through-plane transport, caused by the compacted fibers and indicated by the low through-plane permeability, hindered the transport of vanadium ions in the through-plane direction. As a result, mass transport loss occurred at the current density ranging from 125 to 200 mA/cm<sup>2</sup>, so the voltage was lower than the pristine sample. In practice, the maximum power density of the cell is roughly obtained at the current range where the mass transport polarization starts to occur, indicating the importance of the ion transport in electrodes, as shown in Figure 5-3. It was shown in Chapter 3 that the large artificial holes ( $d_f = 100 \mu\text{m}$ ) enhance through-plane permeability, so this may have promoted the flow of electrolyte to the region near the membrane where the majority of the reaction is occurring. In addition to that, in cases of pristine and compressed electrodes, the in-plane permeability was higher than the through-plane one, creating the dead-zone in the region of electrode below each channel path. In other words, the improved through-plane permeability of the electrode with the artificial holes therefore likely contributed to reducing this size of the dead-zone region; and consequently, a greater portion of the electrode could be supplied with vanadium ions.

**Table 5-2 - List of fibrous samples used at each layer type**

Layer type	Layer 1	Layer 2
A	SGL25AA	SGL25AA
B	Pristine	Pristine
C	Compressed	Compressed
D	Compressed/laser	Compressed/layer
E	SGL25AA	Compressed
F	Compressed	SGL25AA
G	Compressed	Pristine
H	Compressed	Compressed/Laser

Layer 1: Layer located beside a flow field

Layer 2: Layer located beside a nafion membrane

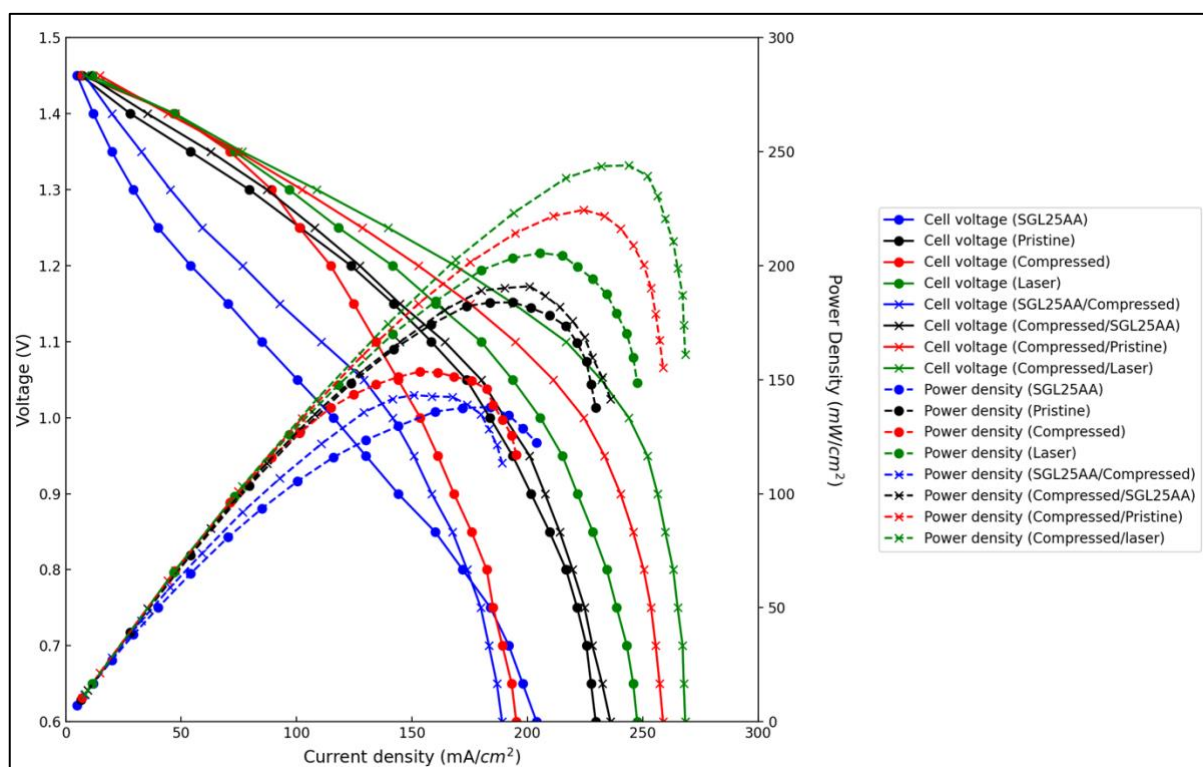


**Figure 5-3 - Polarization and gross power density curves at 100% state of charge with**

*interdigitated flow channel*

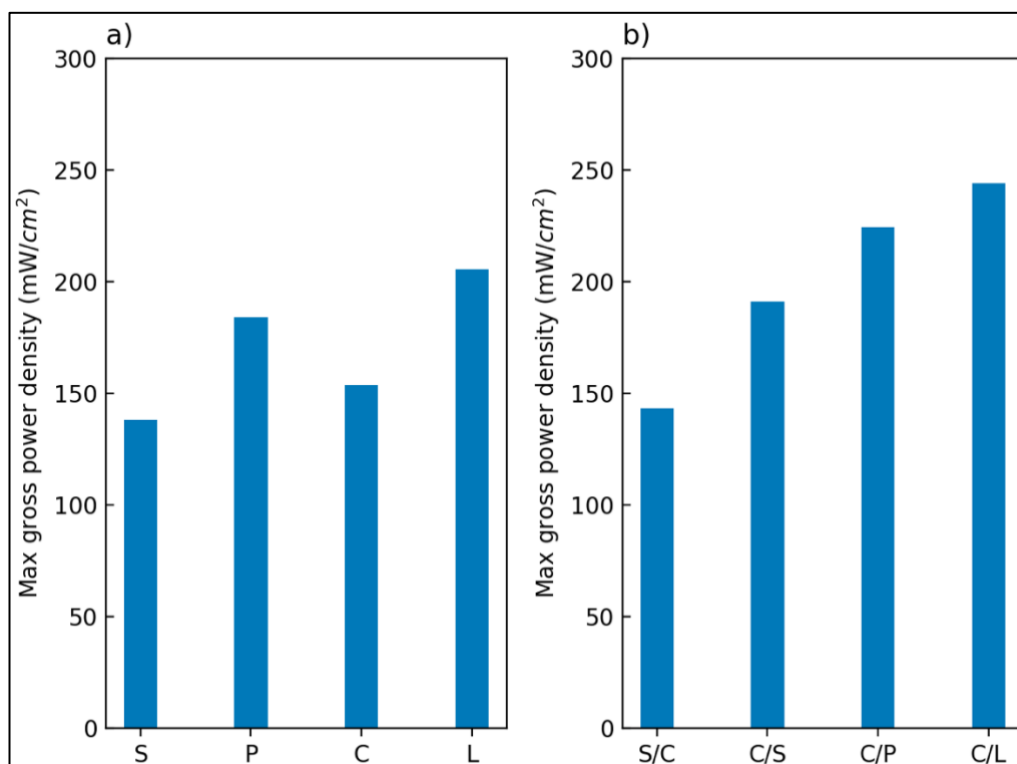
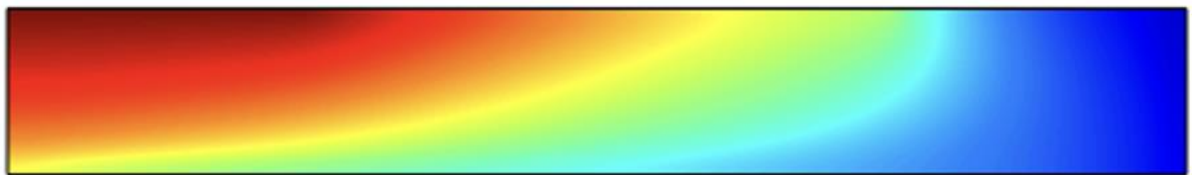


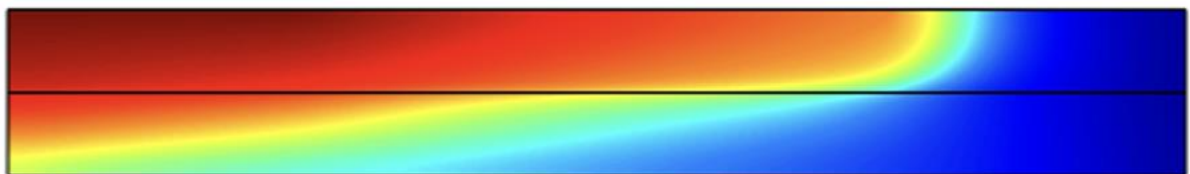
**Figure 5-4 – Maximum gross power density approached via interdigitated flow channel with different layer types of fibrous electrode S: SGL25AA, P: Pristine electrospun sample, C: Compressed electrospun sample, L: Compressed and laser perforated electrospun sample, X/Y: Double layer consist of X sample beside flow field and Y sample beside membrane.**

To help supporting this explanation, the simulation presented in the previous chapter was adapted to describe the present cell configuration. Note that the simulation was still based on a half-cell so direct quantitative comparison to the present experimental data is not possible, but the distribution of ions and reactions in the electrode are still qualitatively relevant and informative. Two different arrangements were considered for analysis here: placing a layer having a higher in-plane permeability either near the flow field or membrane. Figure 5-5a) shows the case of a “single” layer (corresponding to cases A, B and C in Table 5-2). The dead-zone can be seen on the right-hand side indicated by the blue region in colormap, meaning a depletion of reactant in that area. Figure 5-5b) shows the case with layer having the higher in-

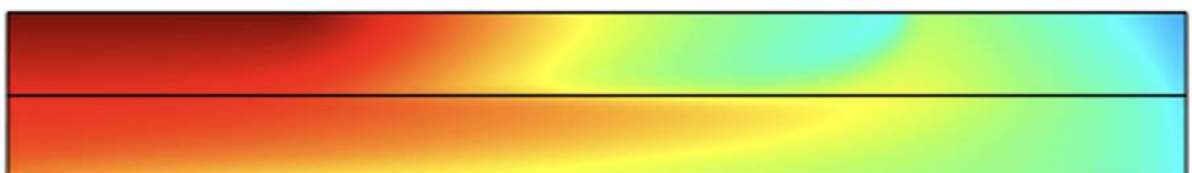
plane permeability layer beside a flow field (top). It can be confirmed that the ions prefer flowing through the layer beside the flow field rather than moving to the layer nearer the membrane. This means that the reactant is flowing predominantly in the layer furthest from the membrane, and that layer is largely underutilized. On the other hand, Figure 5-5c) shows the opposite arrangement with the layering near the membrane having a higher in-plane permeability, such that the electrolyte is forced to penetrate through the layer beside the flow field first, then flow laterally through the layer adjacent to the membrane. The concentration map in Figure 5-5c) clearly shows a more uniform distribution of reactant ions in both layers. Not only does this utilize more of the active area, but by shifting the reaction towards the membrane it reduces the transport length of protons emerging from the membrane.



a)



b)



c)



(Unit: mol/m<sup>3</sup>)

**Figure 5-5 – Distribution of  $VO_2^+$  ion in a) sample #1 and b) dual-layered fibrous electrodes built with layer 3 beside a rib and layer 2 beside a membrane in sample #3 on Table 4-2. C) is the case of dual layer which two layers are reversed**

### 5.3.3.2. Pumping cost

Although the improved cell performance with the novel fibrous structures, pumping cost is another parameter to be considered or incorporated in the analysis. While the electric power is generated, there is a cost associated with operating the flow cell, which is called pumping power. Pumping power is an important metric when evaluating the efficiency of flow cell operation and is calculated using Eq.2-2.

Because the flow-through electrode arrangement is essentially an application of Darcy's law for flow through a porous domain, we can re-cast the pumping cost equation given in Eq.2-2 in terms of the electrode's permeability coefficient. According to Darcy's law in Eq.2-1, the volumetric flow rate of electrolyte and pressure drop are linearly correlated with the permeability coefficient, and also proportional to the area through which flow occurs and the length of the electrode. Inserting the expression for pumping power as a function of pressure drop (Eq.4-30) into Darcy's law (Eq.2-1) yields the following:

$$P_{pump} = \frac{KA}{\mu L \varphi} \Delta P^2 \quad 5-1$$

where  $\varphi$  is the pump efficiency (generally assumed to be 100% here). This expression for the pumping power works for a true "flow-through" system but is not quite correct for an interdigitated configuration due to the different flow inlet and outlet locations; however, it is still a useful expression that allows us to qualitatively understand the relationship between pumping power and the permeability of the electrode material.

Figure 5-6 shows the pumping power vs flow rate and applied pressure for all the

electrode arrangements produced in this work. The commercial SGL25AA had a superior high overall permeability due to the much larger pores compared to electrospun samples, resulting in the lowest pumping power as can be confirmed in Figure 5-6. The compressed electrospun sample required slightly higher pumping power than the pristine one despite their identical in-plane permeability confirmed by Lee et al [138]. The lower through-plane permeability caused by concentrated and compacted fibers required relatively the higher convective force to make the electrolyte transport into the pores among fibers. In other words, higher pressure drop was required to provide an identical flow rate of electrolyte. On the other hand, this flaw could be significantly reduced with the artificial holes created by  $\text{CO}_2$  laser perforation due to the extra pores created.

Moreover, in cases of both pristine and compressed samples, the in-plane permeability was higher than the through-plane one, leading to the vanadium ions flowing straightly from inlet to outlet boundary at in-plane direction as soon as invading into the electrode, as discussed with simulation in Figure 5-5. The improved through-plane permeability with laser perforation could induce electrolytes to flow down to the nafion membrane boundary first and start flowing in the in-plane direction afterward. Hence, the lower pumping power was required although comparatively longer travel length than the cases with pristine and compressed samples. However, despite those gains, the pumping power was still higher than the case with SGL25AA. It would be the next challenge to finding out the advanced technique for further reduction while maintaining the consistent volumetric fiber surface area.

For multi-layered structure with type E, there was no significant difference in pressure drop to provide identical electrolyte flow rate compared to the case of single layer (Type A). This supports the picture that the electrolyte flow bypasses the compressed sample due to the low permeability compared to layer 1. In other words, the fibers at layer 2 were not utilized

properly for reaction to provide current. On the other hand, when layers 1 and 2 are reversed in type F, the electrolyte needs to permeate through the compressed electrospun layer first to reach the next layer containing SGL25AA. Furthermore, the layer 1 beside a flow channel path acts as a barrier and prevents ions exiting through the outlet boundary until layer 2 is completely saturated and pressurized enough to permeate back to layer 1 and exit through outlet boundary. Consequently, the system required comparatively the higher overall pressure drop. When layer 2 was replaced with pristine electrospun sample in Type G, a higher pressure drop was required due to the decreased overall permeability. However, a reduction in pressure drop was observed with Type H containing compressed and laser perforated electrospun sample at layer 2 due to enormously increased overall through-plane permeability.

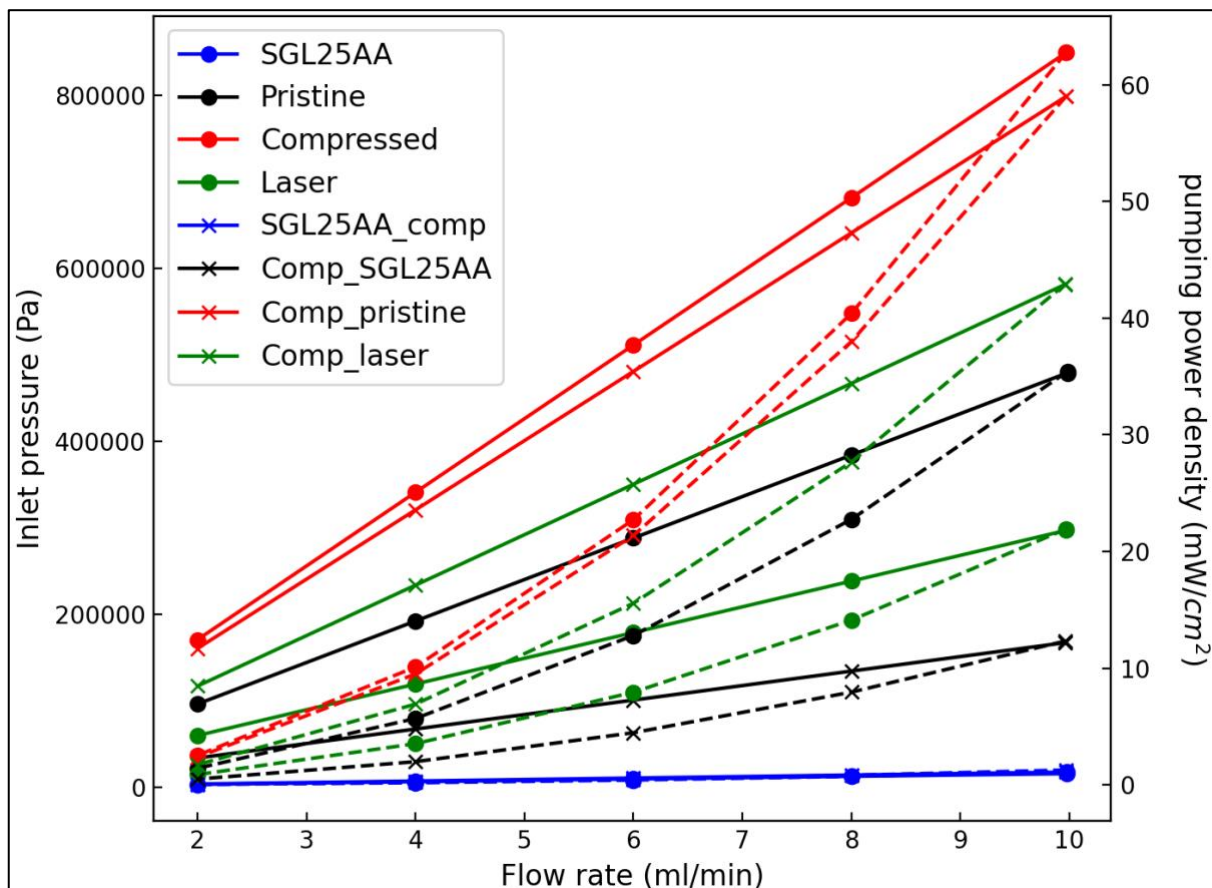


**Figure 5-6 – Inlet pressure and pumping power density required with each layer type of fibrous electrode to provide electrolyte flow rates when assembled with interdigitated flow channel**

### 5.3.3.3. *Net performance*

In practice, it is important to make a balance between gross power density provided from the cell and pumping power required for operation to evaluate the overall performance. The net power density of cell with each electrode sample was calculated using Eq.2-14.

As can be confirmed in Figure 5-7a), although the higher pumping power density, the pristine electrospun still showed improvement on overall net power density compared to the commercial SGL25AA. However, much higher pumping power with low through plane permeability of compressed electrospun sample resulted in a substantial loss of net power density, resulting in worse performance than commercial SGL25AA. On the other hand, the enormous improvement in permeability with laser perforation induced much lower pumping power, so the highest net power density could be achieved compared to other single layered electrodes. The electrodes built in multi-layered structures in Figure 5-7b) generally shows improvement in net power density. The layer type E shows the lowest net power density although the lowest pumping power is required to operate the cell due to extremely low gross power density. Interestingly, layer type G showed the worst net power density than type F although the higher overall fiber surface for reaction due to the significantly much higher pumping power. However, the highest overall fiber surface area with sufficient permeability could be approached by replacing layer 2 beside membrane with compressed and laser perforated electrospun sample, rendering the optimal net power density among all layer types.

In addition, it is important to make a balance between gross and pumping power density to optimize the operating efficiency of flow cell. The efficiency was found from:

$$\eta_{net} = \frac{V_{cell}i_{cell}A_{elec} - P_{pump}}{V_{cell}i_{cell}A_{cell}} \quad 5-2$$

where  $\eta_{net}$  is the net efficiency of cell operation,  $V_{cell}$  is the cell voltage,  $i_{cell}$  is the current density provided, and  $A_{cell}$  is the geometric area of electrode. In practice, the operating efficiency was mostly dependent on pumping power required to operate the cell. As can be seen in Figure 5-8, the efficiency with SGL25AA approaches almost 100% since the magnitude of pumping power is quite negligible due to extremely high overall permeability. On the other hand, the pristine electrospun sample shows relatively the lower efficiency, indicating the inverse correlation between efficiency and fiber size. The further reduction was observed with compressed electrospun sample, but the laser perforation successfully overcame the flaw.

In the case of multi-layered structure in Figure 5-8b), it can be observed by comparing electrode types E and F that the efficiency is better with the electrode having a higher permeability at layer 1 than layer 2. This is attributed to the fact that most of the electrolyte transports through large pores among fibers in layer 1, which caused extremely low pumping power. Specifically, the degree of improvement in gross power density was lower than the pumping power when reversing layer 1 and 2, leading to the lower operating efficiency with electrode type F.

For types F, G, and H, which are the cases with layer 1 having lower permeability than layer 2, the efficiency was correlated with the permeability at layer 2. The electrode type F had the highest efficiency due to lowest pumping power density induced with high permeability of SGL25AA at layer 2. Similarly, the electrode type H containing the laser perforated sample could approach relatively higher efficiency than type G with improved permeability.

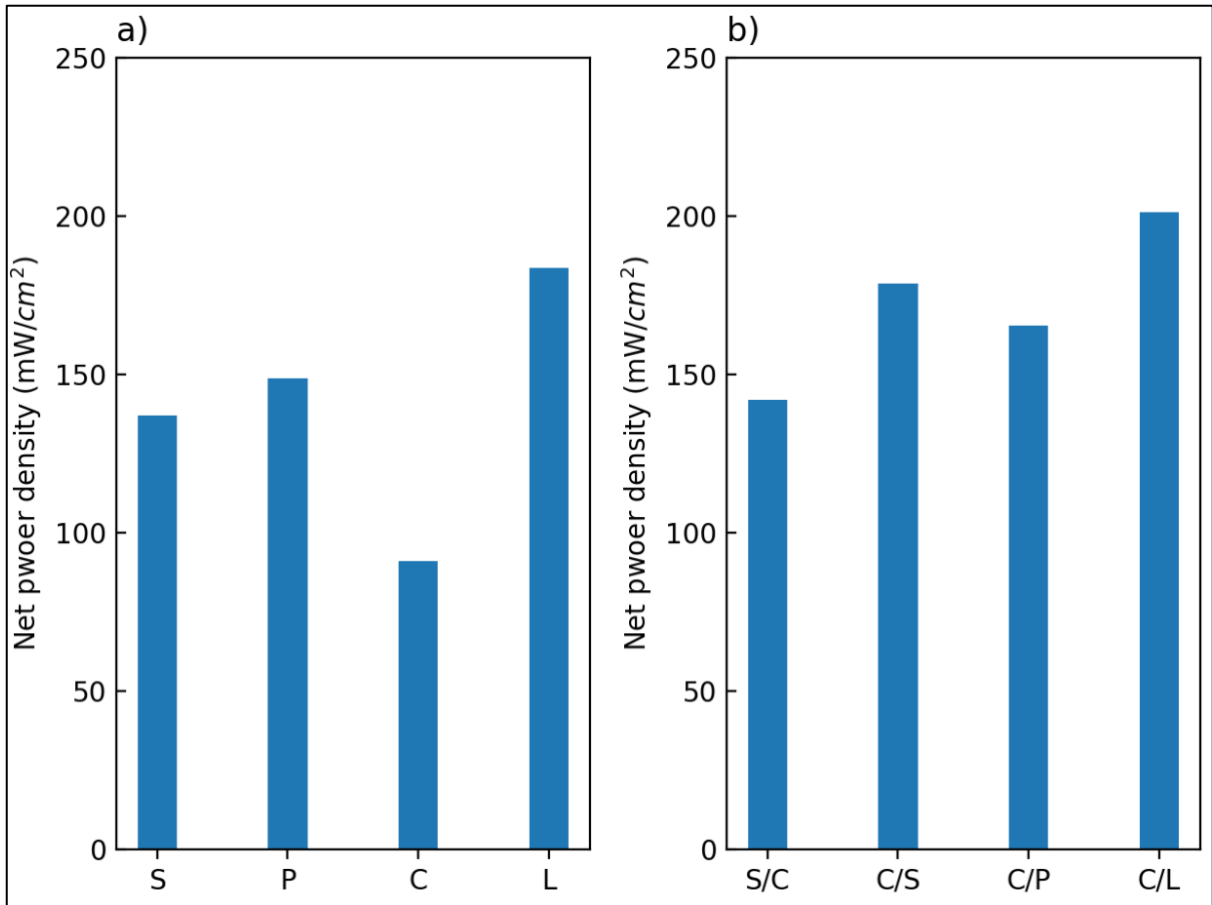


**Figure 5-7 – Net power density approached via interdigitated flow channel with different layer types of fibrous electrodes. S: SGL25AA, P: Pristine electrospun sample, C: Compressed electrospun sample, L: Compressed and laser perforated electrospun sample, X/Y: Double layer consist of X sample beside flow field and Y sample beside membrane**

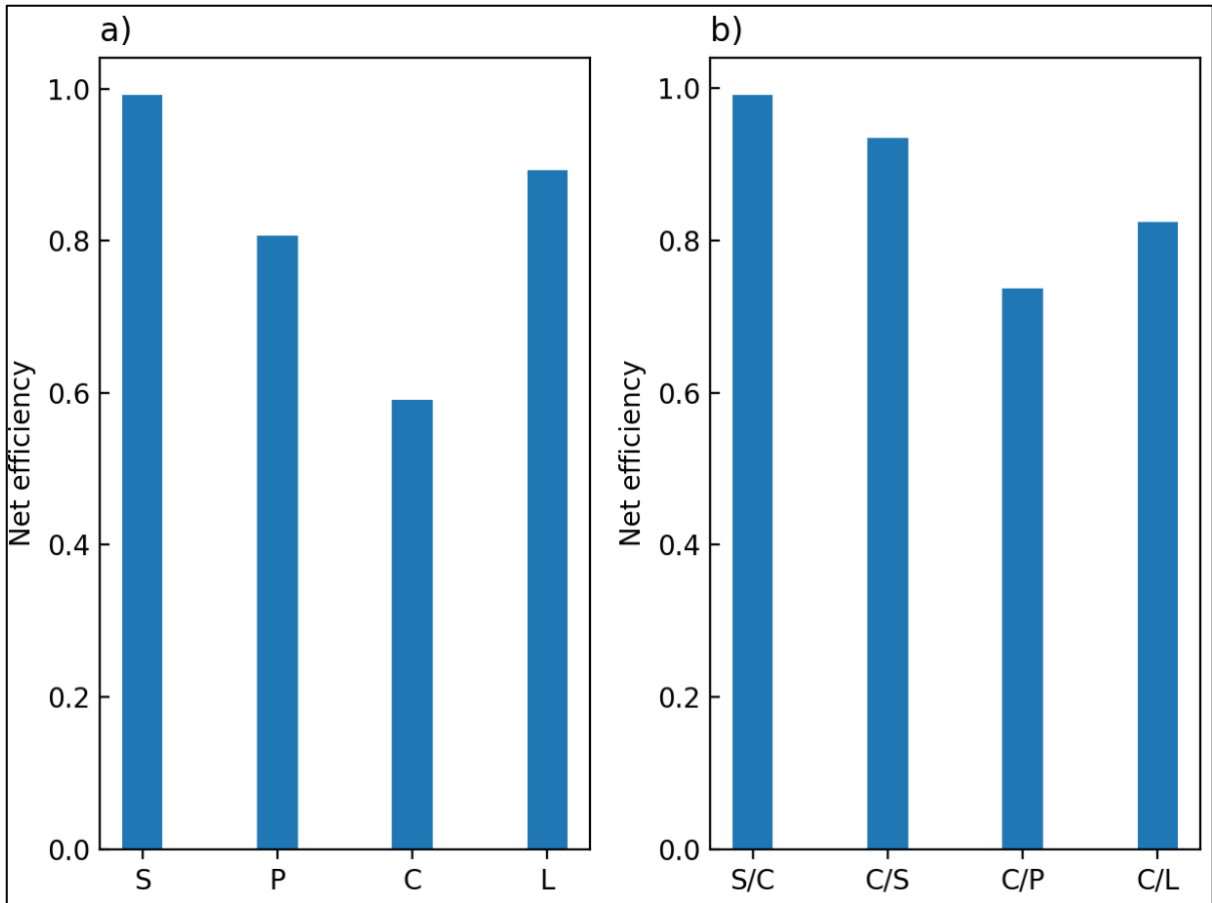


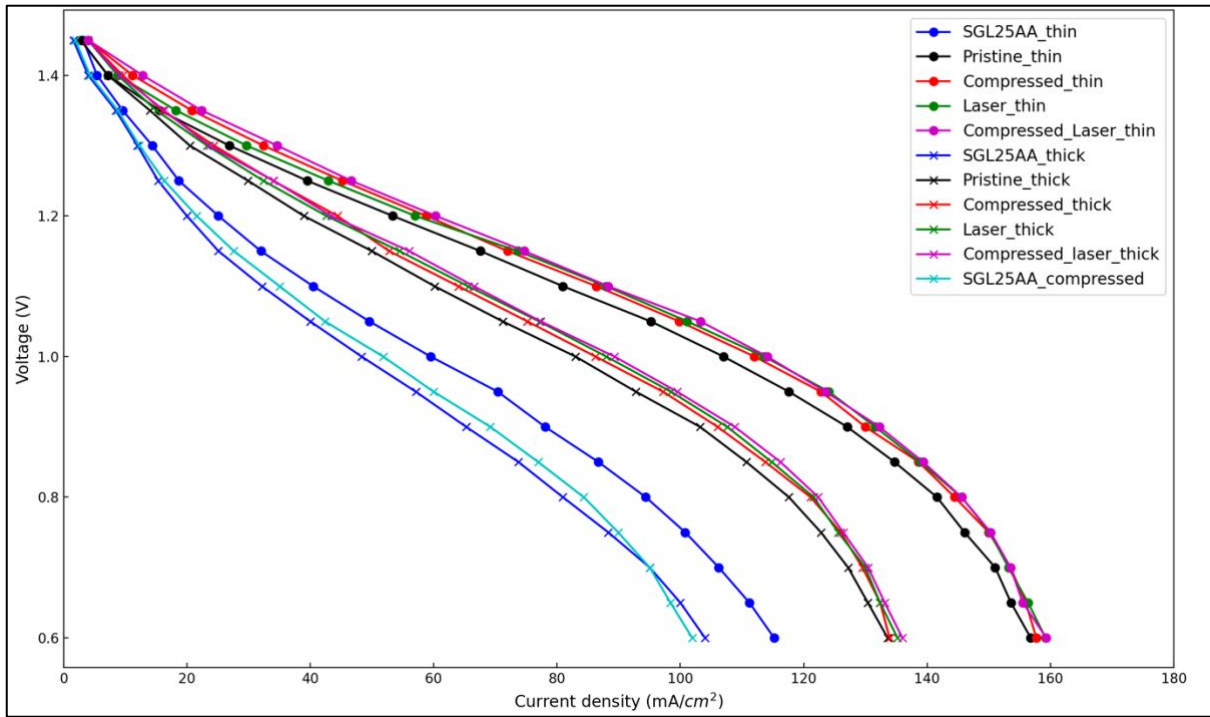
**Figure 5-8 – Net operating efficiency of redox flow cell with different layer types of fibrous electrode when assembled with interdigitated flow channel**

#### 5.3.4. Application of parallel channel design

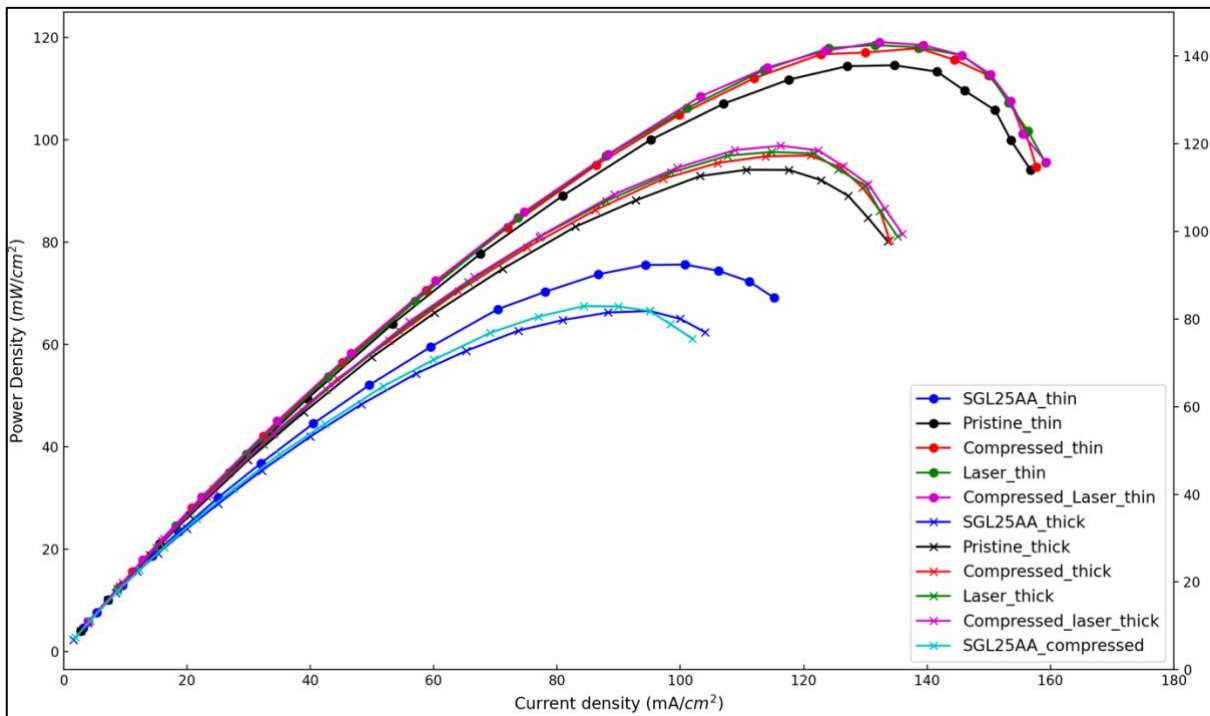
##### 5.3.4.1. *Cell performance*

It was confirmed from the previous section that electrospun samples in general provided higher power density compared to commercial SGL25AA. However, the net performance was relatively lower due to the high pumping power incurred by the low permeability. In practice, using convective flow will always tend to provide low operating efficiency because of the high pumping power required. In this section, the alternative “flow-by” mode was tested using a parallel flow field design, which relies on passive mass transfer into the porous electrode via diffusion. The aim was to confirm if the overall performance is better when accounting for the alleviated pumping power. Figure 5-9 shows that the

commercial SGL25AA still shows the worst polarization behavior compared to other electrospun fibrous samples. In the case of this flow-by mode, the transport of vanadium ions completely relies on diffusion because of no convective force applied. Because diffusion is slower than convection, most reaction will occur near the interface between flow field and electrode. The electrospun samples still provided better performance attributed to the greater fiber surfaces exposed to that interface with smaller fiber size. Furthermore, the proton transport was not significantly affected by structures of SGL25AA and electrospun sample because of their low tortuosity with high porosity ( $\sim 0.9$ ). Thus, in all cases the protons had fairly low resistance when transferring from the membrane to the reactive zone. In the case of compressed electrospun fibrous electrode, the higher fiber surface area at the interface induced further improvement on cell performance. Since most of the reaction is occurring at the flow channel-electrode interface, the structural properties of porous electrode did not significantly change any polarization behavior. As Figure 5-9 and Figure 5-10 demonstrate, no appreciable improvement could be observed with multi-layered structure.



a)



b)

**Figure 5-9- a) Polarization and b) gross power density curves at 100% state of charge with parallel flow channel. X\_Y\_(thin or thick): X sample beside flow field and Y sample beside membrane with the overall thickness of (thin: 170  $\mu\text{m}$ , thick: 340  $\mu\text{m}$ )**

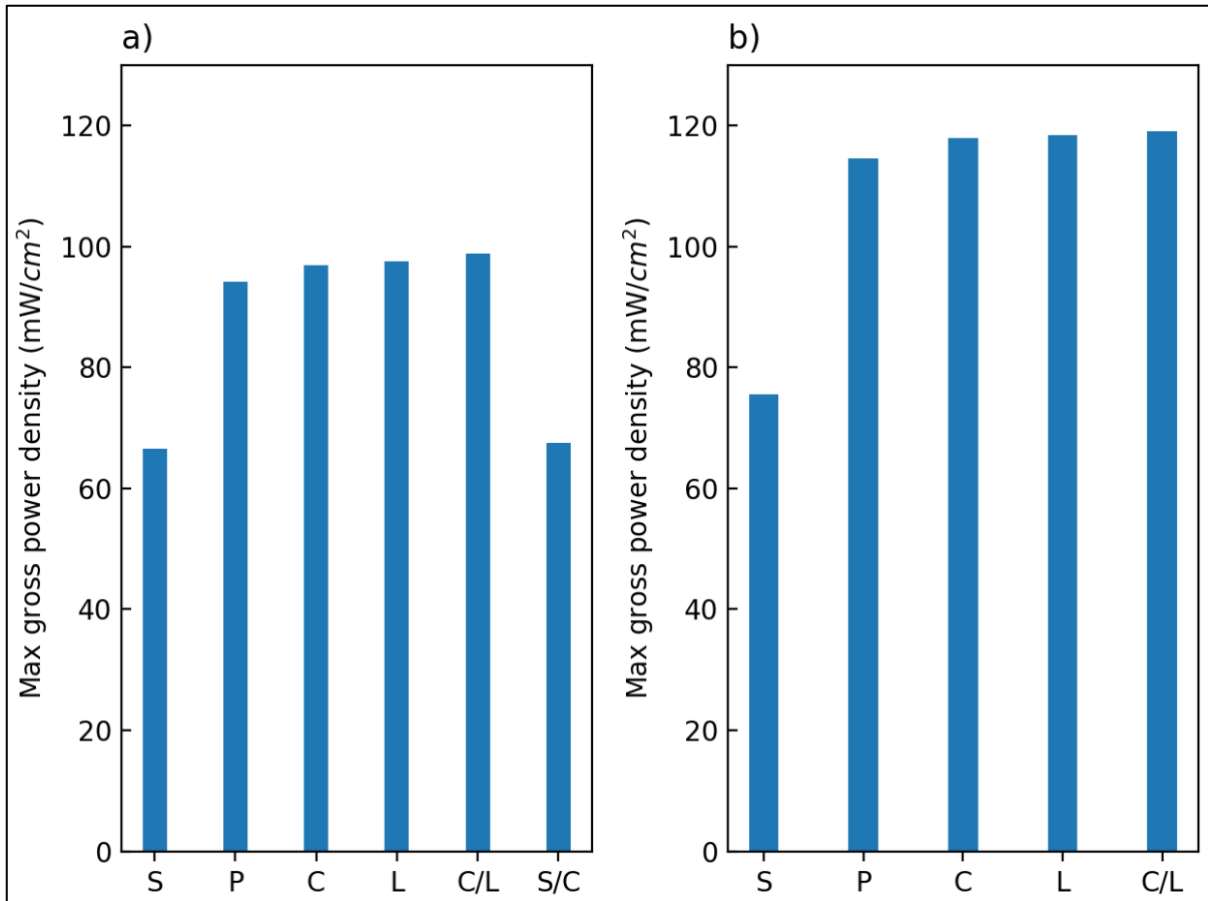


**Figure 5-10 - Maximum gross power density approached via parallel flow channel with different layer types of fibrous electrode at the overall thicknesses of a) 340  $\mu\text{m}$  and b) 170  $\mu\text{m}$**

#### 5.3.4.2. Pumping cost

The required pumping power with flow-by mode was independent to the structure of fibrous electrode, as depicted in Figure 5-11. As discussed earlier, the liquid electrolyte is not compelled to transport into small pores among fiber in electrodes, and ions only transport via diffusion. In other words, the pressure required for electrolyte transport depends only on the geometrical size and design of the parallel flow channel used. In practice, the magnitude of pumping power applied was much lower than the case with interdigitated flow channels. For instance, the highest pumping power was observed with compressed electrospun sample in Figure 5-6, but the power could be reduced by 98% with parallel flow field as shown in Figure

5-11. In practice, the pumping power with compressed sample was quite similar to other samples since identical flow field was used.

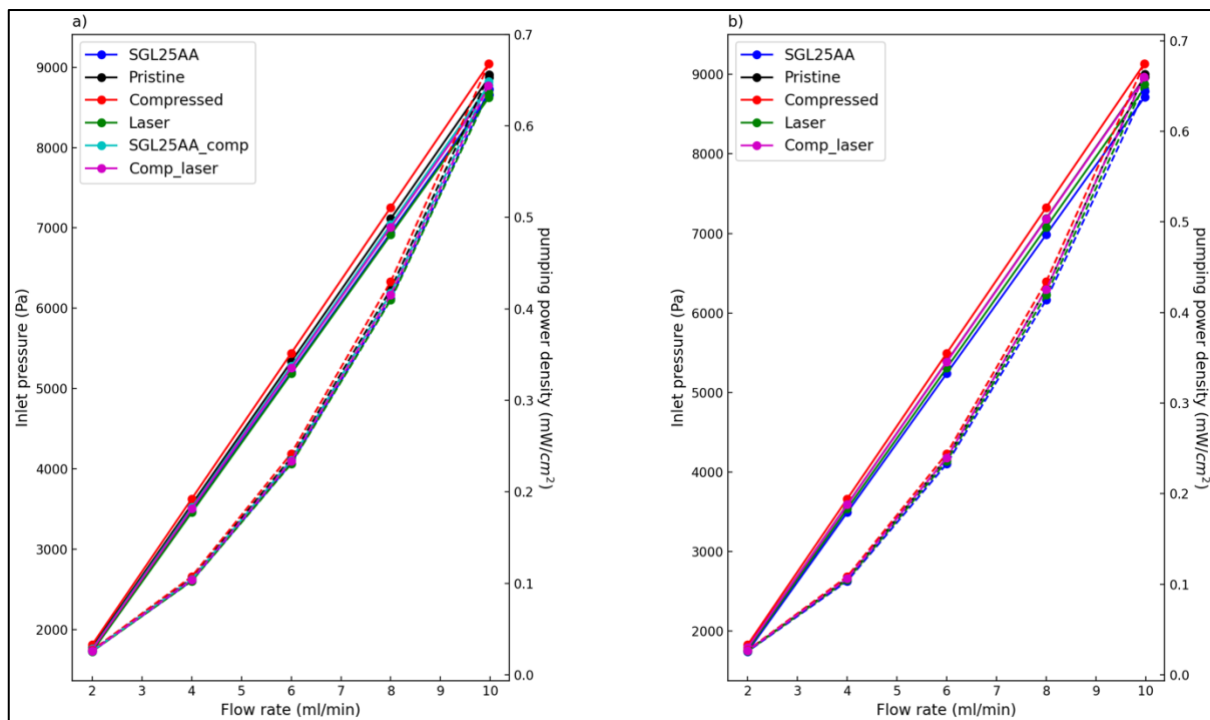


**Figure 5-11 – Inlet pressure and pumping power density required with each layer type of fibrous electrode at the overall thicknesses of a) 340 μm and b) 170 μm to provide electrolyte flow rates when assembled with parallel flow channel**

### 5.3.4.3. Net performance

Unlike the case of interdigitated flow channel, the gross and net power densities are almost identical to each other with parallel flow design, as can be compared in Figure 5-10 and Figure 5-12. In fact, it can be realized from Figure 5-6 and Figure 5-11 that the magnitude of required pumping power to operate the cell with parallel flow channel design is quite small and negligible for all electrode types compared to the case with interdigitated one, and thus does not significantly impact on the operating efficiency. As a result, the operating efficiency was maintained at 100% for all electrode types, shown in Figure 5-13. Consequently, it can be concluded that the structure of fibrous electrode never affects the required pumping power with flow channel designed as flow-by mode, leading to almost perfect operating efficiency

unless channel path is designed to extremely long length. However, although extremely low pumping power, the net power density was lower than the case with interdigitated flow channel for all electrode types, which validates the importance of fiber surface area being utilized for reaction to optimize the performance.

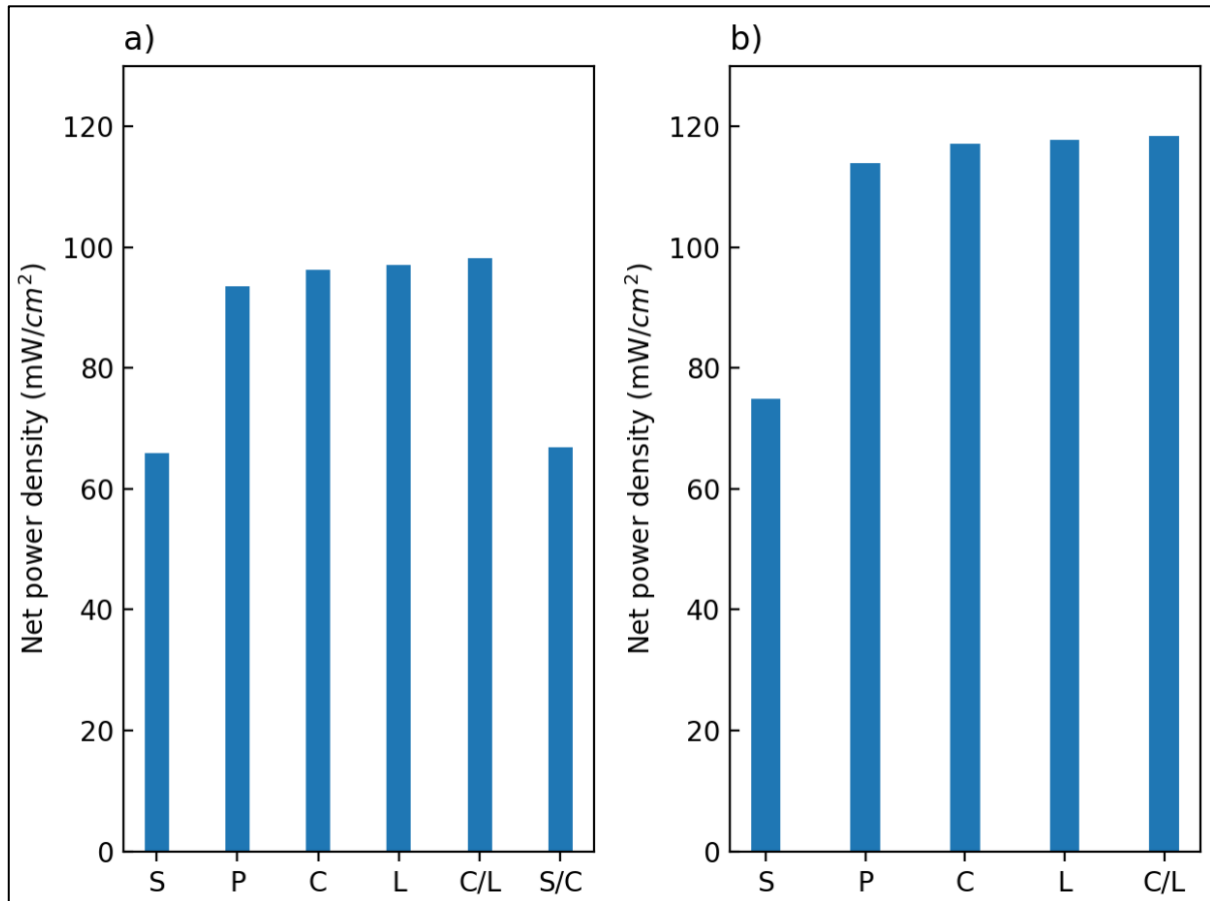


**Figure 5-12 - Net power density approached via parallel flow channel with different layer types of fibrous electrodes at the overall thicknesses of a) 340 μm and b) 170 μm**

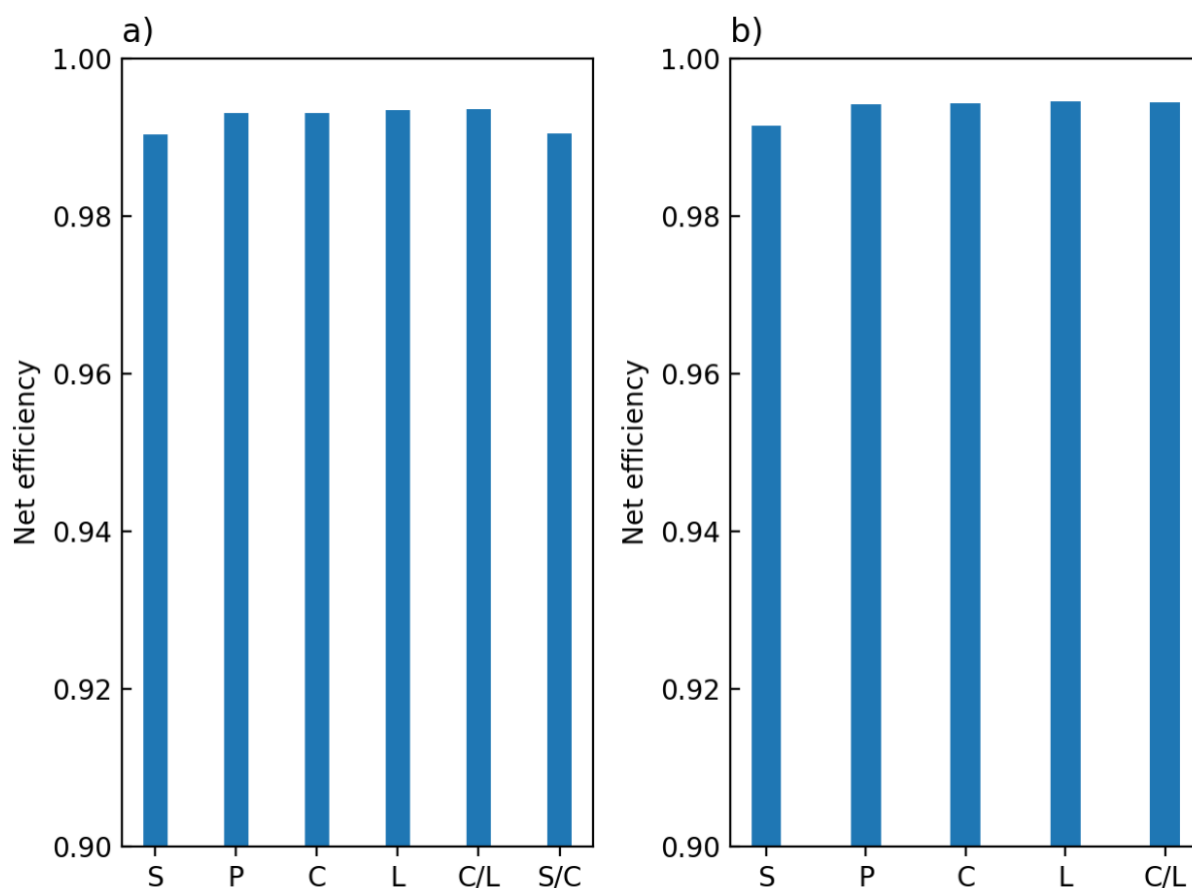


**Figure 5-13 - Net operating efficiency of redox flow cell with different layer types of fibrous electrode at the overall thicknesses of a) 340 μm and b) 170 μm when assembled with parallel flow channel**

#### 5.3.4.4. Electrode thickness

As discussed in previous sessions, not only the electrochemical reaction rate on carbonized fiber surface, but also the transport of proton acts as an important role for cell performance. The performance of redox flow cell with parallel flow field was evaluated at different thickness of fibrous electrode to test this, as shown in Figure 5-9. Overall, all samples provide comparatively better performance with thinner electrodes. Since the active species only transfers into electrodes via diffusion, most electrical reaction occurs at the region closed to the interface between electrode and flow field. This means that the protons must travel the entire thickness of the electrode to reach the reactive zone, leading to appreciable ohmic loss. This flaw becomes worse as the thickness of electrode increases due to the longer

distance between channel path and membrane. Future work should investigate the lower limit on electrode thickness to harness this effect. Thinner electrodes are not physically robust so could become difficult to work with. Also, the actual depth of the reactive zone is not known, so some additional modeling studies would provide useful guidance in this regard.

#### **5.4. Conclusion**

This study presents a way of inducing a more uniform ion distribution by using multi-layered structure of electrodes built with novel electrospun fibrous layers thereby improving the cell performance in almost all categories. Both cell power and pumping power were observed to evaluate the actual performance of the operating cell. The cell with interdigitated flow channels provided the highest net power density despite a non-negligible pumping cost. When the layer beside flow channel had a low in-plane permeability it essentially forced the electrolyte to flow through the layer nearest the membrane, thus utilizing more of the electrode. As a result, the gross power density was increased by 17% with the best multi-layered structure compared to the single layer containing only compressed and laser perforated electrospun electrode. A higher pumping power was required due to the lower permeability of the layer beside flow channel, but the magnitude was small compared to the degree of improvement in gross power density. Thus, there was still an improvement in net power density.

Even though the net power density was improved, the pumping cost was still appreciable, so the performance of the custom electrodes was analyzed using parallel flow channels as well. The multi-layered electrode design provided no benefit when parallel flow channels were used since the transport of active electrolyte species relied totally on diffusion,

so only the fibers located at the boundary between the electrode and flow channels were utilized. It was observed that thicker electrodes hindered the proton to transport by increasing the transport length between the membrane and the reactive zone, lead to a noticeable increase in ohmic polarization. Overall, this work illustrates the importance of arranging fibrous structures as well as flow channel design to induce uniform ion distribution and optimize the power density of redox flow cell.

## 6. Conclusions and Future Work

The main goal of this thesis was to modify the structure of fibrous electrode in a vanadium redox flow battery to improve the net power density. The two parallel objectives of this work were to increase the gross power density obtained from a flow cell while simultaneously reducing the pumping cost. The net power density of the flow cell was therefore analyzed in detail by measuring polarization performance as well as pressure drop, which is very rarely reported together in the literature. This work therefore presents a novel electrode architecture which provides an impressive increase in power density, while also critically analyzing the tradeoffs associated with the design.

### 6.1. Summary and Conclusion

In chapter 3, the performance of vanadium redox flow battery with modified electrospun fibrous electrode was examined in various aspects. A polymer solution containing 12 wt% PAN dissolved in N,N-dimethylformamide (DMF) was electrospun to fabricate fibrous electrodes. The electrospun material was compressed to the half its original thickness during stabilization and carbonization process to densify fibers and increase the volumetric specific surface area and therefor active site density. As a result, in-plane permeability was maintained while decreasing the porosity. A positive side effect of this process was an improvement in the electrical conductivity of the materials due to better interconnections between fibers created via compression. A negative effect was that the compacted fibers possessed lower through-plane permeability. The flaw was overcome by create artificial hole via  $CO_2$  laser perforation. A portion of the fiber surface area was lost with  $CO_2$  laser perforation but the influence was quite negligible compared to the degree of increase in through-plane permeability. Consequently, the vanadium ion could be uniformly distributed over the entire region of

fibrous electrode, leading to the much improved power density.

In chapter 4, multi-layered structures of fibrous electrode were considered via simulation with COMSOL Multiphysics software. Each layer in the electrode domain had different values of Carman-Kozeny constants, fiber size, and porosity. Structures were considered which had permeability gradients between layers so that uniform vanadium ion distribution can be induced over the entire region of electrode domain. The best performance was found when the layer beside the flow channel contained the lowest in-plane permeability while the one beside a membrane had the highest permeability. This arrangement forced the electrolyte through the layer near the membrane, helping to ensure that vanadium ions were more uniformly distributed to the entire domain. The performance of multi-layered structure was evaluated at different inlet concentration of reactant and flow rate electrolyte. The trend of change in polarization behavior as well as limiting current density was perfectly correlated to inlet concentration, but relatively the less improvement was observed at higher electrolyte flow rate. This was attributed to the fact that the mass transport between bulk and fiber surface tends to weaken at a higher velocity of the electrolyte due to the sub-linear nature of the mass transfer correlation, leading to relatively lower surface concentration of ions. The operating efficiency of multi-layered structure was comparatively lower than single layer since the higher pumping power was required to overcome low permeability of the layer beside flow channel path. However, the efficiency approached over 99% at high flow rate of electrolyte (10 ml/min) and inlet concentration ( $1000 \text{ mol/m}^3$ ), which validates negligible pumping power required for operation compared to the gross power generated from the redox flow cell.

In chapter 5, the performance of vanadium redox flow battery with multi-layered fibrous electrode built with commercial carbon felt and novel electrospun fibrous structures. The electrode was built in double layer for simple experimental approach. First, uniform ion distribution could be induced when the layer beside membrane had the higher permeability. In the case when two layers were reversed, the liquid electrolyte only transports through the layer beside flow channel due to the difference in permeability, meaning the fibers in the next layer could not be utilized properly for reaction. Also, making a balance between permeability and the surface area of active site for reaction acted as an important role to optimize the performance. When the commercial sample, SGL25AA, was used in the layer beside a membrane to induce larger permeability difference between layers, net power density was even lower than the case of single layer due to the reduced overall fiber surface area of active site reduced. In practice, the multi-layered electrode was effective with the interdigitated flow channel, but inefficient with parallel flow channel since vanadium ions only transport via diffusion and thus do not permeate deeply into the space beside the electrode. Because of that, the interdigitated flow channel always provided the better net performance although the higher pumping power required to operate the system.

## **6.2. Suggestions for Future Works**

### **6.2.1. Analysis in the size and concentration of artificial holes**

In the project described in Chapter 3, the polarization behavior could be improved further by inducing the uniform ion distribution over the entire region of electrode on top of the compressed and laser perforated sample. The fibrous electrode had permeabilities in two different directions: in-plane and through-plane. Since through-plane permeability was

excessively increased to even much higher than in-plane permeability with large artificial holes created via  $CO_2$  laser perforation ( $d_p = 100 \mu\text{m}$ ), it is suspected that the fibers located at the portion below outlet boundary was not saturated sufficiently with vanadium ion. There might be the possibility of further improvement on power density by solving this issue. Thus, it is recommended to find out the way of approaching the smaller size of artificial holes to remediate through-plane permeability. The new challenge would be to make a balance again between fiber surface area and permeability in terms of the hole size to optimize the performance.

#### 6.2.2. Development of time-dependent model in COMSOL Multiphysics

In chapter 4, the model built in COMSOL Multiphysics was built in stationary condition. The model was independent of time, and thus the reactant was introduced in the electrode domain at a consistent state of charge. In the real case of a vanadium redox flow battery, the electrolytes are stored in a separate tank, and the concentration of reactant inside the tank continuously reduces as time passes due to electrochemical reaction between vanadium ion and carbonized fiber surface in electrodes. Thus, it would be recommended to consider remodeling the simulation in transient mode to improve accuracy.

#### 6.2.3. Development of meso-pores on fiber surface

All the projects introduced in this thesis focused entirely on the way of arranging fibrous structure in electrodes to increase specific surface area of fiber. As discussed, some parameters needed to be sacrificed to improve other parameters. For instance, the through-

plane permeability was increased with the artificial holes created via  $CO_2$  laser perforation, but the portion of fibers in electrodes needed to be burnt out. There would be the possibility of further improvement without any sacrifice by creating meso-pores on top of fiber surface. In that case, not only the higher specific surface area of active site for reaction, but also the higher porosity with extra meso-pores would increase the permeability of electrode, which results in lower pumping power to operate the redox flow cell. It would be a challenge to find the appropriate component of polymer solution to be used for the electrospinning process to approach this goal.

#### 6.2.4. Analysis in component of liquid electrolyte

Both cell performance and pumping power are affected by not only the structure of electrode but also the property of liquid electrolyte. For instance, three different components are in general used to manufacture the liquid electrolyte for a vanadium redox flow battery: vanadium power, sulfuric acid, and water. Among them, sulfuric acid is utilized as a supporting composition to dissolve vanadium powder. Thus, higher wt% of sulfuric acid needs to be considered to make electrolytes containing more densified vanadium ion. In practice the highly densified vanadium ion in the electrolyte will induce higher gross power density. However, the viscosity of electrolyte will increase simultaneously, which would require higher pumping power to operate the cell. By making an overall balance between gross and pumping power density with novel fibrous electrode introduced in this thesis and the electrolytes with optimal component, the redox flow cell would be able to be improved further.

## References

1. Weisser, D. (2007). A guide to life-cycle greenhouse gas (GHG) emissions from electric supply technologies. *Energy*, 32(9), 1543-1559.
2. Barthelmie, R. J., & Pryor, S. C. (2014). Potential contribution of wind energy to climate change mitigation. *Nature Climate Change*, 4(8), 684-688.
3. Braff, W. A., Mueller, J. M., & Trancik, J. E. (2016). Value of storage technologies for wind and solar energy. *Nature Climate Change*, 6(10), 964-969.
4. Mitali, J., Dhinakaran, S., & Mohamad, A. A. (2022). Energy storage systems: A review. *Energy Storage and Saving*.
5. Eze, V. H. U., Edozie, E., Kalyankolo, U., Okafor, O., Ugwu, C. N., & Ogenyi, F. C. (2023). Overview of renewable energy power generation and conversion (2015-2023).
6. Bagher, A. M., Vahid, M., Mohsen, M., & Parvin, D. (2015). Hydroelectric energy advantages and disadvantages. *American Journal of Energy Science*, 2(2), 17-20.
7. Kim, K. J., Park, M. S., Kim, Y. J., Kim, J. H., Dou, S. X., & Skyllas-Kazacos, M. (2015). A technology review of electrodes and reaction mechanisms in vanadium redox flow batteries. *Journal of materials chemistry a*, 3(33), 16913-16933.
8. Ulaganathan, M., Aravindan, V., Yan, Q., Madhavi, S., Skyllas-Kazacos, M., & Lim, T. M. (2016). Recent Advancements in All-Vanadium Redox Flow Batteries. *Advanced Materials Interfaces*, 3(1). <https://doi.org/10.1002/admi.201500309>
9. Darling, R. M., Gallagher, K. G., Kowalski, J. A., Ha, S., & Brushett, F. R. (2014). Pathways to low-cost electrochemical energy storage: a comparison of aqueous and nonaqueous flow batteries. *Energy & Environmental Science*, 7(11), 3459-3477.
10. Ralon, P., Taylor, M., Ilas, A., Diaz-Bone, H., & Kairies, K. (2017). Electricity storage and renewables: Costs and markets to 2030. *International Renewable Energy Agency: Abu Dhabi, United Arab Emirates*, 164.
11. Yang, H., Zhang, S., Chen, B., Xiang, S., Xu, Y., Yin, B., & Ackom, E. (2023). The battery storage management and its control strategies for power system with photovoltaic generation. In *Emerging Trends in Energy Storage Systems and Industrial Applications* (pp. 441-484). Academic Press.
12. Wagner, L. (2007). Overview of energy storage methods. *Analyst*.
13. Leung, P., Li, X., De León, C. P., Berlouis, L., Low, C. J., & Walsh, F. C. (2012). Progress in redox flow batteries, remaining challenges and their applications in energy storage. *Rsc Advances*, 2(27), 10125-10156.
14. Skyllas-Kazacos, M., Chakrabarti, M. H., Hajimolana, S. A., Mjalli, F. S., & Saleem, M. (2011). Progress in flow battery research and development. *Journal of the electrochemical society*, 158(8), R55.
15. Wang, W., Luo, Q., Li, B., Wei, X., Li, L., & Yang, Z. (2013). Recent progress in redox flow battery research and development. *Advanced Functional Materials*, 23(8), 970-986.
16. Weber, A. Z., Mench, M. M., Meyers, J. P., Ross, P. N., Gostick, J. T., & Liu, Q. (2011). Redox flow batteries: a review. *Journal of applied electrochemistry*, 41, 1137-1164.
17. Thaller, L. H. (1974). Electrically rechargeable redox flow cells. In *9th Intersociety energy conversion engineering conference* (pp. 924-928).
18. De Leon, C. P., Frías-Ferrer, A., González-García, J., Szánto, D. A., & Walsh, F. C.

- (2006). Redox flow cells for energy conversion. *Journal of power sources*, 160(1), 716-732.
19. Singh, P., & Jonshagen, B. (1991). Zinc–bromine battery for energy storage. *Journal of power sources*, 35(4), 405-410.
  20. Skyllas-Kazacos, M., & Limantari, Y. (2004). Kinetics of the chemical dissolution of vanadium pentoxide in acidic bromide solutions. *Journal of applied electrochemistry*, 34, 681-685.
  21. Sum, E., Rychcik, M., & Skyllas-Kazacos, M. (1985). Investigation of the V (V)/V (IV) system for use in the positive half-cell of a redox battery. *J. Power Sources;(Switzerland)*, 16(2).
  22. Sum, E., & Skyllas-Kazacos, M. (1985). A study of the V (II)/V (III) redox couple for redox flow cell applications. *Journal of Power sources*, 15(2-3), 179-190.
  23. Wang, W., Kim, S., Chen, B., Nie, Z., Zhang, J., Xia, G. G., ... & Yang, Z. (2011). A new redox flow battery using Fe/V redox couples in chloride supporting electrolyte. *Energy & Environmental Science*, 4(10), 4068-4073.
  24. Liu, S., Kok, M., Kim, Y., Barton, J. L., Brushett, F. R., & Gostick, J. (2017). Evaluation of electrospun fibrous mats targeted for use as flow battery electrodes. *Journal of The Electrochemical Society*, 164(9), A2038.
  25. Lee, N. J., Lee, S. W., Kim, K. J., Kim, J. H., Park, M. S., Jeong, G., ... & Byun, D. (2012). Development of carbon composite bipolar plates for vanadium redox flow batteries. *Bulletin of the Korean Chemical Society*, 33(11), 3589-3592.
  26. Qi, Z., & Koenig, G. M. (2017). Flow battery systems with solid electroactive materials. *Journal of Vacuum Science & Technology B*, 35(4).
  27. Shigematsu, T. (2011). Redox flow battery for energy storage. *SEI technical review*, 73(7), 13.
  28. Giner, J. D., & Stark, H. H. (1984). *Redox battery including a bromine positive electrode and a chromium ion negative electrode and method* (No. US 4469760).
  29. Skyllas-Kazacos, M. (2003). Novel vanadium chloride/polyhalide redox flow battery. *Journal of Power Sources*, 124(1), 299-302.
  30. Liu, Y., Xia, X., & Liu, H. (2004). Studies on cerium (Ce<sup>4+</sup>/Ce<sup>3+</sup>)–vanadium (V<sup>2+</sup>/V<sup>3+</sup>) redox flow cell—cyclic voltammogram response of Ce<sup>4+</sup>/Ce<sup>3+</sup> redox couple in H<sub>2</sub>SO<sub>4</sub> solution. *Journal of power sources*, 130(1-2), 299-305.
  31. R. L. Clarke, B. Dougherty, S. Harrison, P. J. Millington, S. Mohanta, Cerium batteries, US Patent 7,625,663 (Dec. 1 2009).
  32. Rychcik, M., & Skyllas-Kazacos, M. (1988). Characteristics of a new all-vanadium redox flow battery. *Journal of power sources*, 22(1), 59-67.
  33. Leung, P. K., Ponce-de-León, C., Low, C. T. J., & Walsh, F. C. (2011). Zinc deposition and dissolution in methanesulfonic acid onto a carbon composite electrode as the negative electrode reactions in a hybrid redox flow battery. *Electrochimica Acta*, 56(18), 6536-6546.
  34. Chai, J., Lashgari, A., & Jiang, J. J. (2020). Electroactive materials for next-generation redox flow batteries: from inorganic to organic. In *Clean Energy Materials* (pp. 1-47). American Chemical Society.
  35. Zhou, X., Liu, Q., Jiang, C., Ji, B., Ji, X., Tang, Y., & Cheng, H. M. (2020). Strategies towards low-cost dual-ion batteries with high performance. *Angewandte Chemie International Edition*, 59(10), 3802-3832.
  36. Placke, T., Heckmann, A., Schmuck, R., Meister, P., Beltrop, K., & Winter, M. (2018).

- Perspective on performance, cost, and technical challenges for practical dual-ion batteries. *Joule*, 2(12), 2528-2550.
37. Wu, X., Liu, J., Xiang, X., Zhang, J., Hu, J., & Wu, Y. (2014). Electrolytes for vanadium redox flow batteries. *Pure and Applied Chemistry*, 86(5), 661-669.
  38. Martin, J., Schafner, K., & Turek, T. (2020). Preparation of electrolyte for vanadium redox-flow batteries based on vanadium pentoxide. *Energy Technology*, 8(9), 2000522.
  39. Buckley, D. N., Oboroceanu, D., Quill, N., Lenihan, C., & Lynch, R. P. (2021). Modelling and accelerated testing of catholyte stability in vanadium flow batteries. *Journal of The Electrochemical Society*, 168(3), 030530.
  40. Jiang, B., Wu, L., Yu, L., Qiu, X., & Xi, J. (2016). A comparative study of Nafion series membranes for vanadium redox flow batteries. *Journal of Membrane Science*, 510, 18-26.
  41. Zhang, D., Xin, L., Xia, Y., Dai, L., Qu, K., Huang, K., ... & Xu, Z. (2021). Advanced Nafion hybrid membranes with fast proton transport channels toward high-performance vanadium redox flow battery. *Journal of membrane science*, 624, 119047.
  42. Shi, Y., Eze, C., Xiong, B., He, W., Zhang, H., Lim, T. M., ... & Zhao, J. (2019). Recent development of membrane for vanadium redox flow battery applications: A review. *Applied energy*, 238, 202-224.
  43. Zhang, K., Yan, C., & Tang, A. (2020). Unveiling electrode compression impact on vanadium flow battery from polarization perspective via a symmetric cell configuration. *Journal of Power Sources*, 479, 228816.
  44. Kaneko, H., Nozaki, K., Wada, Y., Aoki, T., Negishi, A., & Kamimoto, M. (1991). Vanadium redox reactions and carbon electrodes for vanadium redox flow battery. *Electrochimica Acta*, 36(7), 1191-1196.
  45. Xue, F. Q., Wang, Y. L., Wang, W. H., & Wang, X. D. (2008). Investigation on the electrode process of the Mn (II)/Mn (III) couple in redox flow battery. *Electrochimica Acta*, 53(22), 6636-6642.
  46. Zhong, S., Padeste, C., Kazacos, M., & Skyllas-Kazacos, M. (1993). Comparison of the physical, chemical and electrochemical properties of rayon-and polyacrylonitrile-based graphite felt electrodes. *Journal of Power sources*, 45(1), 29-41.
  47. Sun, B., & Skyllas-Kazacos, M. (1992). Modification of graphite electrode materials for vanadium redox flow battery application—I. Thermal treatment. *Electrochimica acta*, 37(7), 1253-1260.
  48. Liu, T., Serrano, J., Elliott, J., Yang, X., Cathcart, W., Wang, Z., ... & Liu, G. (2020). Exceptional capacitive deionization rate and capacity by block copolymer-based porous carbon fibers. *Science Advances*, 6(16), eaaz0906.
  49. Zhou, X. L., Zhao, T. S., An, L., Zeng, Y. K., & Wei, L. (2017). Critical transport issues for improving the performance of aqueous redox flow batteries. In *Journal of Power Sources* (Vol. 339, pp. 1–12). Elsevier B.V. <https://doi.org/10.1016/j.jpowsour.2016.11.040>
  50. Grady, B. P. (2011). *Carbon nanotube-polymer composites: manufacture, properties, and applications*. John Wiley & Sons.
  51. Lee, J., Yun, L., & Park, J. (2005). Anisotropic properties of needle punched carbon/carbon composites. In *18th International conference on composite materials* (pp. 1-4).

52. He, Z., Shi, L., Shen, J., He, Z., & Liu, S. (2015). Effects of nitrogen doping on the electrochemical performance of graphite felts for vanadium redox flow batteries. *International Journal of Energy Research*, 39(5), 709-716.
53. Le, T. X. H., Bechelany, M., & Cretin, M. (2017). Carbon felt based-electrodes for energy and environmental applications: A review. *Carbon*, 122, 564-591.
54. Wu, Y., Reddy, M. V., Chowdari, B. V. R., & Ramakrishna, S. (2013). Long-term cycling studies on electrospun carbon nanofibers as anode material for lithium ion batteries. *ACS applied materials & interfaces*, 5(22), 12175-12184.5, 12175.
55. Kim, D., Lee, D., Kim, J., & Moon, J. (2012). Electrospun Ni-added SnO<sub>2</sub>-carbon nanofiber composite anode for high-performance lithium-ion batteries. *ACS applied materials & interfaces*, 4(10), 5408-5415.
56. Ma, X., Kolla, P., Yang, R., Wang, Z., Zhao, Y., Smirnova, A. L., & Fong, H. (2017). Electrospun polyacrylonitrile nanofibrous membranes with varied fiber diameters and different membrane porosities as lithium-ion battery separators. *Electrochimica Acta*, 236, 417-423.
57. Freitag, K. M., Kirchhain, H., Wüllen, L. V., & Nilges, T. (2017). Enhancement of Li ion conductivity by electrospun polymer fibers and direct fabrication of solvent-free separator membranes for Li ion batteries. *Inorganic chemistry*, 56(4), 2100-2107.
58. Ding, Y., Hou, H., Zhao, Y., Zhu, Z., & Fong, H. (2016). Electrospun polyimide nanofibers and their applications. *Progress in Polymer Science*, 61, 67-103.
59. Yanilmaz, M., & Zhang, X. (2015). Polymethylmethacrylate/polyacrylonitrile membranes via centrifugal spinning as separator in Li-ion batteries. *Polymers*, 7(4), 629-643.
60. Chevalier, S., Ge, N., Lee, J., George, M. G., Liu, H., Shrestha, P., ... & Bazylak, A. (2017). Novel electrospun gas diffusion layers for polymer electrolyte membrane fuel cells: Part II. In operando synchrotron imaging for microscale liquid water transport characterization. *Journal of Power Sources*, 352, 281-290.
61. Kok, M. D., Khalifa, A., & Gostick, J. T. (2016). Multiphysics simulation of the flow battery cathode: cell architecture and electrode optimization. *Journal of The Electrochemical Society*, 163(7), A1408.
62. Taylor, G. I. Disintegration of Water Drops in an Electric Field. *Proc. R. Soc. A* **1964**, 280 (1382), 383. <https://doi.org/10.1098/rspa.1964.0151>
63. Newcomb, B. A. (2016). Processing, structure, and properties of carbon fibers. *Composites Part A: Applied Science and Manufacturing*, 91, 262-282.
64. Gupta, A. K., Paliwal, D. K., & Bajaj, P. (1991). Acrylic precursors for carbon fibers. *Journal of Macromolecular Science, Part C: Polymer Reviews*, 31(1), 1-89.
65. MInus, M., & Kumar, S. (2005). The processing, properties, and structure of carbon fibers. *Jom*, 57, 52-58.
66. Gostick, J. T., Fowler, M. W., Pritzker, M. D., Ioannidis, M. A., & Behra, L. M. (2006). In-plane and through-plane gas permeability of carbon fiber electrode backing layers. *Journal of Power sources*, 162(1), 228-238.
67. Wang, T., & Kumar, S. (2006). Electrospinning of polyacrylonitrile nanofibers. *Journal of applied polymer science*, 102(2), 1023-1029.
68. Zhang, B. W., Lei, Y., Bai, B. F., & Zhao, T. S. (2019). A two-dimensional model for the design of flow fields in vanadium redox flow batteries. *International Journal of Heat and Mass Transfer*, 135, 460-469.
69. Huang, Z., Mu, A., Wu, L., Yang, B., Qian, Y., & Wang, J. (2022). Comprehensive

- analysis of critical issues in all-vanadium redox flow battery. *ACS Sustainable Chemistry & Engineering*, 10(24), 7786-7810.
70. Chalamala, B. R., Soundappan, T., Fisher, G. R., Anstey, M. R., Viswanathan, V. V., & Perry, M. L. (2014). Redox flow batteries: an engineering perspective. *Proceedings of the IEEE*, 102(6), 976-999.
  71. Hamilton, P. J., & Pollet, B. G. (2010). Polymer electrolyte membrane fuel cell (PEMFC) flow field plate: design, materials and characterisation. *Fuel cells*, 10(4), 489-509.
  72. Li, X., & Sabir, I. (2005). Review of bipolar plates in PEM fuel cells: Flow-field designs. *International journal of hydrogen energy*, 30(4), 359-371.
  73. Wong, C. W., Zhao, T. S., Ye, Q., & Liu, J. G. (2006). Experimental investigations of the anode flow field of a micro direct methanol fuel cell. *Journal of Power Sources*, 155(2), 291-296.
  74. Yang, H., Zhao, T. S., & Ye, Q. (2005). In situ visualization study of CO<sub>2</sub> gas bubble behavior in DMFC anode flow fields. *Journal of Power Sources*, 139(1-2), 79-90.
  75. Dennison, C. R., Agar, E., Akuzum, B., & Kumbur, E. C. (2015). Enhancing mass transport in redox flow batteries by tailoring flow field and electrode design. *Journal of The Electrochemical Society*, 163(1), A5163.
  76. Xu, Q., & Zhao, T. S. (2013). Determination of the mass-transport properties of vanadium ions through the porous electrodes of vanadium redox flow batteries. *Physical Chemistry Chemical Physics*, 15(26), 10841-10848.
  77. Darling, R. M., & Perry, M. L. (2014). The influence of electrode and channel configurations on flow battery performance. *Journal of The Electrochemical Society*, 161(9), A1381.
  78. Houser, J., Clement, J., Pezeshki, A., & Mench, M. M. (2016). Influence of architecture and material properties on vanadium redox flow battery performance. *Journal of Power Sources*, 302, 369-377.
  79. Jyothi Latha, T., & Jayanti, S. (2014). Hydrodynamic analysis of flow fields for redox flow battery applications. *Journal of Applied Electrochemistry*, 44, 995-1006.
  80. Latha, T. J., & Jayanti, S. (2014). Ex-situ experimental studies on serpentine flow field design for redox flow battery systems. *Journal of Power Sources*, 248, 140-146.
  81. Tsushima, S., & Suzuki, T. (2020). Modeling and simulation of vanadium redox flow battery with interdigitated flow field for optimizing electrode architecture. *Journal of The Electrochemical Society*, 167(2), 020553.
  82. Maleki, M., El-Nagar, G. A., Bernsmeier, D., Schneider, J., & Roth, C. (2020). Fabrication of an efficient vanadium redox flow battery electrode using a free-standing carbon-loaded electrospun nanofibrous composite. *Scientific Reports*, 10(1), 11153.
  83. Zhou, X. L., Zeng, Y. K., Zhu, X. B., Wei, L., & Zhao, T. S. (2016). A high-performance dual-scale porous electrode for vanadium redox flow batteries. *Journal of Power Sources*, 325, 329-336.
  84. Shao, Y., Wang, X., Engelhard, M., Wang, C., Dai, S., Liu, J., ... & Lin, Y. (2010). Nitrogen-doped mesoporous carbon for energy storage in vanadium redox flow batteries. *Journal of Power Sources*, 195(13), 4375-4379.
  85. Yadav, S., Kok, M. D., Forner-Cuenca, A., Tenny, K. M., Chiang, Y. M., Brushett, F. R., ... & Gostick, J. T. (2021). Fabrication of high surface area ribbon electrodes for use in redox flow batteries via coaxial electrospinning. *Journal of Energy Storage*, 33,

- 102079.
86. Sánchez-Díez, E., Ventosa, E., Guarnieri, M., Trovò, A., Flox, C., Marcilla, R., ... & Ferret, R. (2021). Redox flow batteries: Status and perspective towards sustainable stationary energy storage. *Journal of Power Sources*, *481*, 228804.
  87. Charvát, J., Mazúr, P., Dundálek, J., Povedič, J., Vrána, J., Mrlík, J., ... & Dinter, S. (2020). Performance enhancement of vanadium redox flow battery by optimized electrode compression and operational conditions. *Journal of Energy Storage*, *30*, 101468.
  88. Jiang, H. R., Sun, J., Wei, L., Wu, M. C., Shyy, W., & Zhao, T. S. (2020). A high power density and long cycle life vanadium redox flow battery. *Energy Storage Materials*, *24*, 529-540.
  89. Ma, L., Dong, X., Chen, M., Zhu, L., Wang, C., Yang, F., & Dong, Y. (2017). Fabrication and water treatment application of carbon nanotubes (CNTs)-based composite membranes: a review. *Membranes*, *7*(1), 16.
  90. Sun, X., Bai, L., Li, J., Huang, L., Sun, H., & Gao, X. (2021). Robust preparation of flexibly super-hydrophobic carbon fiber membrane by electrospinning for efficient oil-water separation in harsh environments. *Carbon*, *182*, 11-22.
  91. Jiang, T., Zhang, Y., Olayiwola, S., Lau, C., Fan, M., Ng, K., & Tan, G. (2022). Biomass-derived porous carbons support in phase change materials for building energy efficiency: a review. *Materials Today Energy*, *23*, 100905.
  92. Xia, M., Zhao, S., Hasi, Q. M., Zhang, Y., Li, L., & Chen, L. (2021). Superhydrophilic and oil-repellent porous material based on halloysite nanotubes and wood fibers for efficient solar steam generation. *Materials Today Energy*, *21*, 100726.
  93. Wang, X., Zhang, X., Fu, G., & Tang, Y. (2021). Recent progress of electrospun porous carbon-based nanofibers for oxygen electrocatalysis. *Materials Today Energy*, *22*, 100850.
  94. Yang, D. S., Han, J. H., Jeon, J. W., Lee, J. Y., Kim, D. G., Seo, D. H., ... & Hong, Y. T. (2019). Multimodal porous and nitrogen-functionalized electrode based on graphite felt modified with carbonized porous polymer skin layer for all-vanadium redox flow battery. *Materials today energy*, *11*, 159-165.
  95. Xu, Z., Fan, Q., Li, Y., Wang, J., & Lund, P. D. (2020). Review of zinc dendrite formation in zinc bromine redox flow battery. *Renewable and Sustainable Energy Reviews*, *127*, 109838.
  96. Amini, K., & Pritzker, M. D. (2020). Life-cycle analysis of zinc-cerium redox flow batteries. *Electrochimica Acta*, *356*, 136785.
  97. Kim, D., Kim, Y., Lee, Y., & Jeon, J. (2019). 1, 2-Dimethylimidazole based bromine complexing agents for vanadium bromine redox flow batteries. *International Journal of Hydrogen Energy*, *44*(23), 12024-12032.
  98. Xu, Q., Qin, L. Y., Ji, Y. N., Leung, P. K., Su, H. N., Qiao, F., ... & Li, H. M. (2019). A deep eutectic solvent (DES) electrolyte-based vanadium-iron redox flow battery enabling higher specific capacity and improved thermal stability. *Electrochimica Acta*, *293*, 426-431.
  99. Chen, H., Zhang, X., Wu, S., Chen, F., & Xu, J. (2022). A comparative study of iron-vanadium and all-vanadium flow battery for large scale energy storage. *Chemical Engineering Journal*, *429*, 132403.
  100. Yu, H., Pritzker, M., & Gostick, J. (2023). Use of Mixed Methanesulfonic Acid/Sulfuric Acid as Positive Supporting Electrolyte in Zn-Ce Redox Flow

- Battery. *Journal of The Electrochemical Society*, 170(2), 020536.
101. Goulet, M. A., Eikerling, M., & Kjeang, E. (2015). Direct measurement of electrochemical reaction kinetics in flow-through porous electrodes. *Electrochemistry Communications*, 57, 14-17.
  102. Poli, N., Trovò, A., Fischer, P., Noack, J., & Guarnieri, M. (2023). Electrochemical rebalancing process for vanadium flow batteries: Sizing and economic assessment. *Journal of Energy Storage*, 58, 106404.
  103. Meinel, J., Schönfeld, K., Kirsten, M., Kittler, K., Michaelis, A., & Cherif, C. (2017). Optimization of the temperature program to scale up the stabilization of polyacrylonitrile fibers. *Composites Part A: Applied Science and Manufacturing*, 96, 37-45.
  104. Lin, C. H., Zhuang, Y. D., Tsai, D. G., Wei, H. J., & Liu, T. Y. (2020). Performance enhancement of vanadium redox flow battery by treated carbon felt electrodes of polyacrylonitrile using atmospheric pressure plasma. *Polymers*, 12(6), 1372.
  105. Zeng, L., Sun, J., Zhao, T. S., Ren, Y. X., & Wei, L. (2020). Balancing the specific surface area and mass diffusion property of electrospun carbon fibers to enhance the cell performance of vanadium redox flow battery. *International Journal of Hydrogen Energy*, 45(22), 12565-12576.
  106. Sun, J., Zeng, L., Jiang, H. R., Chao, C. Y. H., & Zhao, T. S. (2018). Formation of electrodes by self-assembling porous carbon fibers into bundles for vanadium redox flow batteries. *Journal of Power Sources*, 405, 106-113.
  107. He, Z., Li, M., Li, Y., Wang, L., Zhu, J., Meng, W., ... & Dai, L. (2019). Electrospun nitrogen-doped carbon nanofiber as negative electrode for vanadium redox flow battery. *Applied Surface Science*, 469, 423-430.
  108. Hassan, A., & Tzedakis, T. (2019). Enhancement of the electrochemical activity of a commercial graphite felt for vanadium redox flow battery (VRFB), by chemical treatment with acidic solution of K<sub>2</sub>Cr<sub>2</sub>O<sub>7</sub>. *Journal of Energy Storage*, 26, 100967.
  109. Cheng, D., Li, Y., Zhang, J., Tian, M., Wang, B., He, Z., ... & Wang, L. (2020). Recent advances in electrospun carbon fiber electrode for vanadium redox flow battery: properties, structures, and perspectives. *Carbon*, 170, 527-542.
  110. Jiang, Y., Liu, Z., Lv, Y., Tang, A., Dai, L., Wang, L., & He, Z. (2022). Perovskite enables high performance vanadium redox flow battery. *Chemical Engineering Journal*, 443, 136341.
  111. He, Z., Jiang, Y., Li, Y., Zhu, J., Zhou, H., Meng, W., ... & Dai, L. (2018). Carbon layer-exfoliated, wettability-enhanced, SO<sub>3</sub>H-functionalized carbon paper: A superior positive electrode for vanadium redox flow battery. *Carbon*, 127, 297-304.
  112. Jiang, Y., Cheng, G., Li, Y., He, Z., Zhu, J., Meng, W., ... & Wang, L. (2021). Promoting vanadium redox flow battery performance by ultra-uniform ZrO<sub>2</sub>@ C from metal-organic framework. *Chemical Engineering Journal*, 415, 129014.
  113. Shan, C., Wang, Y., Xie, S., Guan, H. Y., Argueta, M., & Yue, Y. (2019). Free-standing nitrogen-doped graphene-carbon nanofiber composite mats: electrospinning synthesis and application as anode material for lithium-ion batteries. *Journal of Chemical Technology & Biotechnology*, 94(12), 3793-3799.
  114. Tan, H. L., Sanira Putri, M. K., Idris, S. S., Hartikainen, N., Abu Bakar, N. F., Keirouz, A., & Radacsi, N. (2020). High-throughput fabrication of carbonized electrospun polyacrylonitrile/poly (acrylic acid) nanofibers with additives for enhanced electrochemical sensing. *Journal of Applied Polymer Science*, 137(43), 49341.

115. Wen, Y., Kok, M. D., Tafoya, J. P. V., Sobrido, A. B. J., Bell, E., Gostick, J. T., ... & Jervis, R. (2021). Electrospinning as a route to advanced carbon fibre materials for selected low-temperature electrochemical devices: A review. *Journal of Energy Chemistry*, *59*, 492-529.
116. Goulet, M. A., Habisch, A., & Kjeang, E. (2016). In situ enhancement of flow-through porous electrodes with carbon nanotubes via flowing deposition. *Electrochimica Acta*, *206*, 36-44.
117. Kim, Y., Asset, T., Wei, F., Atanassov, P., Secanell, M., Barralet, J., & Gostick, J. T. (2021). Fabrication of platinum group metal-free catalyst layer with enhanced mass transport characteristics via an electrospaying technique. *Materials Today Energy*, *20*, 100641.
118. Grothe, T., Storck, J. L., Dotter, M., & Ehrmann, A. (2020). Impact of solid content in the electrospinning solution on physical and chemical properties of polyacrylonitrile (PAN) nanofibrous mats. *Tekstilec*, *63*(3), 225-232.
119. Mukherjee, M., Bonnet, C., & Lopicque, F. (2020). Estimation of through-plane and in-plane gas permeability across gas diffusion layers (GDLs): Comparison with equivalent permeability in bipolar plates and relation to fuel cell performance. *International Journal of Hydrogen Energy*, *45*(24), 13428-13440.
120. Rashapov, R. R., Unno, J., & Gostick, J. T. (2015). Characterization of PEMFC gas diffusion layer porosity. *Journal of The Electrochemical Society*, *162*(6), F603.
121. Andisheh-Tadbir, M., Orfino, F. P., & Kjeang, E. (2016). Three-dimensional phase segregation of micro-porous layers for fuel cells by nano-scale X-ray computed tomography. *Journal of Power Sources*, *310*, 61-69.
122. Pokhrel, A., El Hannach, M., Orfino, F. P., Dutta, M., & Kjeang, E. (2016). Failure analysis of fuel cell electrodes using three-dimensional multi-length scale X-ray computed tomography. *Journal of Power Sources*, *329*, 330-338.
123. White, R. T., Ramani, D., Eberhardt, S., Najm, M., Orfino, F. P., Dutta, M., & Kjeang, E. (2019). Correlative X-ray tomographic imaging of catalyst layer degradation in fuel cells. *Journal of The Electrochemical Society*, *166*(13), F914.
124. Buades, A., Coll, B., & Morel, J. M. (2011). Non-local means denoising. *Image Processing On Line*, *1*, 208-212.
125. Gostick, J. T., Khan, Z. A., Tranter, T. G., Kok, M. D., Agnaou, M., Sadeghi, M., & Jervis, R. (2019). PoreSpy: A python toolkit for quantitative analysis of porous media images. *Journal of Open Source Software*, *4*(37), 1296.
126. Reed, D., Thomsen, E., Wang, W., Nie, Z., Li, B., Wei, X., ... & Sprengle, V. (2015). Performance of Nafion® N115, Nafion® NR-212, and Nafion® NR-211 in a 1 kW class all vanadium mixed acid redox flow battery. *Journal of Power Sources*, *285*, 425-430.
127. Pahlevaninezhad, M., Pahlevani, M., & Roberts, E. P. (2022). Effects of aluminum, iron, and manganese sulfate impurities on the vanadium redox flow battery. *Journal of Power Sources*, *529*, 231271.
128. Choi, J., Kim, S. S., Chung, Y. S., & Lee, S. (2020). Evolution of structural inhomogeneity in polyacrylonitrile fibers by oxidative stabilization. *Carbon*, *165*, 225-237.
129. Jervis, R., Kok, M. D., Montagut, J., Gostick, J. T., Brett, D. J., & Shearing, P. R. (2018). X-ray Nano Computed Tomography of Electrospun Fibrous Mats as Flow Battery Electrodes. *Energy Technology*, *6*(12), 2488-2500.

130. Thiam, B. G., & Vaudreuil, S. (2021). Recent membranes for vanadium redox flow batteries. *Journal of The Electrochemical Society*, 168(7), 070553.
131. Ishitobi, H., Doki, H., Shiraishi, S., Tsukada, H., Hatakeyama, Y., Obata, R., & Nakagawa, N. (2023). Enhancement of the Electrode Activity of the Vanadium Redox Flow Battery by Higher Crystallinity of Carbon Matrix Using Seamless and Consecutive-porous Carbon Materials. *Journal of The Electrochemical Society*, 170(1), 010536.
132. Gubler, L., Vonlanthen, D., Schneider, A., & Oldenburg, F. J. (2020). Composite membranes containing a porous separator and a polybenzimidazole thin film for vanadium redox flow batteries. *Journal of The Electrochemical Society*, 167(10), 100502.
133. Maurya, S., Nguyen, P. T., Kim, Y. S., Kang, Q., & Mukundan, R. (2018). Effect of flow field geometry on operating current density, capacity and performance of vanadium redox flow battery. *Journal of Power Sources*, 404, 20-27.
134. Xu, Q., Zhao, T. S., & Zhang, C. (2014). Performance of a vanadium redox flow battery with and without flow fields. *Electrochimica Acta*, 142, 61-67.
135. Kumar, S., & Jayanti, S. (2016). Effect of flow field on the performance of an all-vanadium redox flow battery. *Journal of Power Sources*, 307, 782-787.
136. Fetyan, A., Derr, I., Kayarkatte, M. K., Langner, J., Bernsmeier, D., Kraehnert, R., & Roth, C. (2015). Electrospun carbon nanofibers as alternative electrode materials for vanadium redox flow batteries. *ChemElectroChem*, 2(12), 2055-2060.
137. Sun, J., Jiang, H. R., Wu, M. C., Fan, X. Z., Chao, C. Y. H., & Zhao, T. S. (2020). A novel electrode formed with electrospun nano-and micro-scale carbon fibers for aqueous redox flow batteries. *Journal of Power Sources*, 470, 228441.
138. Lee, K. M., Pahlevaninezhad, M., Smith, V., Abouali, S., Orfino, F. P., Kjeang, E., ... & Gostick, J. T. (2023). Improvement of vanadium redox flow battery performance obtained by compression and laser perforation of electrospun electrodes. *Materials Today Energy*, 35, 101333.
139. Messaggi, M., Canzi, P., Mereu, R., Baricci, A., Inzoli, F., Casalegno, A., & Zago, M. (2018). Analysis of flow field design on vanadium redox flow battery performance: Development of 3D computational fluid dynamic model and experimental validation. *Applied energy*, 228, 1057-1070.
140. Tomadakis, M. M., & Sotirchos, S. V. (1993). Transport properties of random arrays of freely overlapping cylinders with various orientation distributions. *The Journal of chemical physics*, 98(1), 616-626.
141. Zhou, X. L., Zhao, T. S., An, L., Zeng, Y. K., & Yan, X. H. (2015). A vanadium redox flow battery model incorporating the effect of ion concentrations on ion mobility. *Applied energy*, 158, 157-166.
142. Knehr, K. W., Agar, E., Dennison, C. R., Kalidindi, A. R., & Kumbur, E. C. (2012). A transient vanadium flow battery model incorporating vanadium crossover and water transport through the membrane. *Journal of The Electrochemical Society*, 159(9), A1446.
143. Jackson, G. W., & James, D. F. (1986). The permeability of fibrous porous media. *The Canadian Journal of Chemical Engineering*, 64(3), 364-374.
144. Tomadakis, M. M., & Robertson, T. J. (2005). Viscous permeability of random fiber structures: comparison of electrical and diffusional estimates with experimental and analytical results. *Journal of Composite Materials*, 39(2), 163-188.

145. Kok, M. D., & Gostick, J. T. (2015). Transport properties of electrospun fibrous membranes with controlled anisotropy. *Journal of membrane science*, 473, 237-244.
146. Schmal, D., Van Erkel, J., & Van Duin, P. J. (1986). Mass transfer at carbon fibre electrodes. *Journal of applied electrochemistry*, 16, 422-430.
147. Yamamura, T., Watanabe, N., Yano, T., & Shiokawa, Y. (2005). Electron-transfer kinetics of  $\text{Np}^{3+}/\text{Np}^{4+}$ ,  $\text{NpO}_2^{+}/\text{NpO}_2^{2+}$ ,  $\text{V}^{2+}/\text{V}^{3+}$ , and  $\text{VO}_2^{+}/\text{VO}_2^{+}$  at carbon electrodes. *Journal of The Electrochemical Society*, 152(4), A830.
148. Lei, Y., Zhang, B. W., Bai, B. F., & Zhao, T. S. (2015). A transient electrochemical model incorporating the Donnan effect for all-vanadium redox flow batteries. *Journal of Power Sources*, 299, 202-211.
149. Oriji, G., Katayama, Y., & Miura, T. (2004). Investigation on V (IV)/V (V) species in a vanadium redox flow battery. *Electrochimica Acta*, 49(19), 3091-3095.
150. Yin, C., Gao, Y., Guo, S., & Tang, H. (2014). A coupled three dimensional model of vanadium redox flow battery for flow field designs. *Energy*, 74, 886-895.
151. Forner-Cuenca, A., Penn, E. E., Oliveira, A. M., & Brushett, F. R. (2019). Exploring the role of electrode microstructure on the performance of non-aqueous redox flow batteries. *Journal of The Electrochemical Society*, 166(10), A2230-A2241.
152. Gerhardt, M. R., Wong, A. A., & Aziz, M. J. (2018). The effect of interdigitated channel and land dimensions on flow cell performance. *Journal of The Electrochemical Society*, 165(11), A2625.
153. Tsampas, M. N., Pikos, A., Brosda, S., Katsaounis, A., & Vayenas, C. G. (2006). The effect of membrane thickness on the conductivity of Nafion. *Electrochimica Acta*, 51(13), 2743-2755.
154. Misaghian, N., Sadeghi, M. A., Lee, K. M., Roberts, E. P., & Gostick, J. T. (2023). Utilizing Pore Network Modeling for Performance Analysis of Multi-Layer Electrodes in Vanadium Redox Flow Batteries. *Journal of The Electrochemical Society*, 170(7), 070520.
155. Baky, M. A. H., Rahman, M. M., & Islam, A. S. (2017). Development of renewable energy sector in Bangladesh: Current status and future potentials. *Renewable and Sustainable Energy Reviews*, 73, 1184-1197.
156. Perera, F. (2018). Pollution from fossil-fuel combustion is the leading environmental threat to global pediatric health and equity: Solutions exist. *International journal of environmental research and public health*, 15(1), 16.
157. Patel, M., Zhang, X., & Kumar, A. (2016). Techno-economic and life cycle assessment on lignocellulosic biomass thermochemical conversion technologies: A review. *Renewable and Sustainable Energy Reviews*, 53, 1486-1499.
158. Patel, M., & Kumar, A. (2016). Production of renewable diesel through the hydroprocessing of lignocellulosic biomass-derived bio-oil: A review. *Renewable and Sustainable Energy Reviews*, 58, 1293-1307.
159. Luo, X., Wang, J., Dooner, M., & Clarke, J. (2015). Overview of current development in electrical energy storage technologies and the application potential in power system operation. *Applied energy*, 137, 511-536.
160. Ourahou, M., Ayrir, W., Hassouni, B. E., & Haddi, A. (2020). Review on smart grid control and reliability in presence of renewable energies: Challenges and prospects. *Mathematics and computers in simulation*, 167, 19-31.
161. Bajaj, M., & Singh, A. K. (2020). Grid integrated renewable DG systems: A review of power quality challenges and state-of-the-art mitigation techniques. *International*

- Journal of Energy Research*, 44(1), 26-69.
162. Sinsel, S. R., Riemke, R. L., & Hoffmann, V. H. (2020). Challenges and solution technologies for the integration of variable renewable energy sources—a review. *renewable energy*, 145, 2271-2285.
  163. Basit, M. A., Dilshad, S., Badar, R., & Sami ur Rehman, S. M. (2020). Limitations, challenges, and solution approaches in grid-connected renewable energy systems. *International Journal of Energy Research*, 44(6), 4132-4162.
  164. Colmenar-Santos, A., Linares-Mena, A. R., Molina-Ibáñez, E. L., Rosales-Asensio, E., & Borge-Diez, D. (2020). Technical challenges for the optimum penetration of grid-connected photovoltaic systems: Spain as a case study. *Renewable energy*, 145, 2296-2305.
  165. McLarnon, F. R., & Cairns, E. J. (1989). Energy storage. *Annual review of energy*, 14(1), 241-271.
  166. Baker, J. N., & Collinson, A. (1999). Electrical energy storage at the turn of the millennium. *Power Engineering Journal*, 13(3), 107-112.
  167. Walawalkar, R., Apt, J., & Mancini, R. (2007). Economics of electric energy storage for energy arbitrage and regulation in New York. *Energy Policy*, 35(4), 2558-2568.
  168. Koot, M., Kessels, J. T., De Jager, B., Heemels, W. P. M. H., Van den Bosch, P. P. J., & Steinbuch, M. (2005). Energy management strategies for vehicular electric power systems. *IEEE transactions on vehicular technology*, 54(3), 771-782.
  169. Weinstock, I. B. (2002). Recent advances in the US Department of Energy's energy storage technology research and development programs for hybrid electric and electric vehicles. *Journal of Power Sources*, 110(2), 471-474.
  170. Sun, C. N., Delnick, F. M., Aaron, D. S., Papandrew, A. B., Mench, M. M., & Zawodzinski, T. A. (2013). Probing electrode losses in all-vanadium redox flow batteries with impedance spectroscopy. *ECS Electrochemistry Letters*, 2(5), A43.
  171. Liu, Q., Turhan, A., Zawodzinski, T. A., & Mench, M. M. (2013). In situ potential distribution measurement in an all-vanadium flow battery. *Chemical Communications*, 49(56), 6292-6294.
  172. Shah, A. A., Watt-Smith, M. J., & Walsh, F. C. (2008). A dynamic performance model for redox-flow batteries involving soluble species. *Electrochimica Acta*, 53(27), 8087-8100.
  173. Al-Fetlawi, H., Shah, A. A., & Walsh, F. C. (2009). Non-isothermal modelling of the all-vanadium redox flow battery. *Electrochimica Acta*, 55(1), 78-89.
  174. Hsieh, S. S., Wu, H. C., & Her, B. S. (2010). A novel design for a flow field configuration, of a direct methanol fuel cell. *Journal of Power Sources*, 195(10), 3224-3230.
  175. Arvay, A., French, J., Wang, J. C., Peng, X. H., & Kannan, A. M. (2013). Nature inspired flow field designs for proton exchange membrane fuel cell. *International Journal of hydrogen energy*, 38(9), 3717-3726.
  176. Li, X., & Sabir, I. (2005). Review of bipolar plates in PEM fuel cells: Flow-field designs. *International journal of hydrogen energy*, 30(4), 359-371.
  177. Srouji, A. K., Zheng, L. J., Dross, R., Turhan, A., & Mench, M. M. (2013). Ultra-high current density water management in polymer electrolyte fuel cell with porous metallic flow field. *Journal of Power Sources*, 239, 433-442.
  178. Zheng, L. J., Srouji, A. K., Turhan, A., & Mench, M. M. (2012). Computational exploration of ultra-high current PEFC operation with porous flow field. *Journal of*

- The Electrochemical Society*, 159(7), F267.
179. Cho, K. T., & Mench, M. M. (2010). Coupled effects of flow field geometry and diffusion media material structure on evaporative water removal from polymer electrolyte fuel cells. *International Journal of Hydrogen Energy*, 35(22), 12329-12340.
  180. Kumbur, E. C., Sharp, K. V., & Mench, M. M. (2006). Liquid droplet behavior and instability in a polymer electrolyte fuel cell flow channel. *Journal of power sources*, 161(1), 333-345.
  181. Yoon, S. Y., Ross, J. W., Mench, M. M., & Sharp, K. V. (2006). Gas-phase particle image velocimetry (PIV) for application to the design of fuel cell reactant flow channels. *Journal of Power Sources*, 160(2), 1017-1025.
  182. Turhan, A., Heller, K., Brenizer, J. S., & Mench, M. M. (2008). Passive control of liquid water storage and distribution in a PEFC through flow-field design. *Journal of Power Sources*, 180(2), 773-783.
  183. Yoon, S. J., Kim, S., Kim, D. K., So, S., Hong, Y. T., & Hempelmann, R. (2020). Ionic liquid derived nitrogen-doped graphite felt electrodes for vanadium redox flow batteries. *Carbon*, 166, 131-137.

## References (Appendices)

1. Kok, M. D., Khalifa, A., & Gostick, J. T. (2016). Multiphysics simulation of the flow battery cathode: cell architecture and electrode optimization. *Journal of The Electrochemical Society*, 163(7), A1408.
2. Liu, S., Kok, M., Kim, Y., Barton, J. L., Brushett, F. R., & Gostick, J. (2017). Evaluation of electrospun fibrous mats targeted for use as flow battery electrodes. *Journal of The Electrochemical Society*, 164(9), A2038.
3. Mukherjee, M., Bonnet, C., & Lapique, F. (2020). Estimation of through-plane and in-plane gas permeability across gas diffusion layers (GDLs): Comparison with equivalent permeability in bipolar plates and relation to fuel cell performance. *International Journal of Hydrogen Energy*, 45(24), 13428-13440.
4. Rashapov, R. R., Unno, J., & Gostick, J. T. (2015). Characterization of PEMFC gas diffusion layer porosity. *Journal of The Electrochemical Society*, 162(6), F603.

## Appendices

### Permeability

The permeability of a fibrous porous material is one of the parameters affecting flow battery performance, and is well correlated by the Carman-Kozeny relationship [1] :

$$K = \frac{d_f^2 \varepsilon^3}{180 k_{CK} (1 - \varepsilon)^2} \quad S1$$

where  $K$  is the permeability coefficient, and  $k_{CK}$  is a fitting parameter, which accounts for the material structure, such as fibre morphology and shape. According to the Carman-Kozeny model, there are three ways to increase the permeability of porous electrode: increase the porosity, increase the fiber size, or decrease  $k_{CK}$ . In general, high permeability can be accomplished by increasing the fiber size but has a negative impact on the reactive surface area, as approximated by the filament analogue model [2]:

$$A_s = \frac{4(1 - \varepsilon)}{d_f} \quad S2$$

The porosity is already quite high for fibrous structure ( $> 85\%$ ). Meanwhile, the  $k_{CK}$  value is a function of the physical arrangement of the solid structure and can be affected by altering the sample's physical structure.

In the case of nitrogen gas, the compressibility of the fluid must be accounted, and thus Darcy's law is modified to the following expression.

$$m = \frac{KA}{\mu} \left( \frac{P_{IN}^2 - P_{OUT}^2}{2L_s RT / MW_{N_2}} \right) \quad S3$$

where  $m$  is the mass flow rate.  $A$  is the cross-sectional area,  $\mu$  is the viscosity  $Pa \cdot s$ ,  $P_{IN}$  is the inlet pressure,  $P_{OUT}$  is the outlet pressure (1atm),  $L_s$  is the length of the sample,  $R$  is the gas constant,  $T$  is the temperature, and  $MW_{N_2}$  is the molecular weight of nitrogen gas.

In-plane permeability was measured additionally with a radial flow to avoid compression. The average velocity was calculated with the following expression [3].

$$v_{av} = \frac{Q}{2\pi\delta(R_o - R_i)} \ln\left(\frac{R_o}{R_i}\right) \quad S4$$

where  $v_{av}$  is the average velocity of nitrogen gas,  $Q$  is the volumetric flow rate of nitrogen gas,  $\delta$  is the sample thickness,  $R_i$  is the inner radius, and  $R_o$  is the outer radius of the sample. The Darcy's equation was then modified to be applied to a disk geometry and utilized to calculate the in-plane permeability, as shown below.

$$\frac{P_{IN}^2 - P_{OUT}^2}{2(R_o - R_i)P_{OUT}} = \left(\frac{\mu}{K}\right) v_{av} \quad S5$$

### Porosity

The density of the solid could be obtained as [4]:

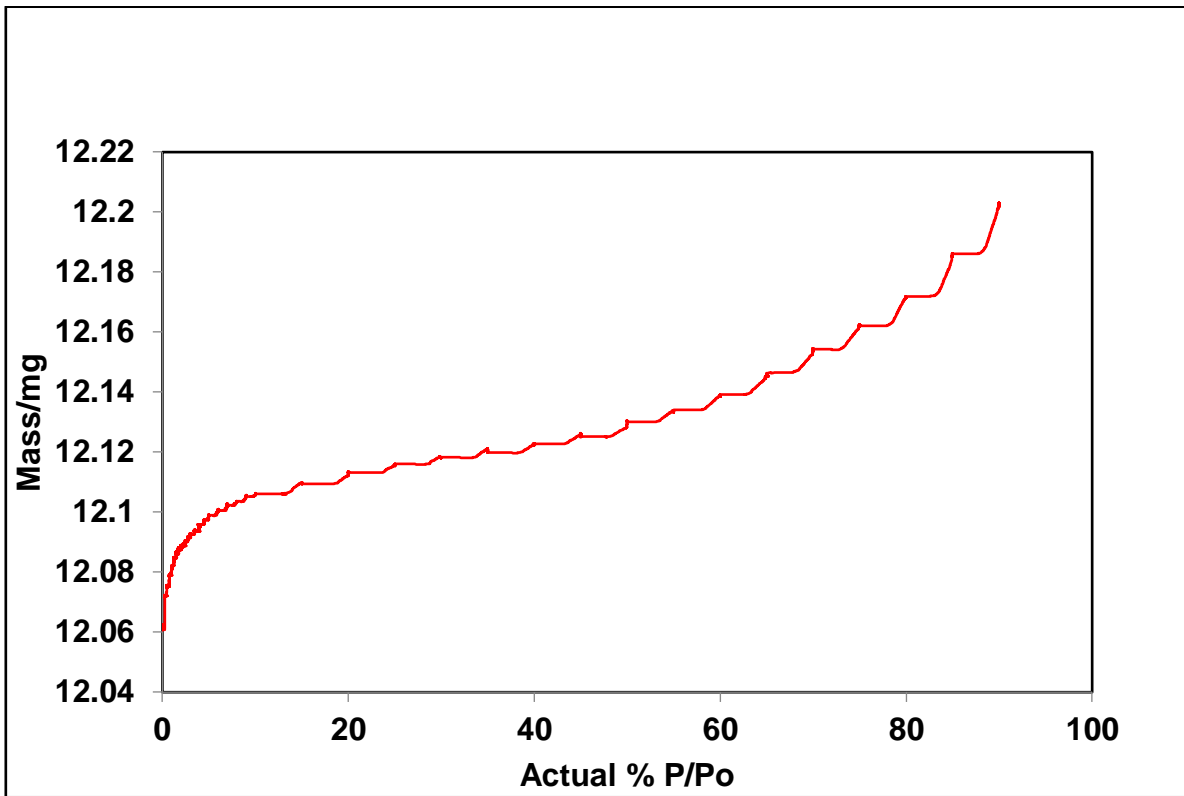
$$\rho_s = \rho_L \frac{m_{dry}}{m_l} = \rho_L \frac{m_{dry}}{m_{dry} - m_{wet}} \quad S6$$

where  $\rho_s$  and  $\rho_L$  are the solid and liquid density,  $m_{dry}$  is the dry weight of the sample,  $m_l$  is the weight of liquid displaced, and  $m_{wet}$  is the weight of the submerged sample. The porosity is then obtained from:

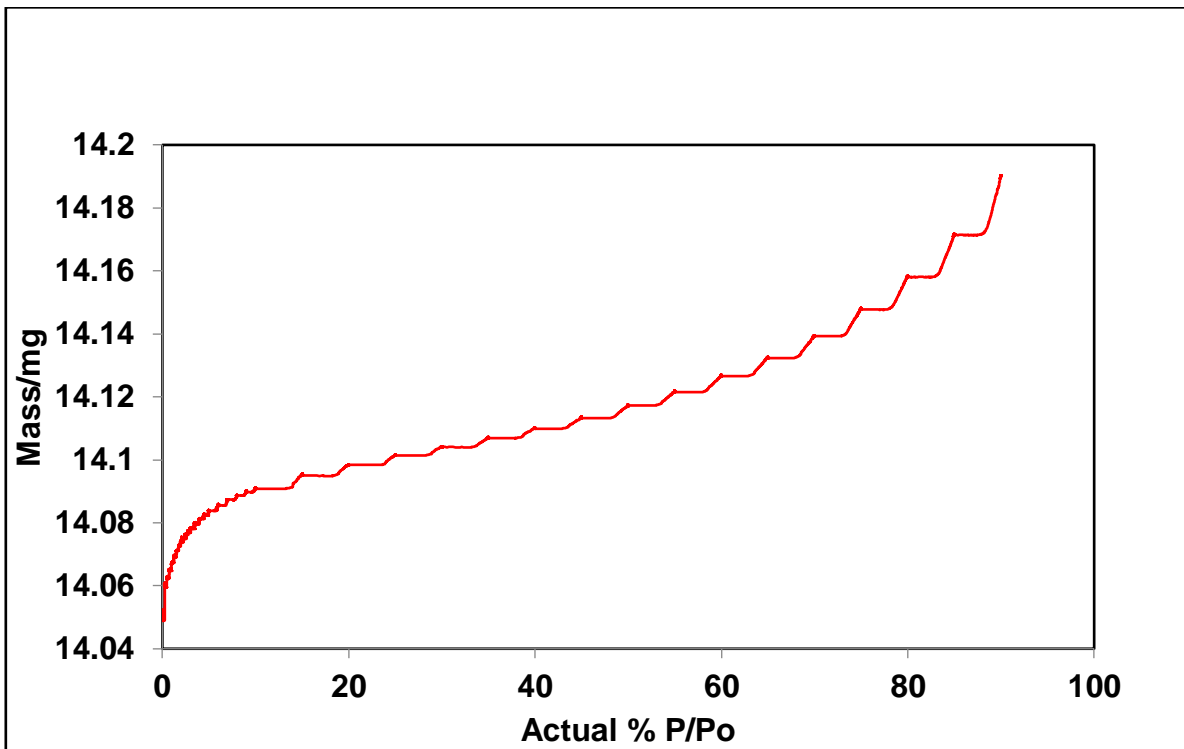
$$\varepsilon = 1 - \frac{m_{dry}/\rho_s}{V_b} \quad S7$$

where  $\varepsilon$  is the porosity, and  $V_b$  is the bulk volume of the sample.

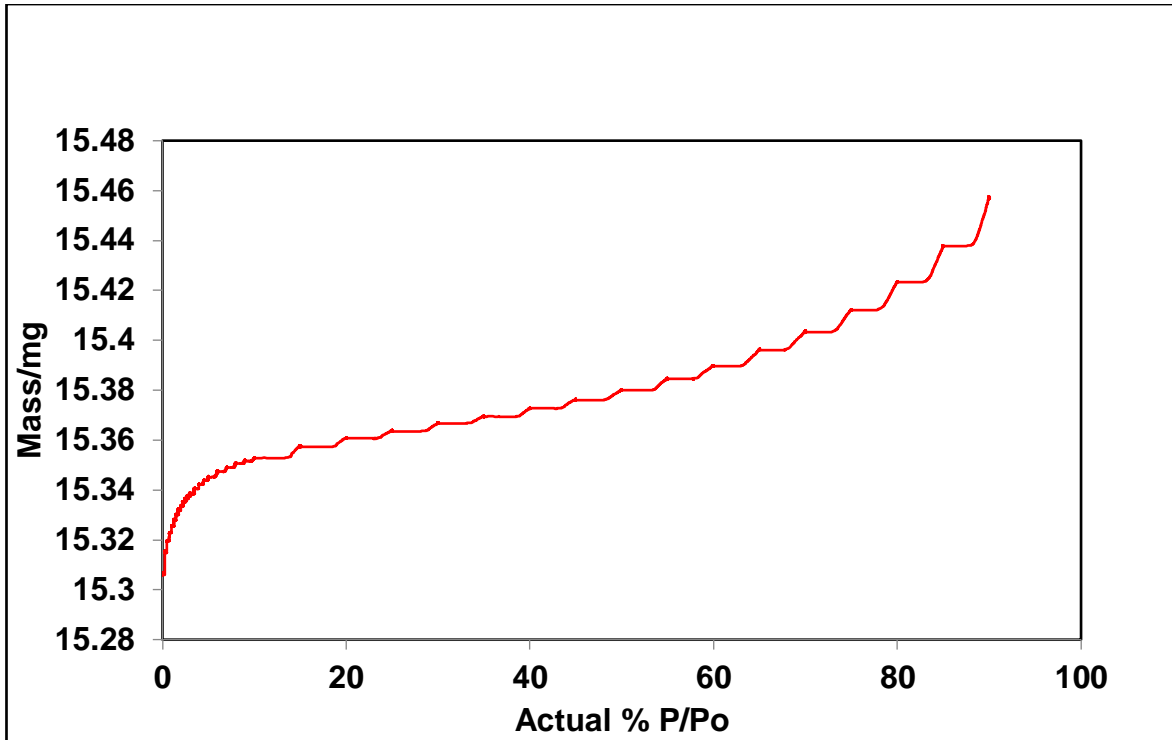
### Specific Surface Area with Brunauer-Emmett-Teller (BET)



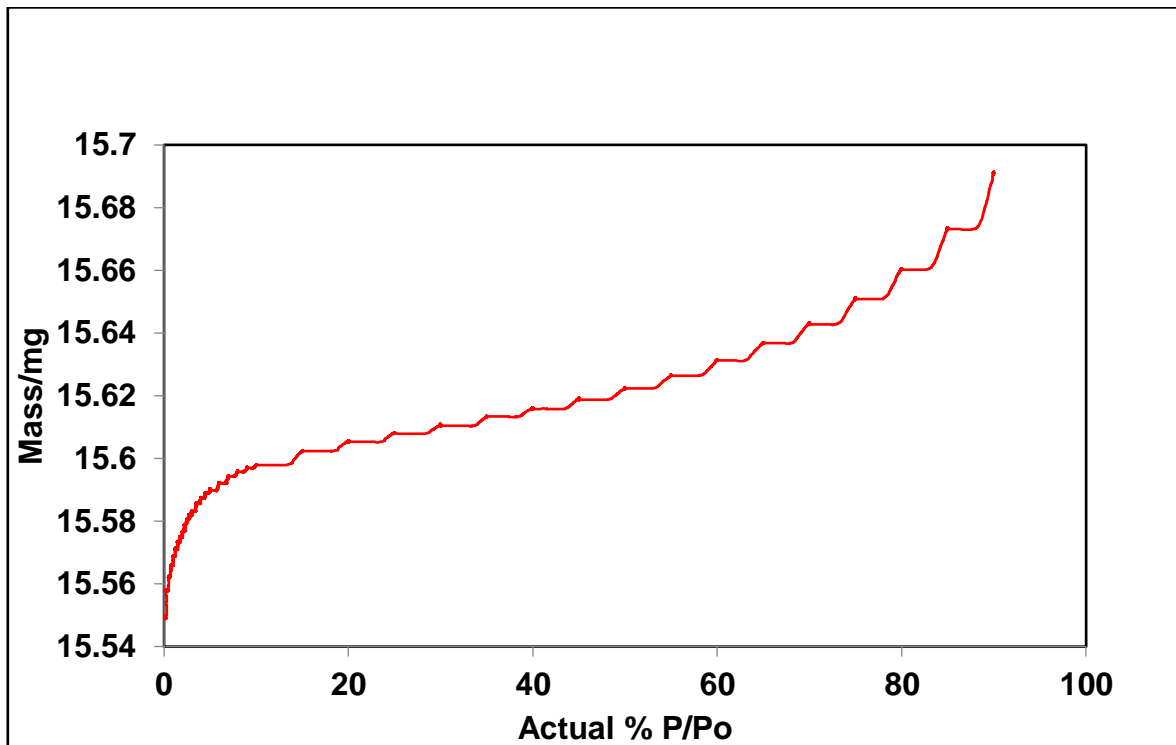
a)



b)



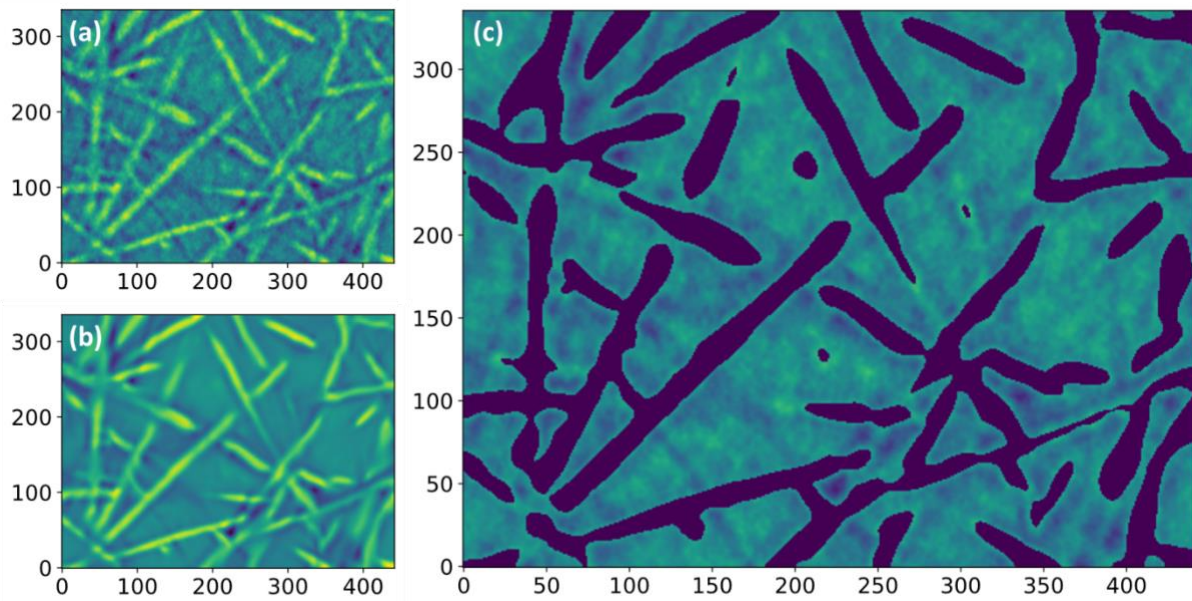
c)



d)

Figure S1 – Isotherms of a) pristine, b) sintered, and sintered/laser perforated sample with c) 1000um, and d) 2000um distance between holes

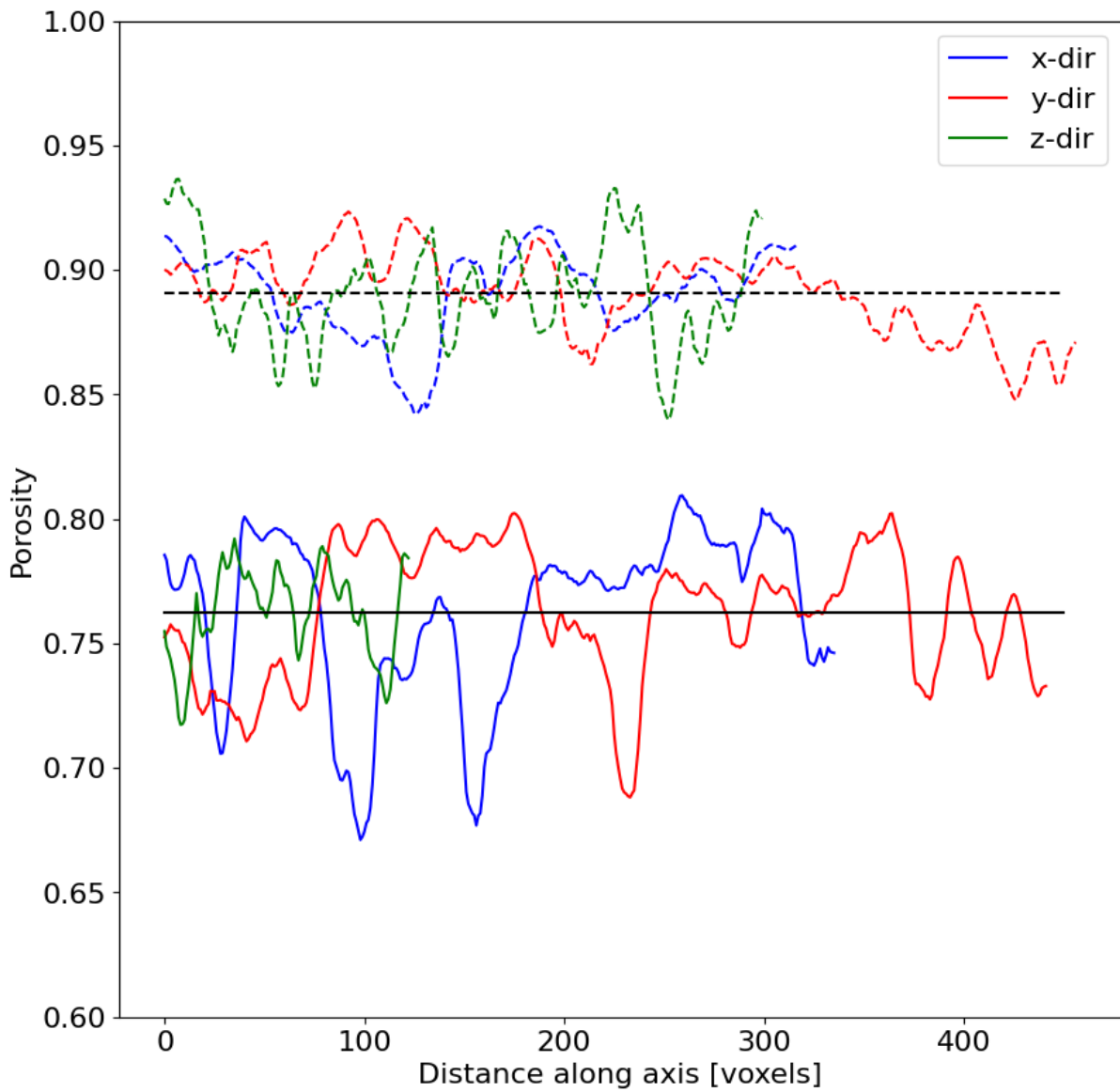
## Image Processing



*Figure S2 – Image of compressed sample after non-local means denoising*

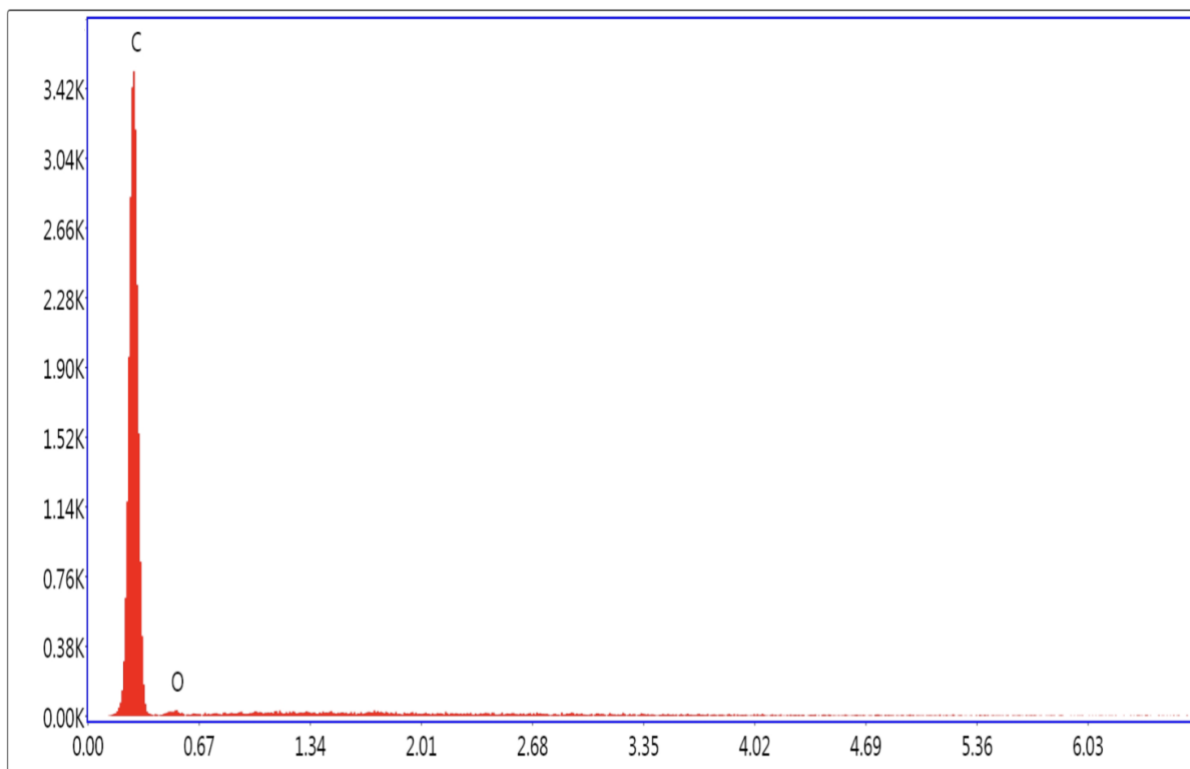
## Porosity Distribution

Figure S3 shows porosity profiles computed along each axis for both pristine and compressed electrospun fibrous samples. The values vary substantially due to the random nature of the samples. Perhaps the main observable trend here is that the porosity in the compressed sample varies more strongly, but in relative and absolute terms, than the uncompressed sample. This is somewhat counterintuitive since it might be expected that the compression would act to smooth out the heterogeneities.

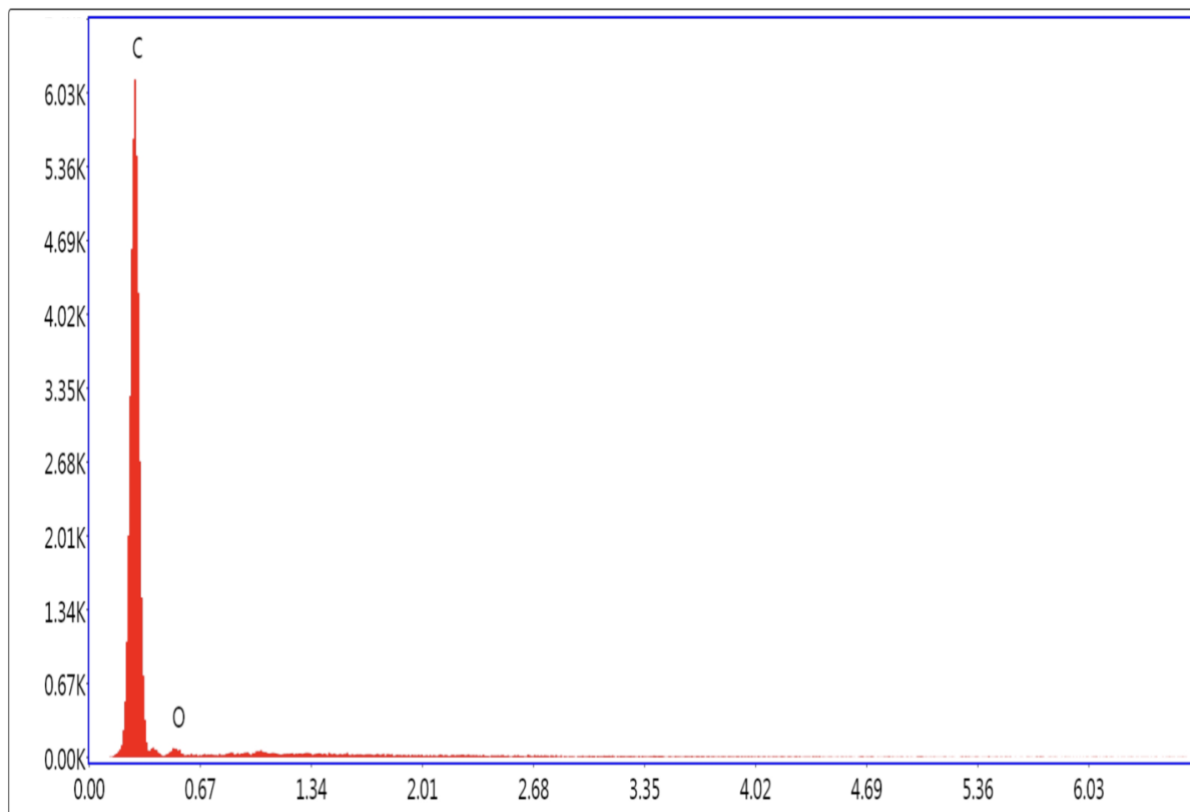


*Figure S3 - Porosity profiles for the uncompressed (top, dashed lines) and compressed (bottom, solid lines) samples. All three principal directions are shown.*

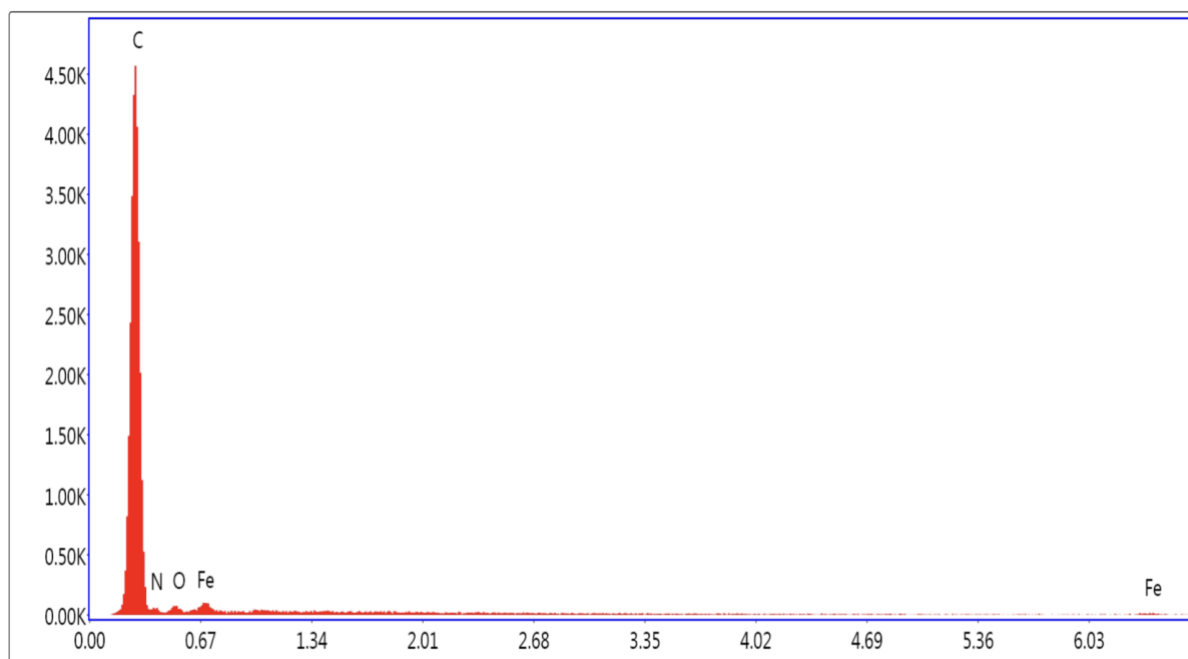
## Energy Dispersive X-Ray Spectroscopy



a)



b)



c)

**Figure S4 – Components in a) SGL25AA, b) pristine, and c) compressed electrospun sample in Chapter 5 obtained through energy dispersive x-ray spectroscopy**

**Table S1 – Component of fibrous electrode samples in chapter 5**

	SGL25AA		Pristine		Compressed			
	C	O	C	O	C	O	N	Fe
Weight %	98.76	1.24	96.97	3.03	86.55	2.48	8.21	2.76
Atomic %	99.07	0.93	97.71	2.29	90.12	7.33	1.94	0.62